Supplementary Information

Ionic Self-Assembled Monolayers Enable Neutral Interfaces and Synergistic Charge Extraction in High-Efficiency Perovskite Solar Cells

Supplementary Movie 1. MD trajectories of Me-4PACz in water for 2 ns

Supplementary Movie 2. MD trajectories of 2PACz-K in water for 2 ns

Supplementary Movie 3. MD trajectories of Me-4PACz in EtOH for 2 ns

Supplementary Movie 4. MD trajectories of Me-4PACz and 2PACz-K in EtOH for 2 ns

Supplementary Movie 5. AIMD trajectories of Me-4PACz at 5000 K for 125 fs

Supplementary Movie 6. AIMD trajectories of 2PACz-K at 5000 K for 125 fs

Supplementary Movie 7. IRC downhill trajectories of Me-4PACz under the electric field of -0.01 a.u.

Supplementary Movie 8. IRC downhill trajectories of 2PACz-K under the electric field of -0.01 a.u.

Supplementary Molecular Synthesis

General procedure of metal phosphonate salt preparation by acid-base neutralization reaction:

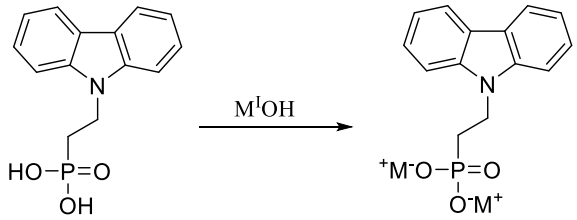

2PACz **2PACz-M**

Supplementary Scheme 1. The synthesis of 2PACz-M

Phosphonic acid (1 mmol) is dissolved in methanol (10 ml) and 2 mmol of the corresponding metal (I) hydroxide is added. The reaction mixture is stirred overnight at room temperature and the solvent is distilled off with a vacuum rotary evaporator. The resulting crystals were dissolved in methanol and precipitated in diethyl ether. The precipitate is filtered, washed with diethyl ether, and dried to obtain phosphonate salt in quantitative yield.

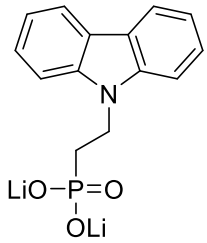

lithium (2-(9H-carbazol-9-yl)ethyl)phosphonate (**2PACz-Li**)

^{1}H NMR (400 MHz, MeOD) δ 8.04 (d, J = 7.7 Hz, 2H), 7.59 (d, J = 8.1 Hz, 2H), 7.41 (t, J = 7.7 Hz, 2H), 7.15 (t, J = 7.4 Hz, 2H), 4.6o (dt, J = 13.0, 3.9 Hz, 2H), 2.08 – 1.95 (m, 2H). ^{13}C NMR (101 MHz, MeOD) δ 141.35, 126.65, 124.19, 121.00, 119.77, 109.93, 38.61, 28.56, 27.31. $C_{14}H_{12}NLi_2O_3P$ [M^+] exact mass = 287.087, MS (ESI) = 287.66.

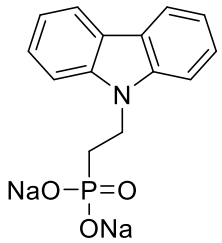

sodium (2-(9H-carbazol-9-yl)ethyl)phosphonate (**2PACz-Na**)

^{1}H NMR (400 MHz, MeOD) δ 8.01 (d, J = 7.7 Hz, 2H), 7.68 (d, J = 8.2 Hz, 2H), 7.39 (t, J = 7.7 Hz, 2H), 7.12 (t, J = 7.5 Hz, 2H), 4.63 (dt, J = 12.9, 3.9 Hz, 2H), 2.06 – 1.90 (m, 2H). ^{13}C NMR (101 MHz, MeOD) δ 141.52, 126.46, 124.07, 120.82, 119.46, 110.26, 40.73, 31.11, 29.87. $C_{14}H_{12}NNa_2O_3P$ [M^+] exact mass = 319.035, MS (ESI) = 319.72.

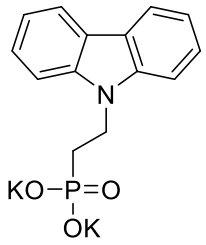

potassium (2-(9H-carbazol-9-yl)ethyl)phosphonate (**2PACz-K**)

^{1}H NMR (400 MHz, MeOD) δ 8.02 (d, J = 7.8 Hz, 2H), 7.67 (d, J = 8.2 Hz, 2H), 7.39 (t, J = 7.7 Hz, 2H), 7.12 (t, J = 7.5 Hz, 2H), 4.63 (dt, J = 13.0, 3.9 Hz, 2H), 2.04 – 1.91 (m, 2H). ^{13}C NMR (101 MHz, MeOD) δ 141.50, 126.48, 124.08, 120.85, 119.50, 110.22, 40.68, 31.08, 29.84. $C_{14}H_{12}NK_2O_3P$ [M^+] exact mass = 350.983, MS (ESI) = 351.62.

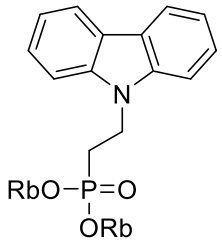

rubidium (2-(9H-carbazol-9-yl)ethyl)phosphonate (**2PACz-Rb**)

^{1}H NMR (400 MHz, MeOD) δ 7.99 (d, J = 7.8 Hz, 2H), 7.68 (d, J = 8.2 Hz, 2H), 7.36 (t, J = 7.7 Hz, 2H), 7.10 (t, J = 7.4 Hz, 2H), 4.61 (dt, J = 12.8, 3.9 Hz, 2H), 2.00 – 1.87 (m, 2H). ^{13}C NMR (101 MHz, MeOD) δ 141.55, 126.43, 124.04, 120.82, 119.43,

110.31, 40.97, 31.42, 30.20. $C_{14}H_{12}NO_3PRb_2$ [M^+] exact mass = 442.879, MS (ESI) = 443.16.

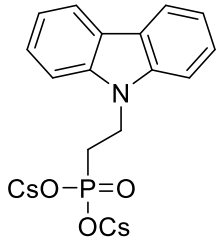

cesium (2-(9H-carbazol-9-yl)ethyl)phosphonate (**2PACz-Cs**)

^{1}H NMR (400 MHz, MeOD) δ 7.99 (d, J = 7.8 Hz, 2H), 7.68 (d, J = 8.2 Hz, 2H), 7.41 – 7.32 (m, 2H), 7.10 (t, J = 7.4 Hz, 2H), 4.61 (dt, J = 12.8, 3.9 Hz, 2H), 1.99 – 1.86 (m, 2H). ^{13}C NMR (101 MHz, MeOD) δ 141.55, 126.45, 124.03, 120.83, 119.44, 110.33, 40.99, 31.58, 30.36. $C_{14}H_{12}NO_3PCs_2$ [M^+] exact mass = 538.866, MS (ESI) = 539.66.

Supplementary Figure

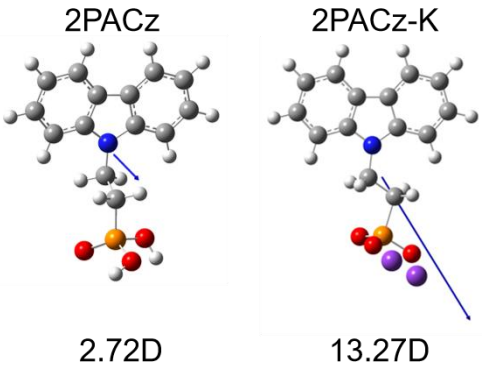

Supplementary Figure 1. Optimized geometry and dipole moment of 2PACz and 2PACz-K. The dipole moment points from negative to positive charge.

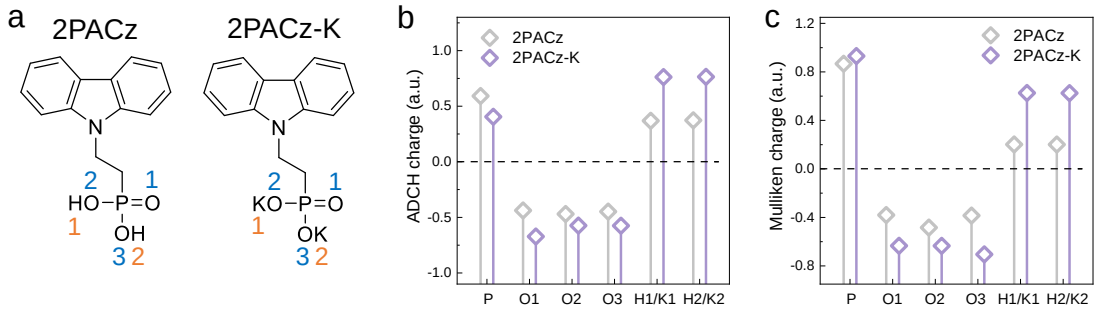

Supplementary Figure 2. Atomic charge analyses of 2PACz and 2PACz-K. (a) Chemical structures and atom numbers. (b) Atomic dipole corrected Hirshfeld (ADCH) atomic charge[1]. (c) Mulliken charge.
Notes: Compared with 2PACz, the O atoms in 2PACz-K are more negatively charged. The K atoms in 2PACz-K are more positively charged than the H atoms in 2PACz.

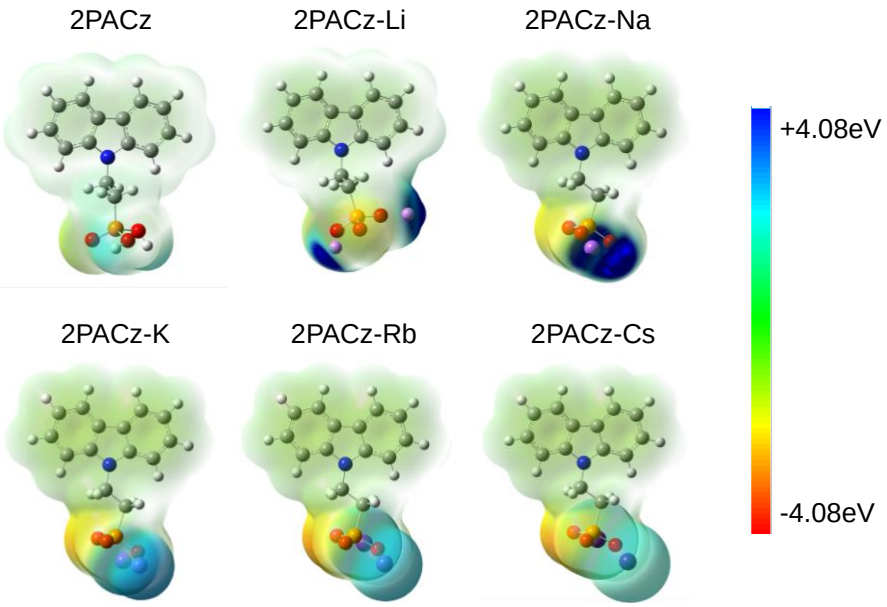

Supplementary Figure 3. Distribution of electrostatic potential (ESP) of 2PACz, 2PACz-Li, 2PACz-Na, 2PACz-K, 2PACz-Rb and 2PACz-Cs.

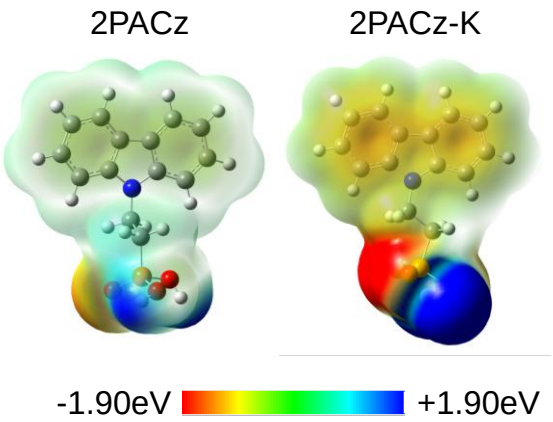

Supplementary Figure 4. Distribution of ESP of 2PACz and 2PACz-K. Narrower ESP display range is used for easy comparison.

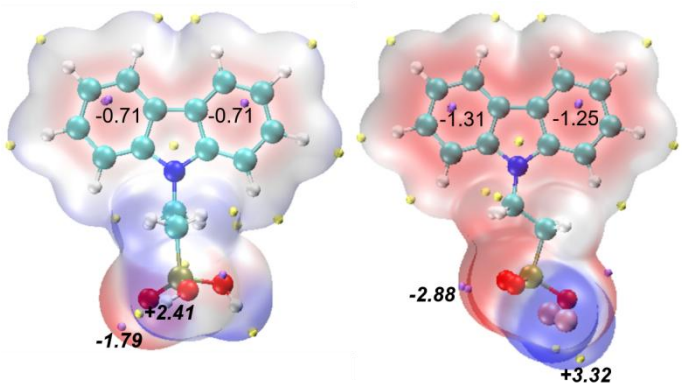

Supplementary Figure 5. Distribution of ESP of 2PACz and 2PACz-K over vdW surface (0.001 a.u. isosurface). Purple and yellow spheres correspond to surface minima and maxima, respectively. ESP values of some surface extreme points are manually labeled in eV, and the bold texts in italics correspond to global surface extreme values.

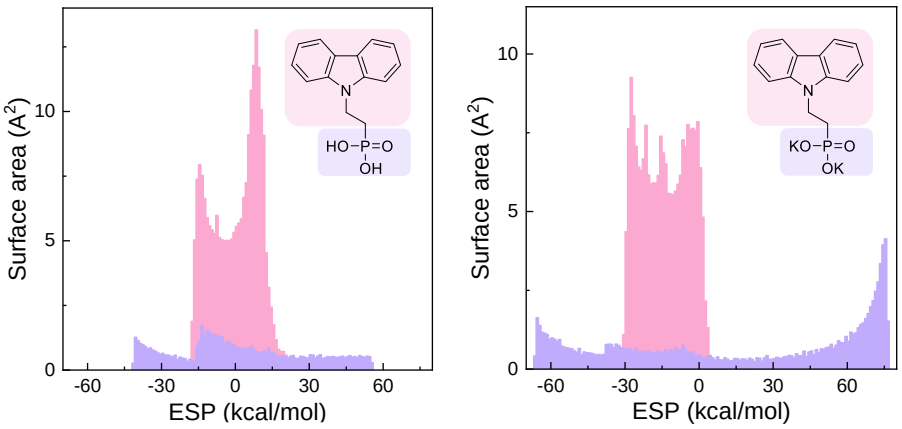

Supplementary Figure 6. Quantitative analyses of electrostatic potential area distribution as histogram of 2PACz and 2PACz-K[2,3]. Pink and purple colors highlight different fragments.

Notes: For 2PACz, the molecular polarity index (MPI) is 0.37 eV (8.54 kcal/mol), with nonpolar surface area (|ESP| ≤ 10 kcal/mol) of 139.86 Angstrom^2 (62.30%) and polar surface area (|ESP| > 10 kcal/mol) of 84.62 Angstrom^2 (37.70%). For 2PACz-K, the MPI is 1.09 eV (25.15 kcal/mol), with nonpolar surface area of 95.55 Angstrom^2 (29.02%) and polar surface area of 233.71 Angstrom^2 (70.98%). Therefore, 2PACz-K exhibits more polar surface area.

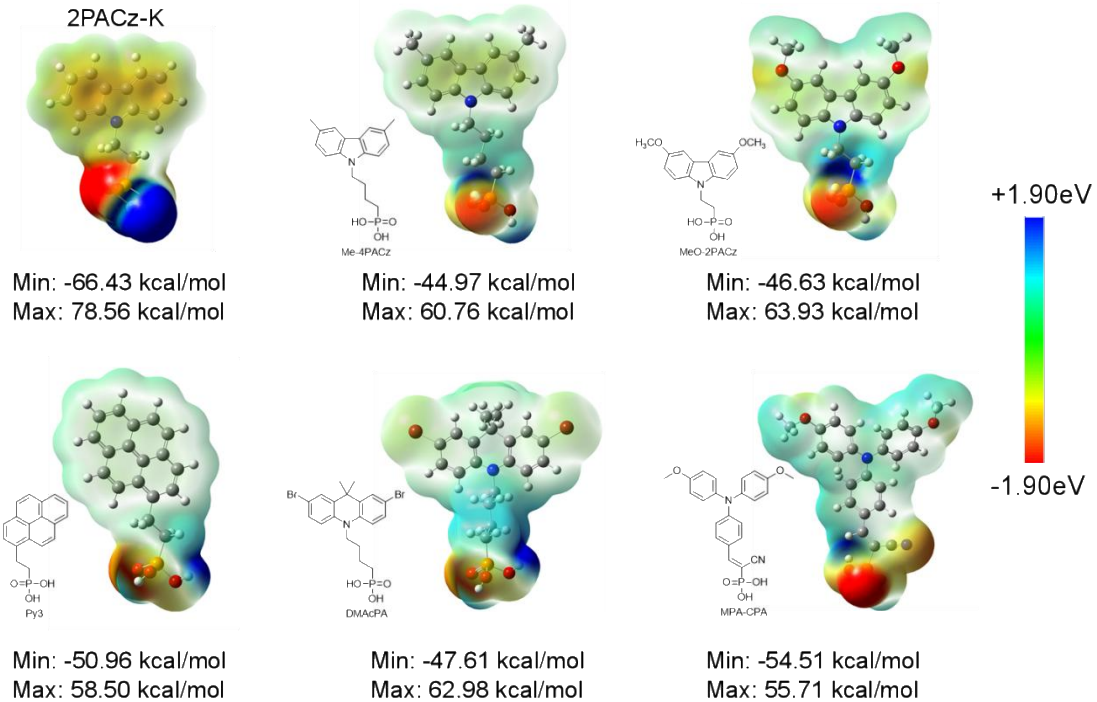

Supplementary Figure 7. Chemical structures and ESP distributions of 2PACz-K, Me-4PACz, MeO-2PACz, Py3, DMAcPA and MPA-CPA over vdW surface[4]. 1 eV = 23.06 kcal/mol.

Notes: Compared with other SAMs, 2PACz-K exhibits obvious charge separation due to bigger difference between surface minima and maxima.

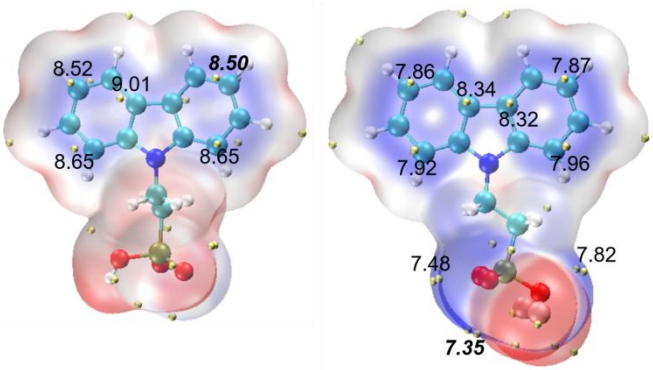

Supplementary Figure 8. Average local ionization energy (ALIE) maps on vdW surface of 2PACz and 2PACz-K. Yellow spheres correspond to surface ALIE minima. ALIE minima are manually labeled in eV.

Notes: ALIE is a real space function reflecting electron ionization energy in a local region. The regions with lower ALIE indicate the electrons are bound weaker with higher reactivity.

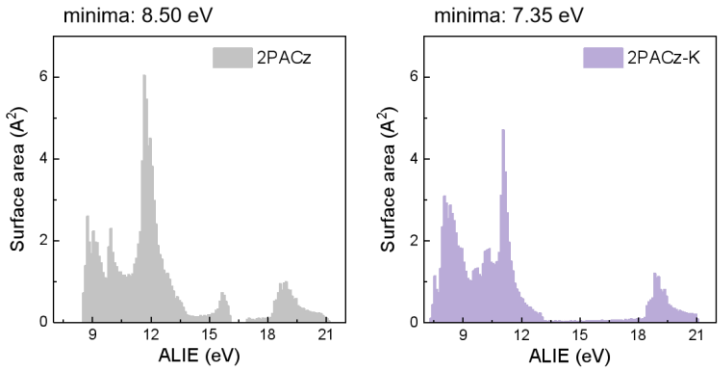

Supplementary Figure 9. Quantitative analyses of ALIE distribution as histogram for 2PACz and 2PACz-K.

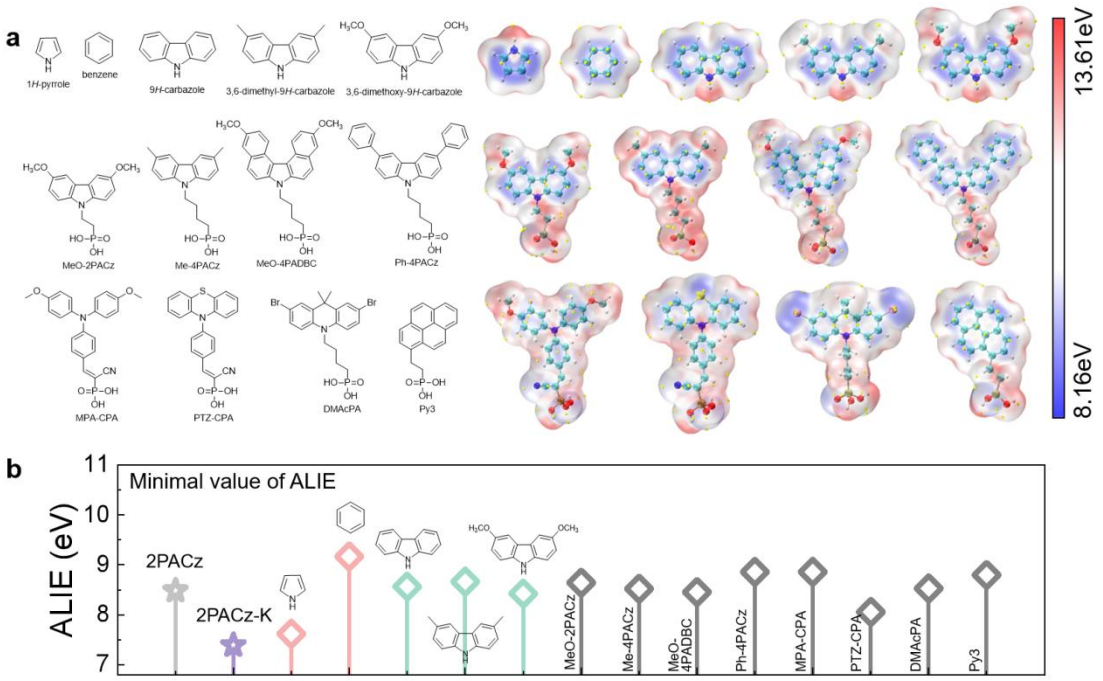

Supplementary Figure 10. (a) Chemical structure and ALIE maps of 2PACz, 2PACz-K, some aromatic fragments and SAMs[4]. Yellow spheres correspond to surface ALIE minima. (b) Comparison of ALIE minima.

Notes: The ALIE distribution on vdW surface and ALIE minima of some other molecules containing π-electrons are given above. 2PACz-K shows the lowest ALIE minimum among these aromatic fragments and SAMs, resulting from its delocalized π-electrons with high reactivity.

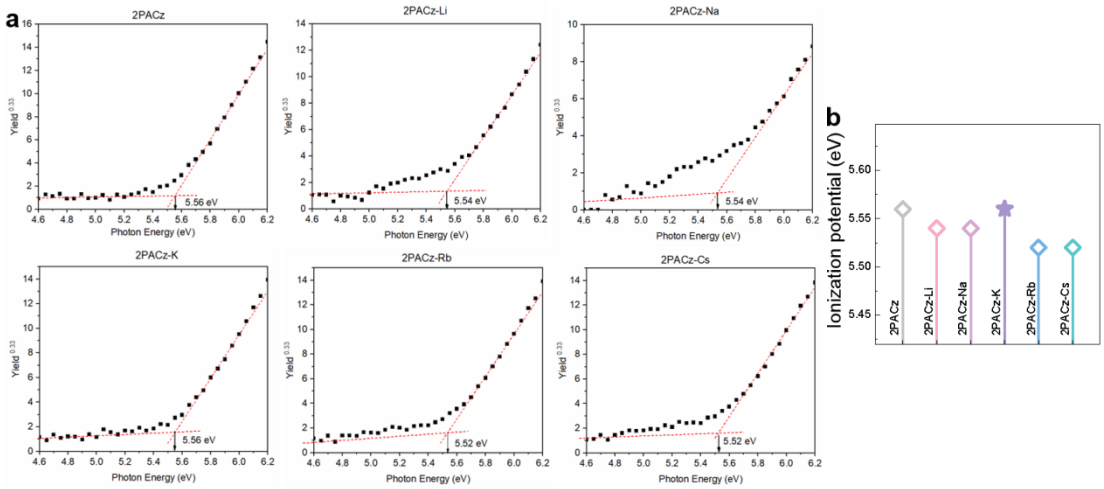

Supplementary Figure 11. Ionization potential (IP) measured by photoelectron spectroscopy in air (PESA). (a) The spectra. (b) IP values. The SAM solutions (EtOH) were spin-coated onto an ITO glass. A diffraction grating monochromator with a deuterium lamp was used for the experiment. The power of the falling light was ~5×10^{-8} W. A negative voltage (-100 V) was connected to the test sample. The electron photoemission current was measured with an Flat-plate open counter.

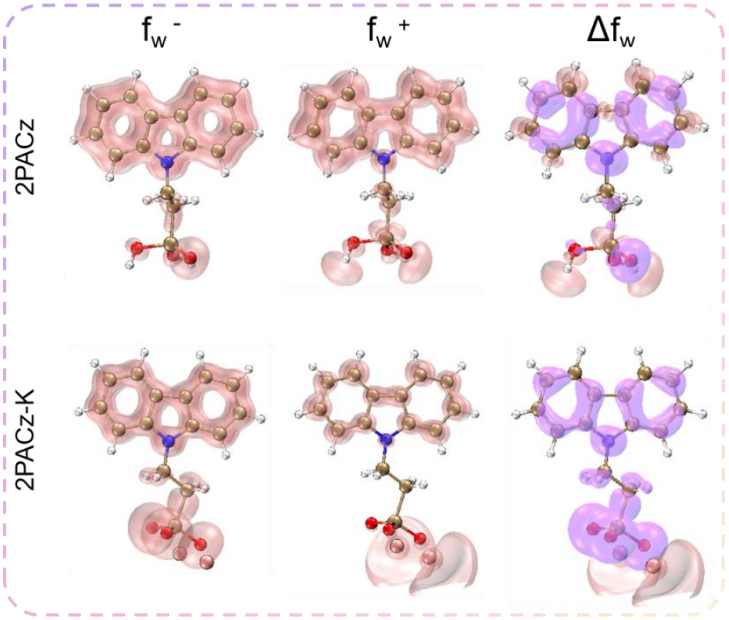

Supplementary Figure 12. Local reactivity analyses of 2PACz and 2PACz-K. Isosurface maps of orbital-weighted Fukui function (f_w^- and f_w^+) and orbital-weighted dual descriptor (Δf_w) with isovalue = ±0.0005. For orbital-weighted dual descriptor, pink/purple (positive/negative values) represent nucleophilic/electrophilic attack susceptibility.

Notes: The Fukui function is one of the most important local reactivity index in Conceptual Density Functional Theory (CDFT). High values of f_w^+ or f_w^- indicate the active sites to receive or donate electrons respectively, which indicates high electrophilicity or nucleophilicity[5]. Compared to 2PACz, 2PACz-K exhibits more widely distributed f_w^-, suggesting the ability to donate electrons (i.e., receive holes).

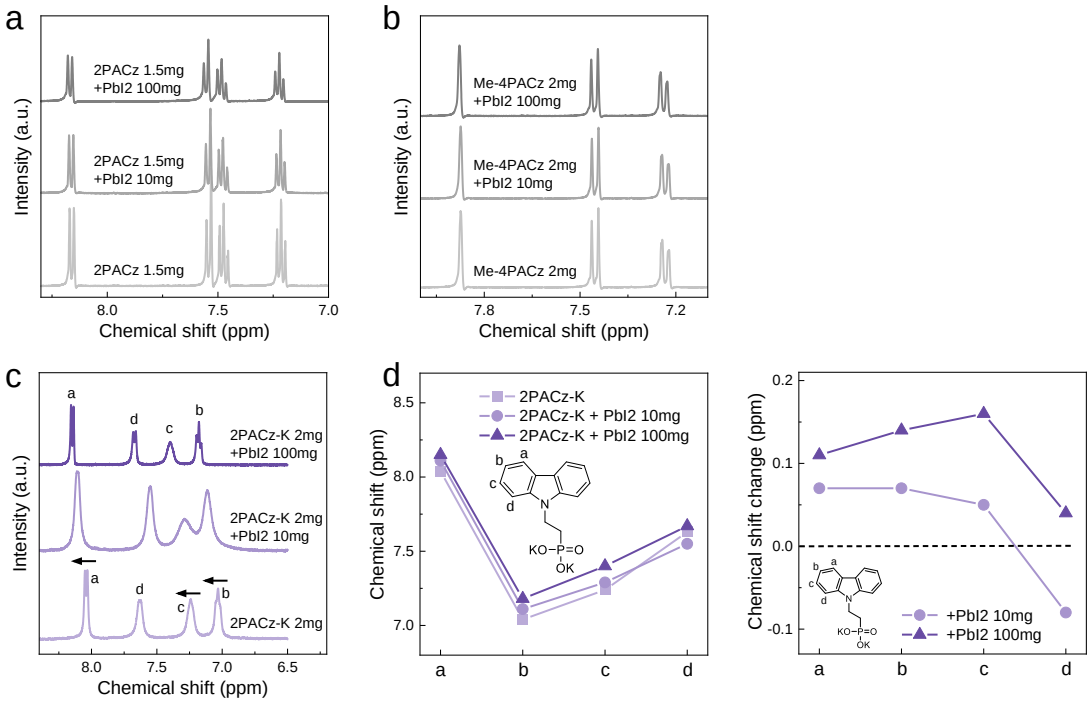

Supplementary Figure 13. (a-c) Enlarged ^{1}H-NMR liquid-state spectra in d_6-DMSO for PbI_2 and SAMs (including 2PACz, Me-4PACz and 2PACz-K, respectively). (d) Chemical shift change ($\Delta\delta$) between 2PACz-K and PbI_2.

Notes: When mixed with different amount of PbI_2, 2PACz and Me-4PACz show no obvious peak shift in the NMR spectra, indicating their limited electron donating ability. While the NMR spectra of 2PACz-K show obvious downfield shifts after mixing with PbI_2, manifesting the reduction of electron cloud densities around protons in carbazole ring of 2PACz-K due to the Lewis acid-base interactions.

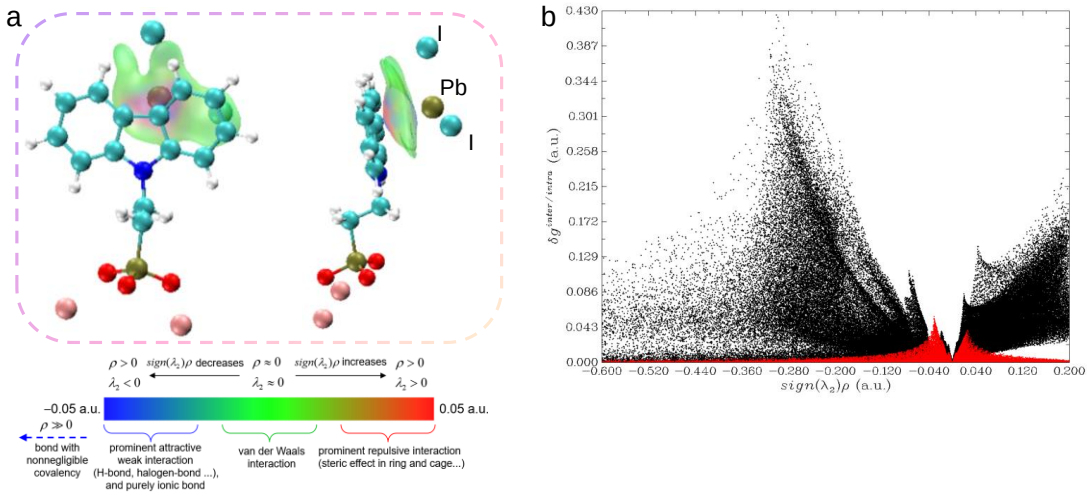

Supplementary Figure 14. The independent gradient model (IGM) analyses of 2PACz-K and PbI_2. (a) Front and side view of IGM maps of δg^{inter} with isosurface of 0.005 a.u. (b) Scatter plot of δg^{inter} (red area) and δg^{intra} (black area).

Notes: δg^{inter} and δg^{intra} reveal interfragment interactions and intrafragment interactions, respectively. $Sign(\lambda_2)\rho$ denotes product of electron density (ρ), and sign of the second largest eigenvalue of Hessian matrix of ρ, $sign(\lambda_2)$.

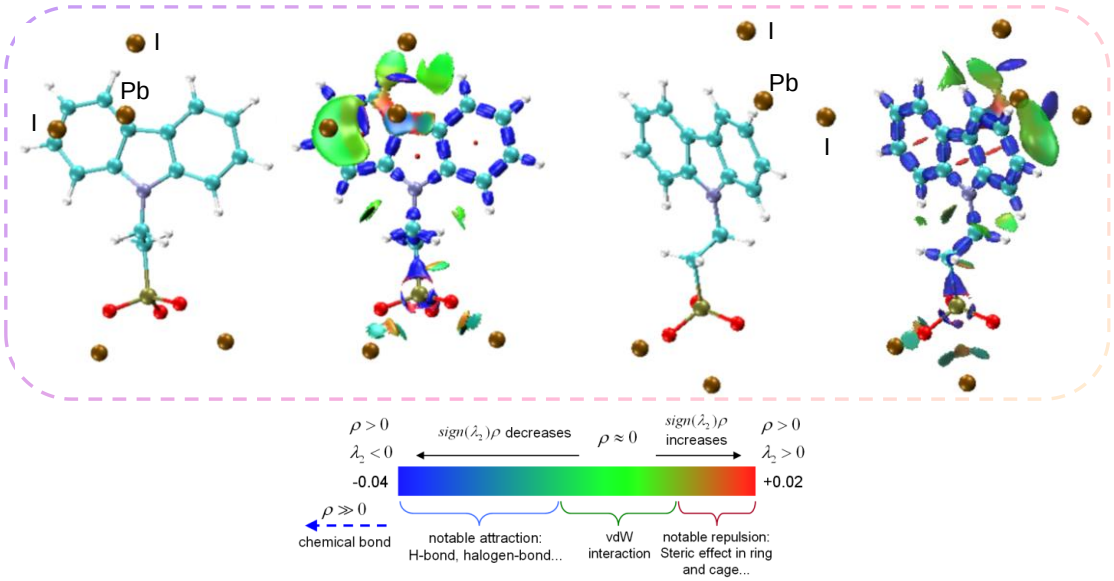

Supplementary Figure 15. Front and side view of chemical structure skeleton and

interaction region indicator (IRI) maps of 2PACz-K and PbI_2. The isosurface is 1.0 a.u.

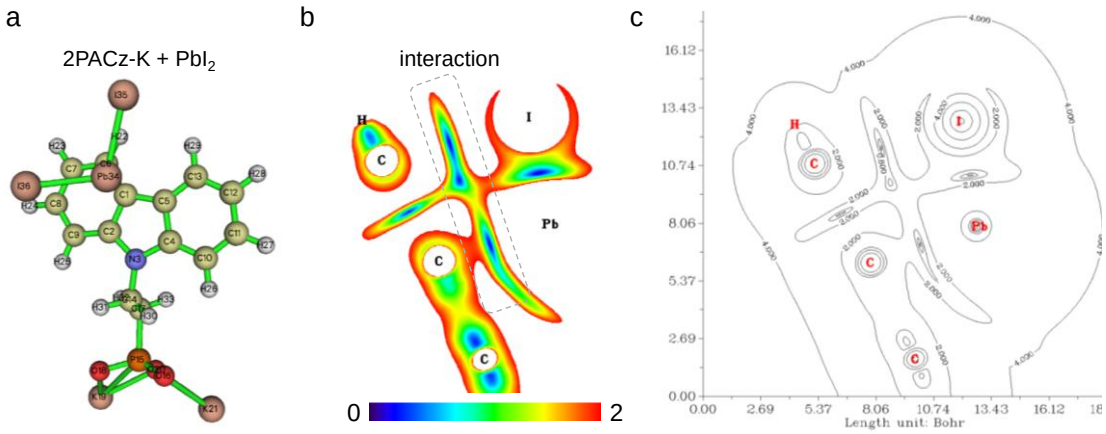

Supplementary Figure 16. IRI analyses of 2PACz-K and PbI_2. (a) Chemical structure skeleton and atom numbers. (b) Color-filled map of the plane of C1, C8, Pb34 and I36[6]. The interaction area of carbazole and PbI_2 is marked by gray dashed rectangle. (c) Contour line map of the plane of C1, C8, Pb34 and I36.

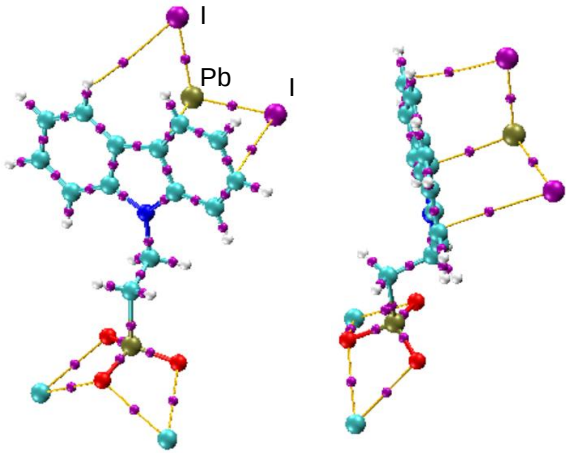

Supplementary Figure 17. Front and side view of topology analyses on electron density of 2PACz-K and PbI_2 based on Atoms in Molecules (AIM) theory[7]. Yellow lines are bond paths, and purple spheres correspond to the (3,-1) critical points (i.e., bond critical point, BCP). The BCPs and bond paths between 2PACz-K and PbI_2 indicate their interaction.

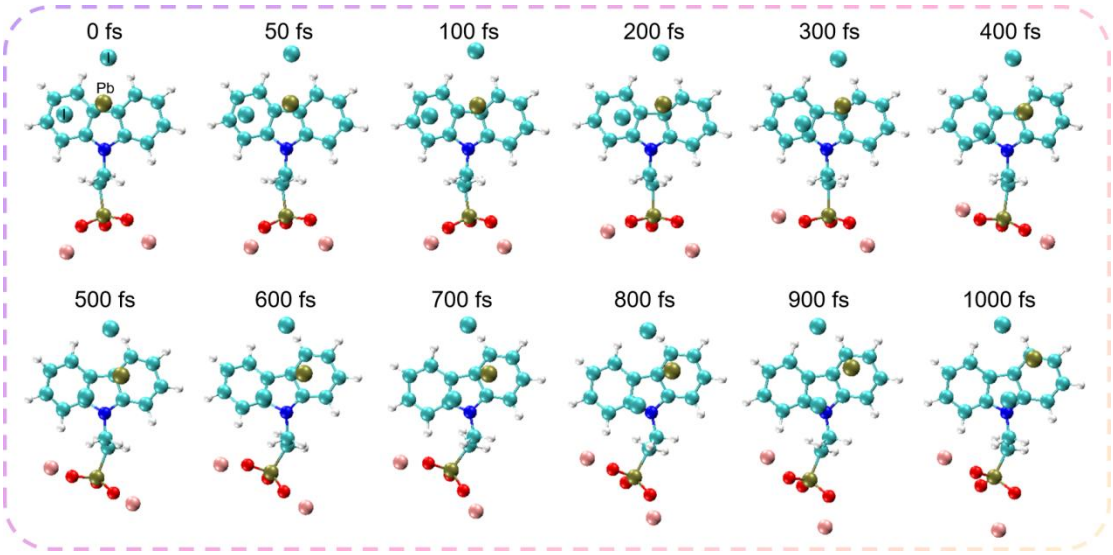

Supplementary Figure 18. The *ab-initio* molecular dynamics (AIMD) trajectories simulated at 300 K for 2PACz-K and PbI_2. The DFT optimized structure corresponds to the first frame. The full trajectory is attached in Supplementary Movie 1.
Notes: During the 1000 fs simulation, 2PACz-K and PbI_2 maintain close, and their dissociation is not observed, confirming the strong interaction between 2PACz-K and PbI_2.

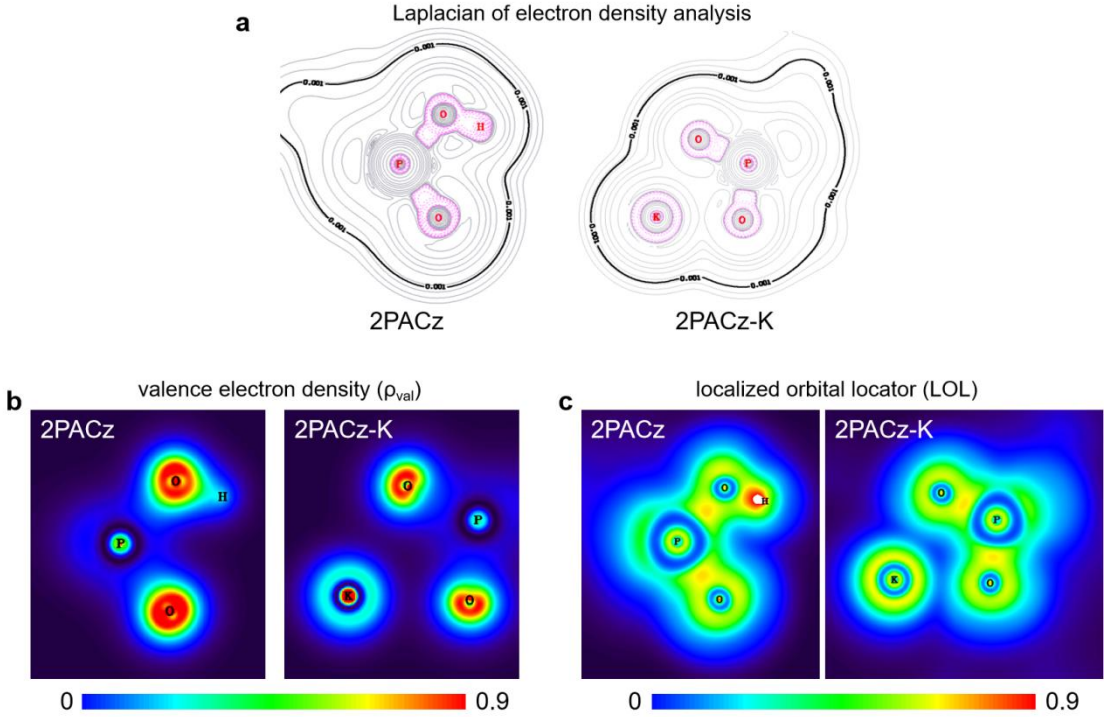

Supplementary Figure 19. Three-dimension real space function analyses of phosphonate groups in 2PACz and 2PACz-K[8]. (a) Contour line maps for Laplacian of electron density[9]. Gray solid lines and pink dash lines represent positive and negative regions, respectively. Color-filled maps of (b) valence electron density (ρ_{val}) and (c)

localized orbital locator (LOL).

Notes: (i) Laplacian of electron density is a three-dimension real space function, one of the key ingredients of the famous atoms in molecules (AIM) theory[7]. Covalent bonds form between O and H atoms in 2PACz due to valence bonding charge concentration, while ionic bonds exist between O and K atoms in 2PACz-K without charge concentration. (ii) The valence electron density is defined as the electron density with removal of contribution of inner core electrons, which is useful in characterizing chemical bonds. (iii) Localized orbital locator (LOL) is a dimensionless function with a range of [0,1] based on localized molecular orbitals (LMOs)[8].

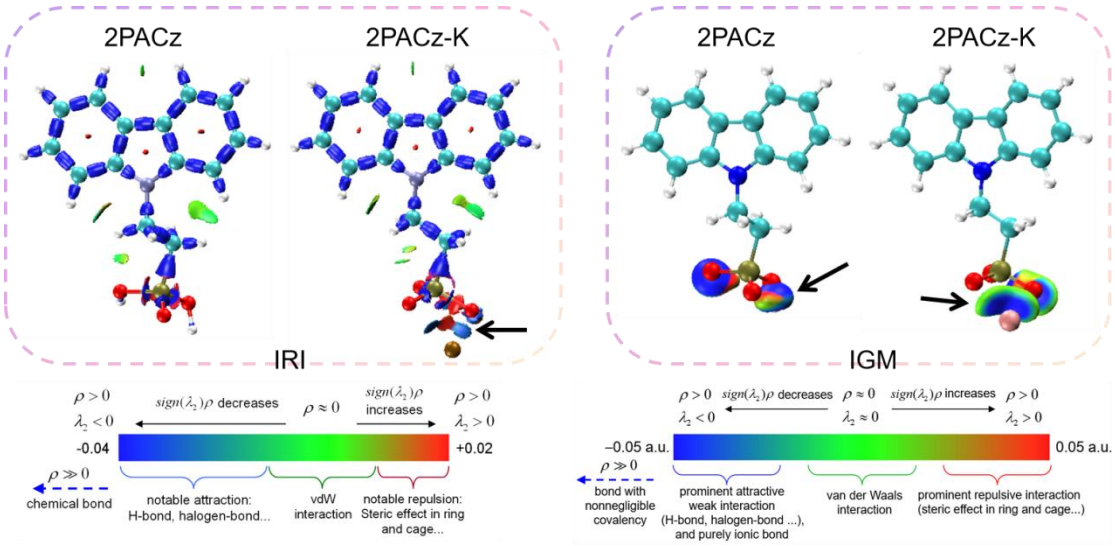

Supplementary Figure 20. Interaction region indicator (IRI) and the independent gradient model (IGM) maps with isosurface of 1.0 a.u. and 0.01 a.u. respectively. The black arrows point out the O-H or O-K bonds in phosphonate groups.

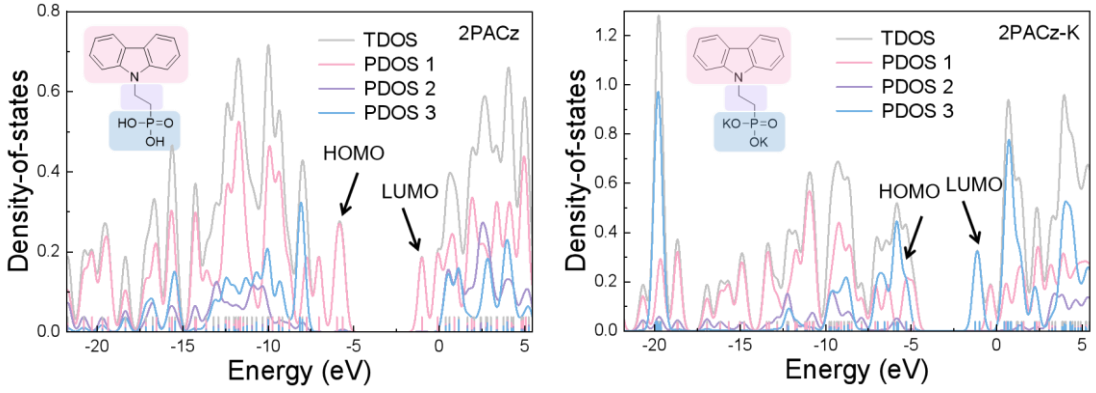

Supplementary Figure 21. Density-of-states (DOS) maps of 2PACz and 2PACz-K, including total DOS (TDOS) and partial DOS (PDOS). The three fragments of PDOS are colored by pink, purple and blue for carbazole, alkyl and phosphonate groups.

Notes: For 2PACz, HOMO and LUMO are mainly contributed by the carbazole ring (see the black arrows and pink lines). While for 2PACz-K, the phosphonate group and carbazole ring jointly dominate HOMO and LUMO (see the black arrows and pink

and blue lines).

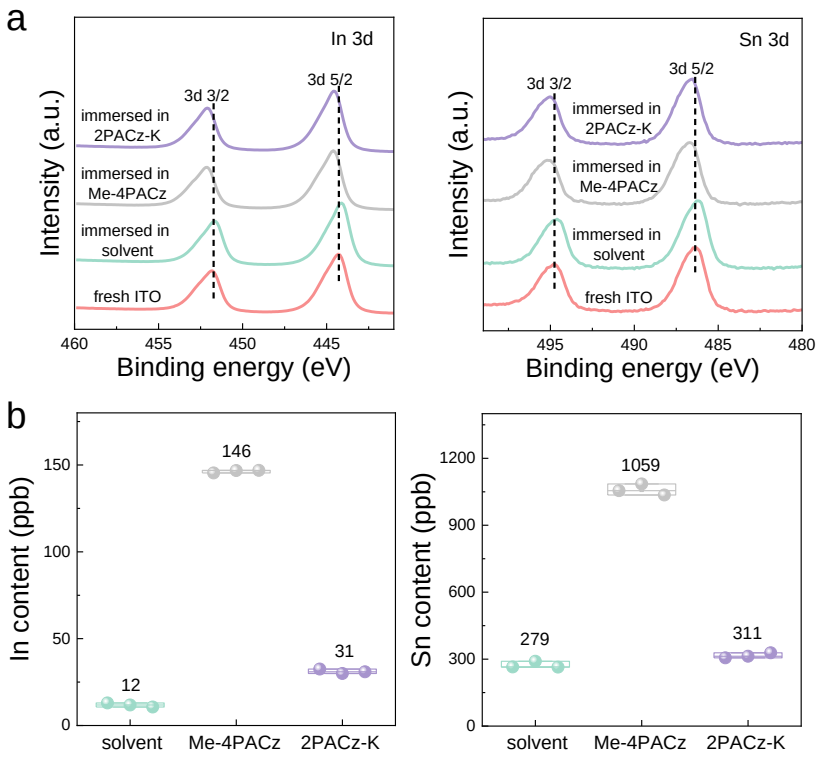

Supplementary Figure 22. The corrosion effect of SAMs on ITO. (a) High-resolution XPS spectra of In 3d and Sn 3d core level of fresh ITO and immersed ITO. Specifically, 2 pieces of ITO films (1.5 cm × 1.5 cm) were immersed in the solvent (DMF+EtOH, 1:10 in volume), Me-4PACz (5 mg/ml in DMF+EtOH) and 2PACz-K solution (5 mg/ml in DMF+EtOH) for 24 h at 60 °C, respectively. (b) In and Sn content of ITO films immersed in the solvent, Me-4PACz and 2PACz-K solution detected by inductively coupled plasma mass spectrometry (ICP-MS).

Notes:

Compared with fresh ITO, the In 3d and Sn 3d peaks of ITO immersed in SAM solution exhibit significantly shift toward higher binding energies, demonstrating the strong chemical interactions between SAMs and ITO, due to decreased electron density around In_2O_3/SnO_2 caused by adsorption of phosphonate group. Besides, the concentration of Sn and In in 2PACz-K solution is much lower than that in Me-4PACz solution, confirming the suppressed corrosion of ITO, resulting from non-acidic 2PACz-K without ionizable hydrogen.

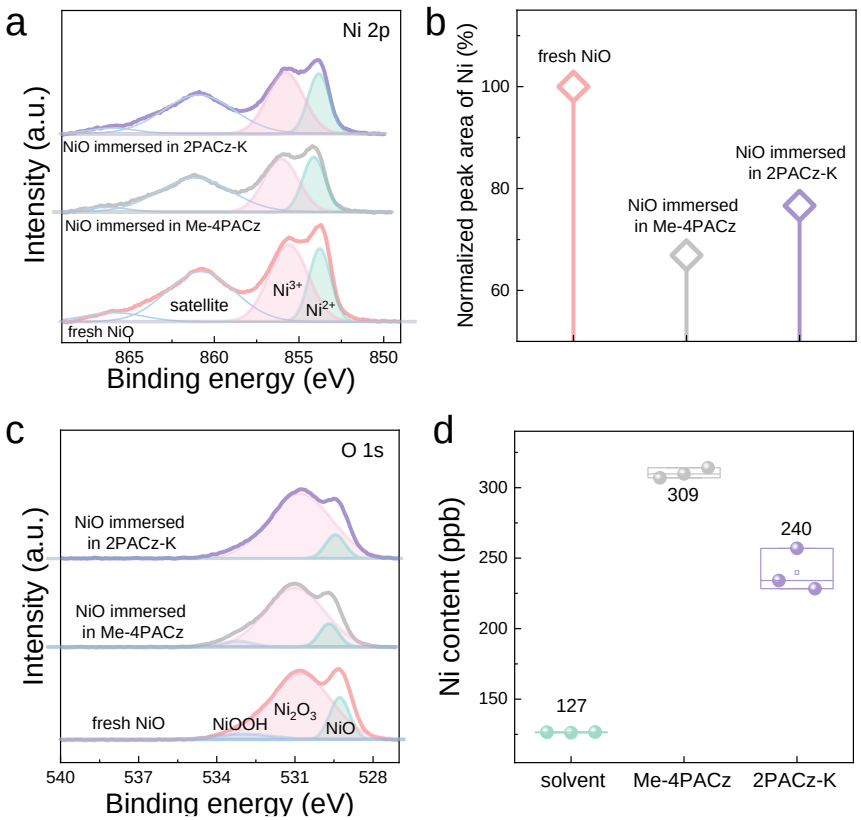

Supplementary Figure 23. The corrosion effect of SAMs on NiO_x. (a) High-resolution XPS spectra of Ni 2p core level of fresh NiO_x and immersed NiO_x films. (b) Normalized peak area of Ni (including Ni^{3+} and Ni^{2+} peak) of fresh NiO_x and immersed NiO_x. Specifically, 2 pieces of ITO/NiO_x films (1.5 cm × 1.5 cm) were immersed in Me-4PACz (5 mg/ml in DMF+EtOH) and 2PACz-K solution (5 mg/ml in DMF+EtOH) for 24 h at 60 °C, respectively. (c) High-resolution XPS spectra of O 1s core level of fresh NiO_x and immersed NiO_x. (d) Ni content of NiO_x films immersed in the solvent (DMF+EtOH, 1:10 in volume), Me-4PACz and 2PACz-K solution detected by ICP-MS.

Notes:

According to literature[10], when NiO_x film is exposed to an acidic environment, there is a corrosive reaction of $NiO + 2H^+ \rightarrow nNi^{2+} + (1\text{-}n)Ni^{3+} + H_2O$.

(i) Compared with fresh NiO_x, the Ni 2p peak area (Ni^{3+} and Ni^{2+}) of NiO_x immersed in Me-4PACz or 2PACz-K significantly reduces to 67% or 77% respectively, demonstrating the corrosion of NiO_x films. (ii) According to the integral area of peaks in the O 1s spectra, the Ni^{3+}/Ni^{2+} ratios increase after immersing in SAM solution, indicating the interaction between NiO_x and SAMs (which will be discussed in details in the next part). (iii) The concentration of Ni in 2PACz-K solution is much lower than that in Me-4PACz, confirming the suppressed corrosion of NiO_x, resulting from non-acidic 2PACz-K without ionizable hydrogen.

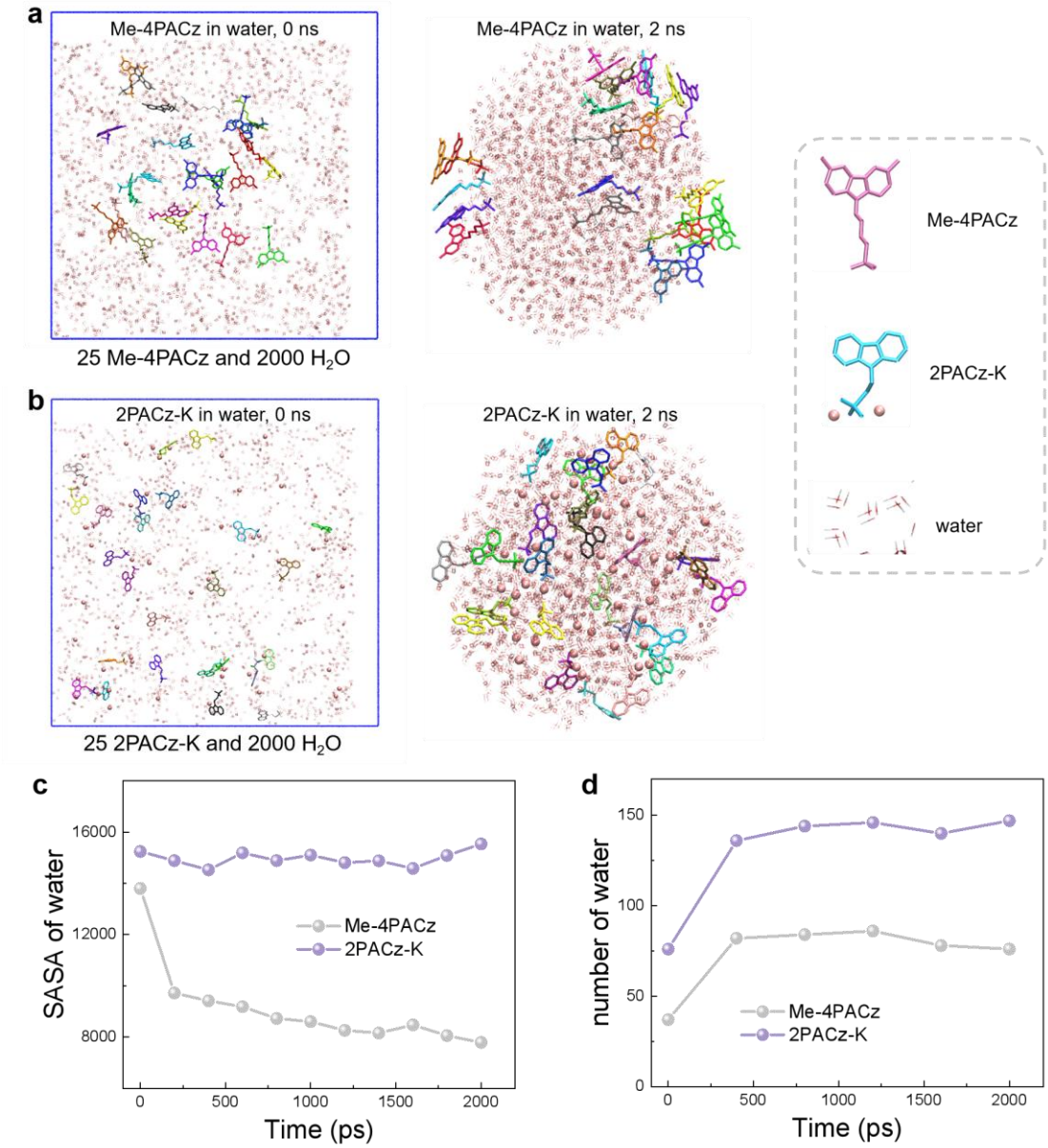

Supplementary Figure 24. The molecular arrangement patterns of (a) Me-4PACz and (b) 2PACz-K in water at 0 ns and 2 ns (i.e., 2000 ps) simulated by molecular dynamics (MD). The full trajectories are attached in Supplementary Movies 1-2. Hydrogen atoms of Me-4PACz and 2PACz-K are hided for easy observation. The blue square refers to the initial box of the system. (c) Solvent accessible surface area (SASA) of water and (d) number of water molecules within 2.5 Angstrom for Me-4PACz and 2PACz-K.

Notes:

We calculated the SASA of water with the probe radius of 1.4 Angstrom for Me-4PACz and 2PACz-K. 2PACz-K shows larger SASA than Me-4PACz. Besides, there are more water molecules around 2PACz-K than Me-4PACz.

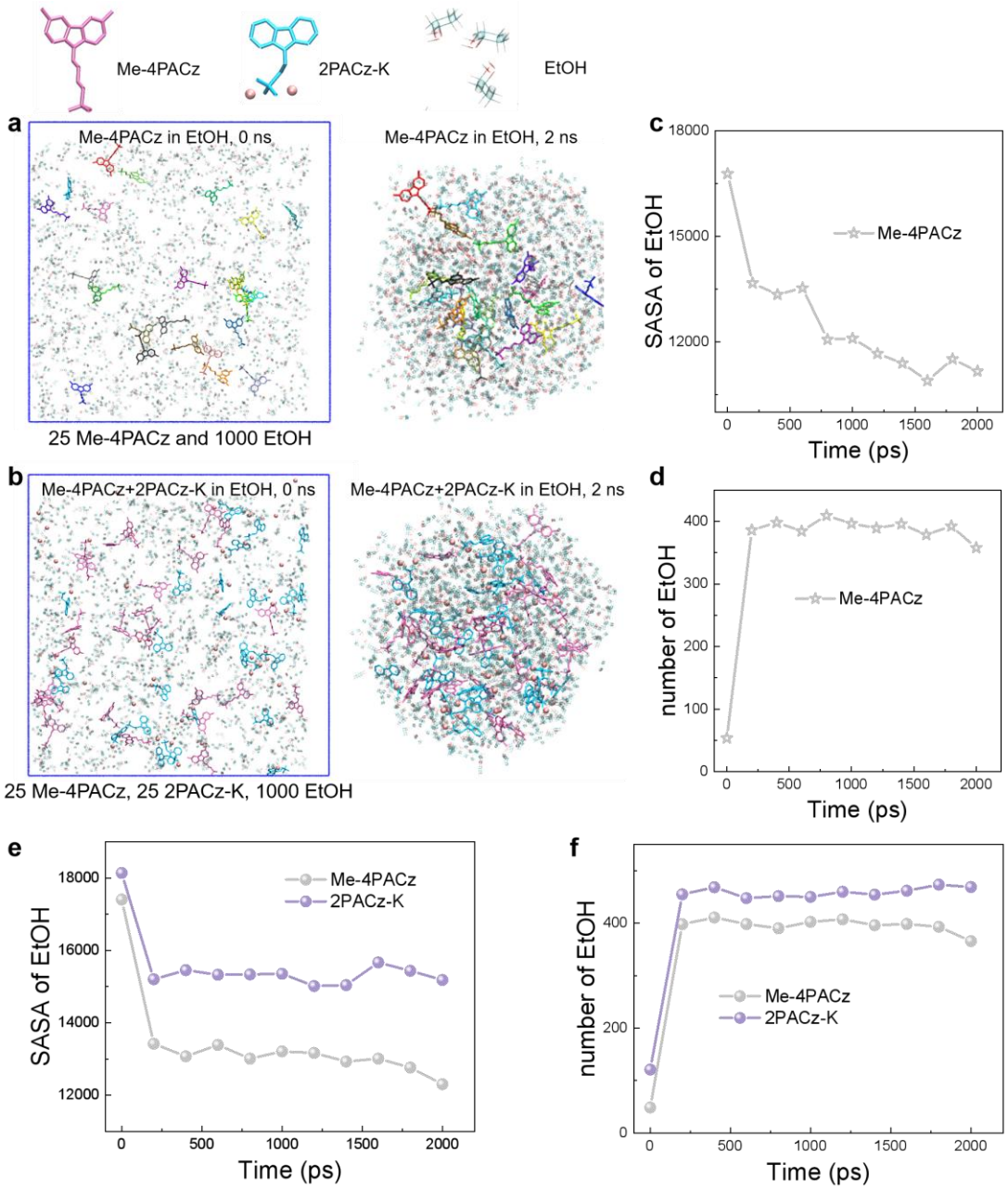

Supplementary Figure 25. The molecular arrangement patterns of (a) Me-4PACz and (b) mix SAMs in EtOH at 0 ns and 2 ns simulated by molecular dynamics. The full trajectories are attached in Supplementary Movies 3-4. (c) SASA of EtOH and (d) number of EtOH molecules within 5 Angstrom for Me-4PACz, corresponding to the system of 25 Me-4PACz and 1000 EtOH. The probe radius of EtOH is 2.0 Angstrom. (e) SASA of EtOH and (f) number of EtOH molecules for Me-4PACz and 2PACz-K, corresponding to the system of 25 Me-4PACz, 25 2PACz-K and 1000 EtOH.

Notes:

During the MD simulations of Me-4PACz EtOH solution, Me-4PACz molecules tend to aggregate and exhibit decreased SASA. While in the system of mixed SAMs, Me-4PACz and 2PACz-K disperse well in EtOH. The SASA of EtOH and number of EtOH molecules for Me-4PACz and 2PACz-K keep relatively constant from 200 to 2000 ps, indicating 2PACz-K avoids the aggregation of Me-4PACz.

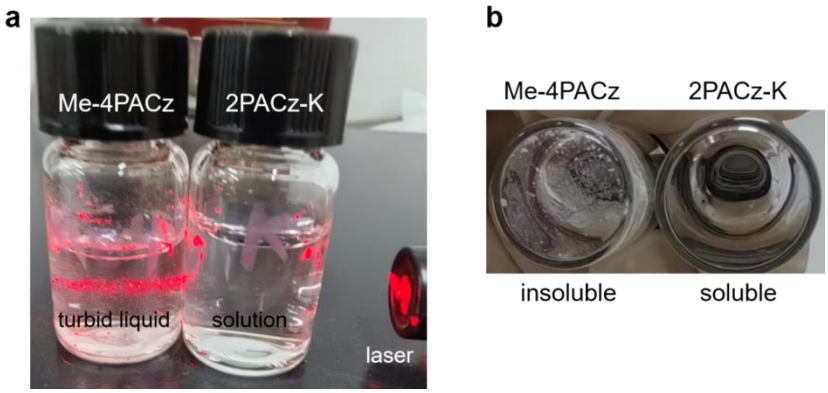

Supplementary Figure 26. The photos of Me-4PACz and 2PACz-K aqueous solution of 1 mg/ml. (a) side view illuminated by laser. (b) bottom view.
Notes: Me-4PACz is nearly insoluble in water, which forms suspension and shows Tyndall effect. While 2PACz-K dissolves well in water and forms a clear solution.

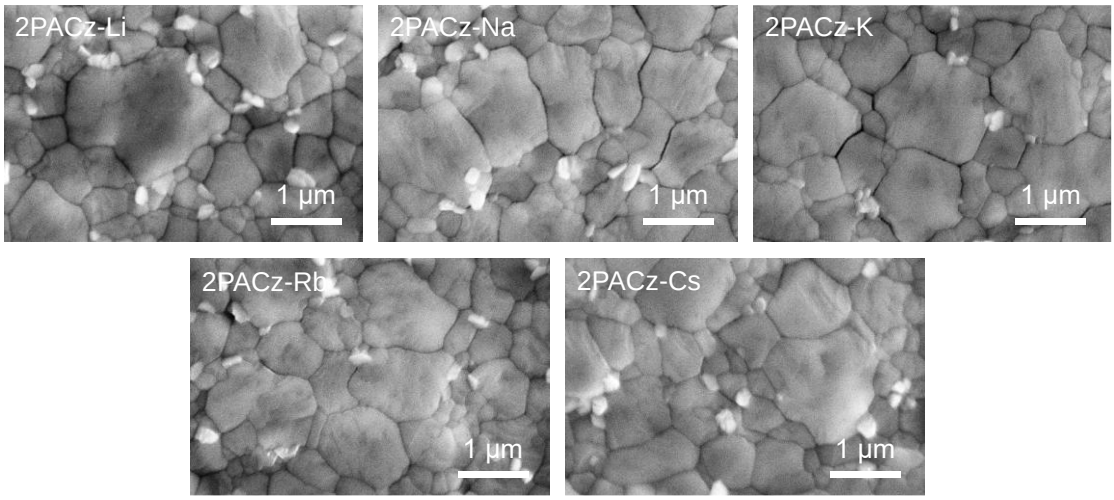

Supplementary Figure 27. SEM images of the top surface of perovskite on ITO/SAM. Herein, 2PACz-Li, 2PACz-Na, 2PACz-K, 2PACz-Rb and 2PACz-Cs aqueous solutions (1 mmol/L) are used to fabricate the SAM layer. Relatively large grains without pinholes or cracks are observed with a small amount of PbI_2.

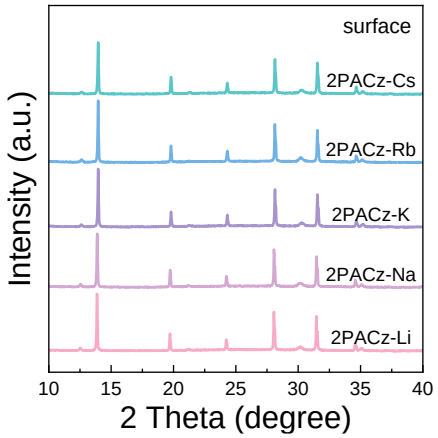

Supplementary Figure 28. XRD patterns of the top surface of perovskite on ITO/SAM. 2PACz-Li, 2PACz-Na, 2PACz-K, 2PACz-Rb and 2PACz-Cs aqueous solutions are used to fabricate the SAM layer.

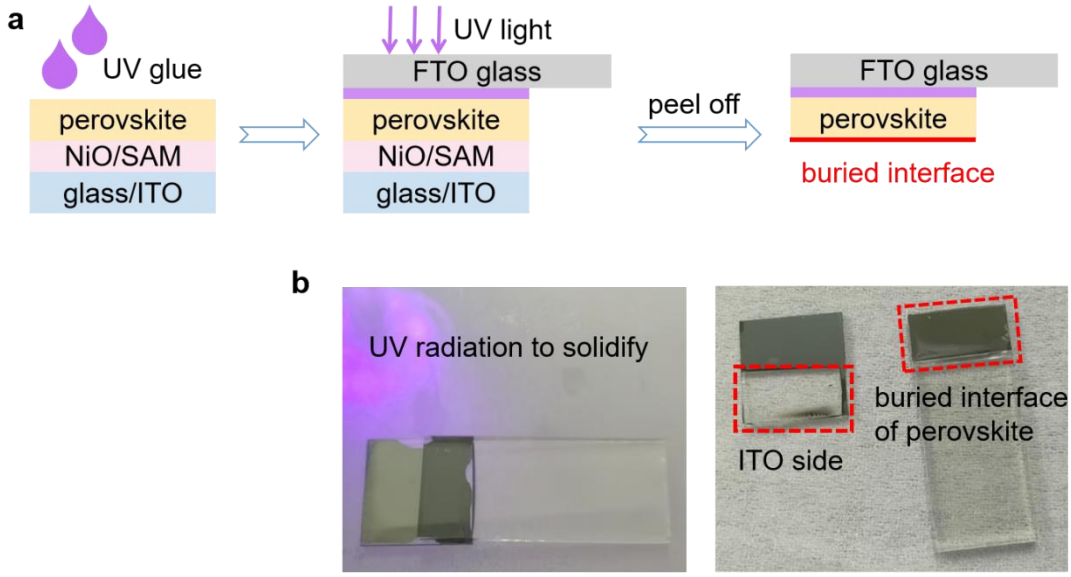

Supplementary Figure 29. (a) Illustration and (b) photos of peeling off perovskite for the buried interface.

Notes: First, drop some UV glue on the top surface of the perovskite film and then cover it with a FTO glass tightly, followed by UV radiation (365 nm, 1 W cm^{-2}) for 2-3 min to solidify. Subsequently, the perovskite film is peeled off from the substrate with force. The buried interface of perovskite is used for characterization.

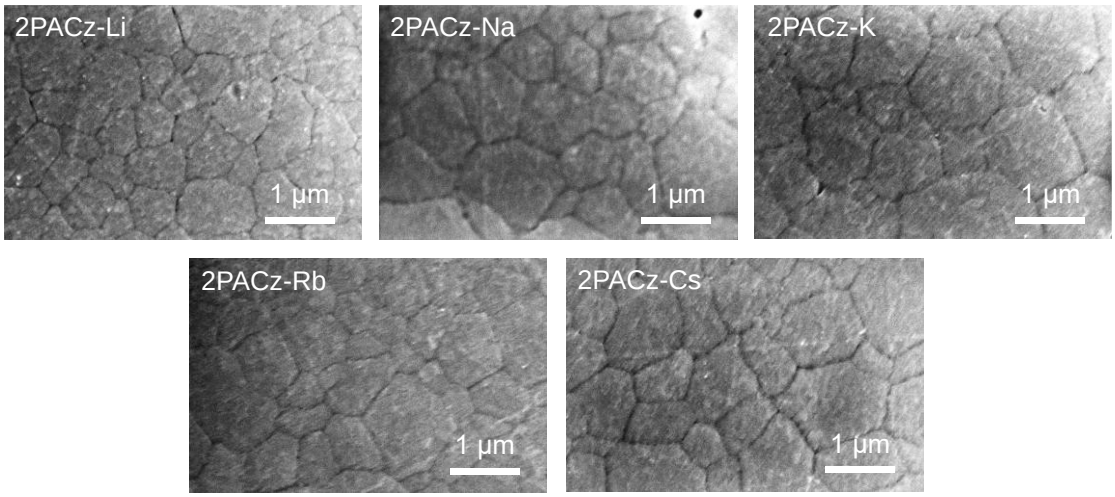

Supplementary Figure 30. SEM images of the buried interface of perovskite on ITO/SAM. Herein, 2PACz-Li, 2PACz-Na, 2PACz-K, 2PACz-Rb and 2PACz-Cs aqueous solutions are used to fabricate the SAM layer. Nearly no pinholes or cracks are observed, suggesting superior interfacial contact.

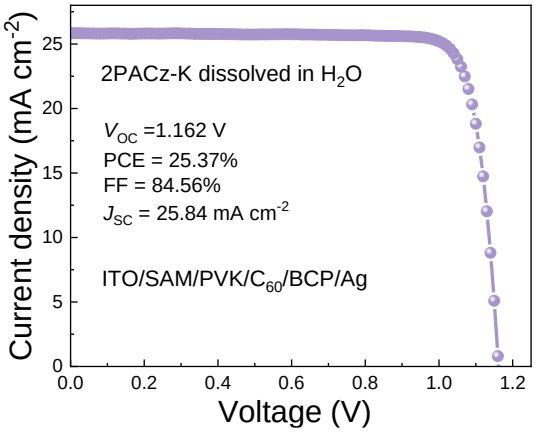

Supplementary Figure 31. *J-V* curve of champion device based on 2PACz-K.

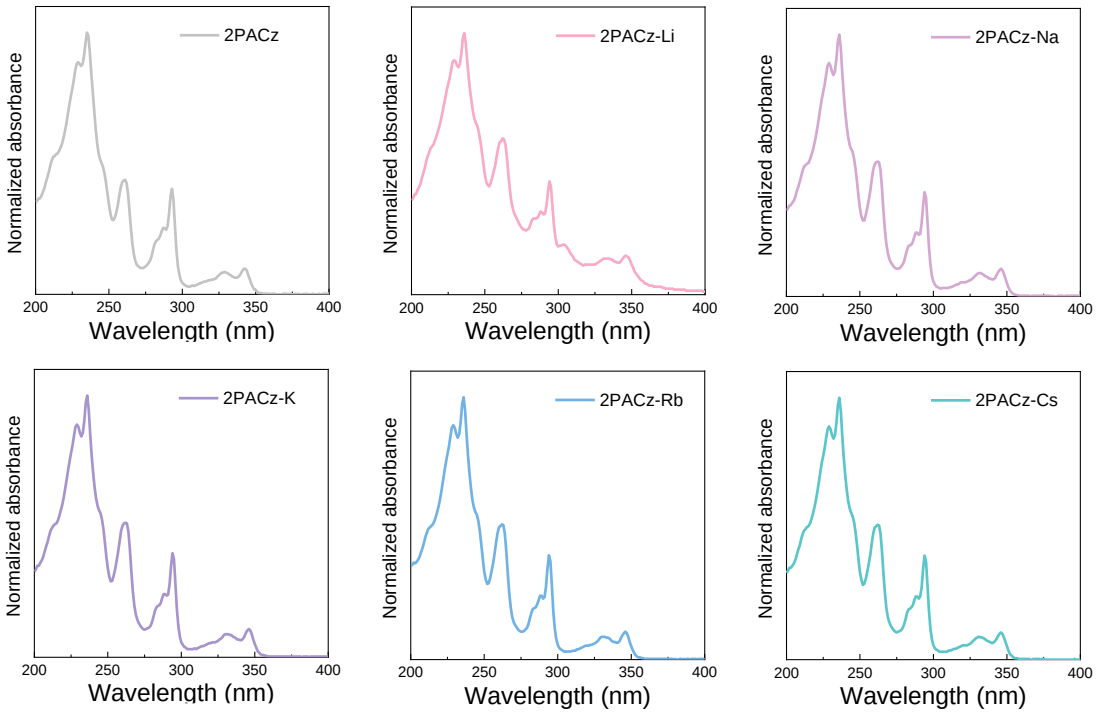

Supplementary Figure 32. UV-vis absorbance of SAMs in EtOH with the concentration of 10^{-4} mol/L.

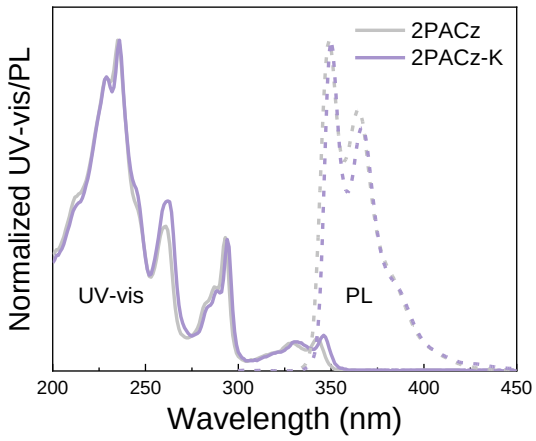

Supplementary Figure 33. UV-vis absorbance and PL spectra of 2PACz and 2PACz-K.

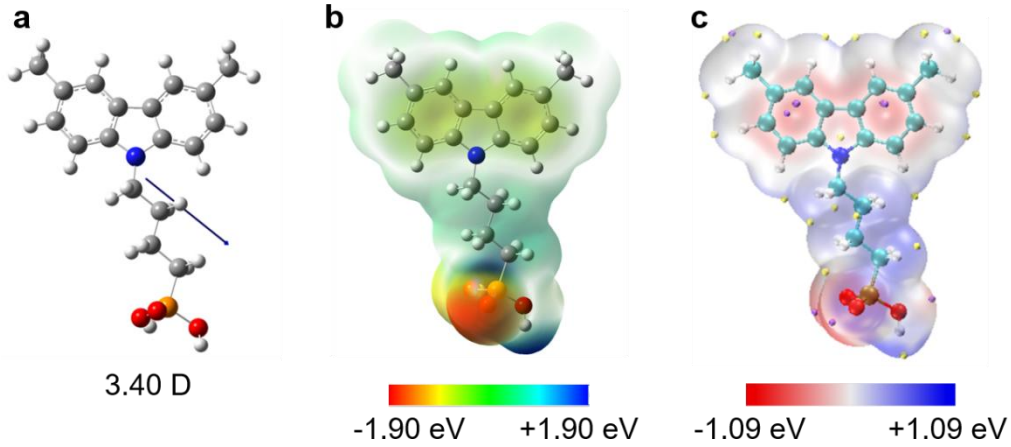

Supplementary Figure 34. (a) Optimized geometry and dipole moment of Me-4PACz. The dipole moment points from negative to positive charge. (b) ESP distribution of Me-4PACz of rainbow color matching. (c) ESP distribution of Me-4PACz of red-white-blue color matching. Purple and yellow spheres correspond to surface minima and maxima, respectively.

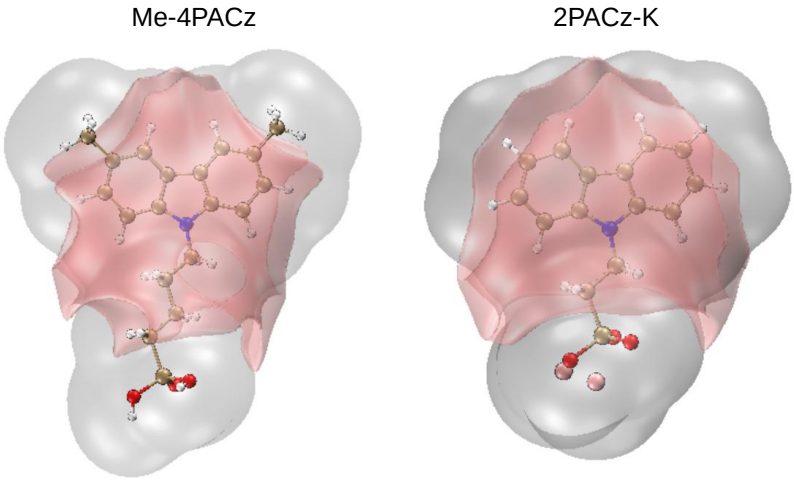

Supplementary Figure 35. Isosurface maps of van der Waals (vdW) potential of Me-4PACz and 2PACz-K with isovalue of 0.7 a.u. Gray and pink correspond to positive and negative parts, respectively.

Notes:

(i) Electrostatics and vdW interactions are two major parts of intermolecular interaction. Electrostatic potential has been used to describe electrostatic interaction between chemical species. Correspondingly, vdW potential is a complement of ESP to investigate intermolecular interactions which is dominant by vdW interaction[11].

(ii) The pink isosurface represents the region where vdW potential is negative. In this region, dispersion attraction effect surpasses exchange-repulsion effect, since the former and the latter have negative and positive contributions to the vdW potential, respectively. SAM molecules tend to interact with other species via the pink region due to the driven force of dispersion attraction.

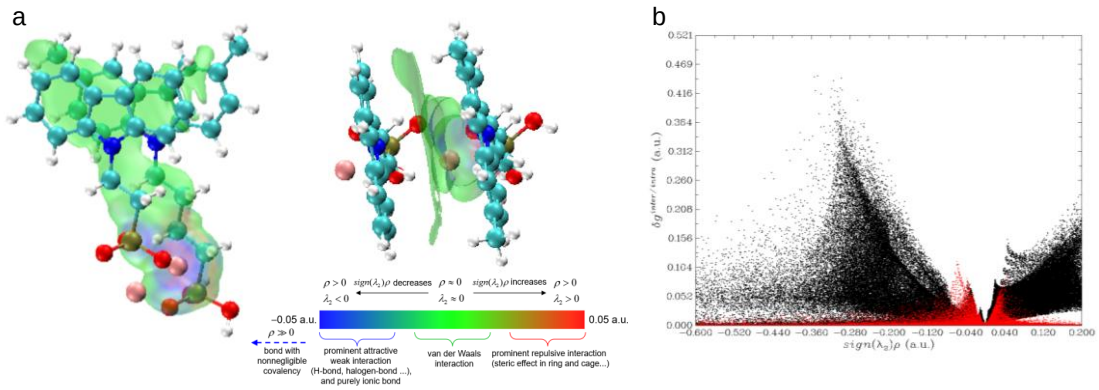

Supplementary Figure 36. IGM analyses of Me-4PACz and 2PACz-K. (a) Front and top view of IGM maps of δg^{inter} with isosurface of 0.001 a.u. (b) Scatter plot of δg^{inter} (red area) and δg^{intra} (black area).

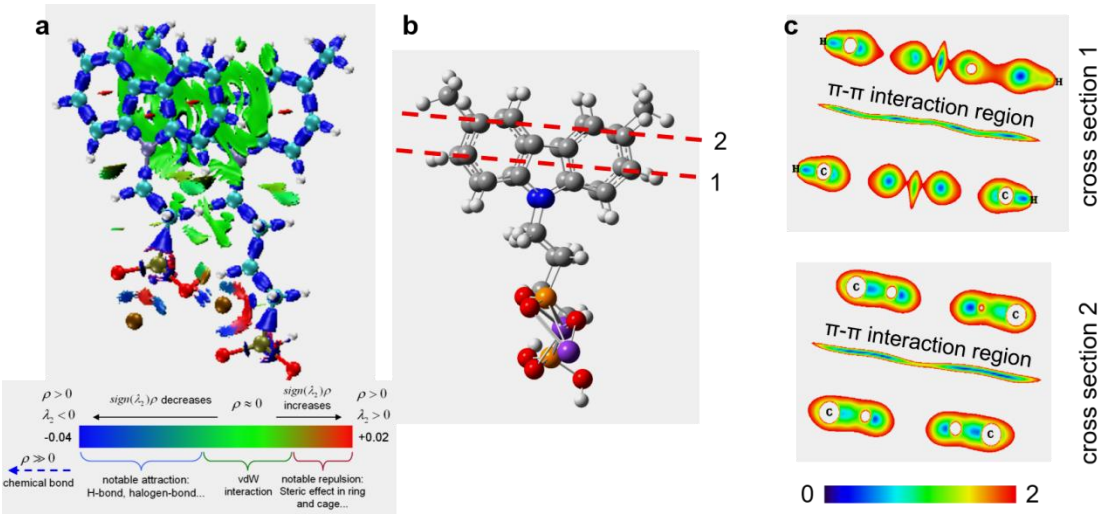

Supplementary Figure 37. IRI analyses of Me-4PACz and 2PACz-K. (a) Side view of IRI map with isosurface of 1.0 a.u. The green isosurface demonstrates the π-π interaction. (b) Diagram of chemical structure skeleton and cross section position. (c) Color-filled maps of IRI at the two cross section planes.

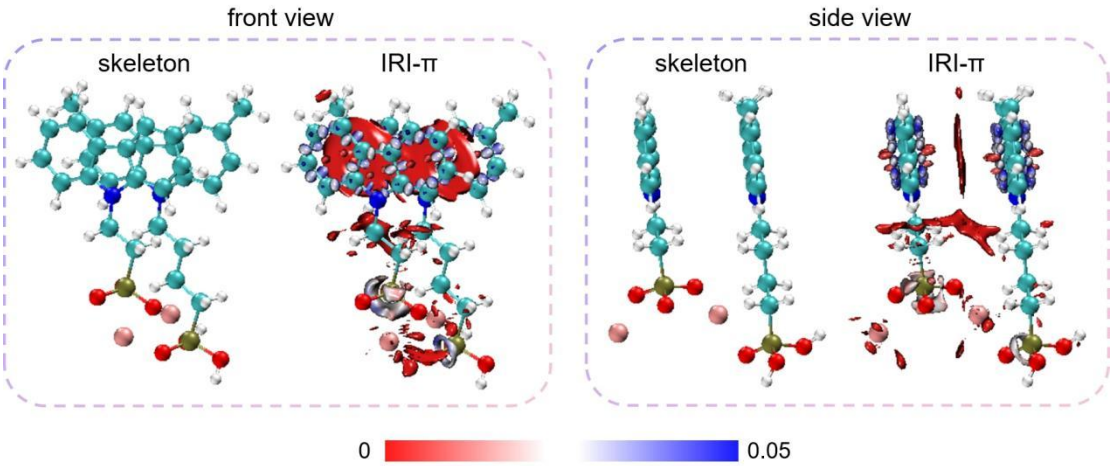

Supplementary Figure 38. Front and side view of chemical structure skeleton and IRI-π maps for Me-4PACz and 2PACz-K[8]. π-electron density is mapped onto the isosurfaces of IRI-π according to the color bar with isovalue of 1.5 a.u. The red isosurface between two carbazole rings indicates the π-π interaction.

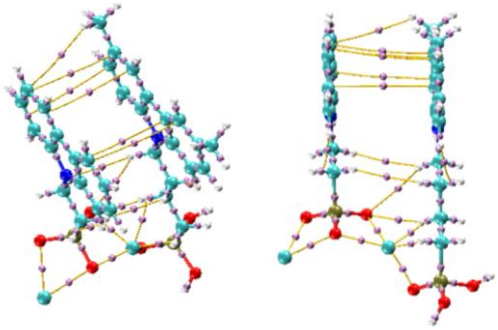

Supplementary Figure 39. Topology analyses on electron density of Me-4PACz and 2PACz-K based on AIM theory. Yellow lines are bond paths, and purple spheres correspond to the (3,-1) critical points. Bond paths and critical points are observed between the carbazole rings of Me-4PACz and 2PACz-K.

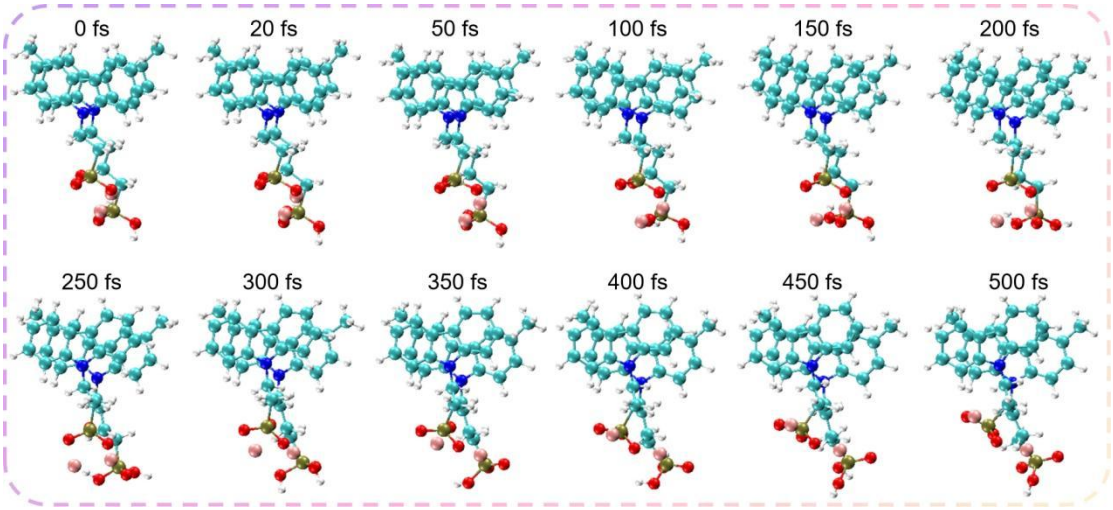

Supplementary Figure 40. The *ab-initio* molecular dynamics trajectories simulated at 300 K for Me-4PACz and 2PACz-K. The optimized structure corresponds to the first frame of the trajectories. The full trajectory is in Supplementary Movie 2.
Notes: During the 500 fs simulation, Me-4PACz and 2PACz-K maintain the configuration of π-π stacking, and their dissociation is not observed, confirming the strong interaction between Me-4PACz and 2PACz-K.

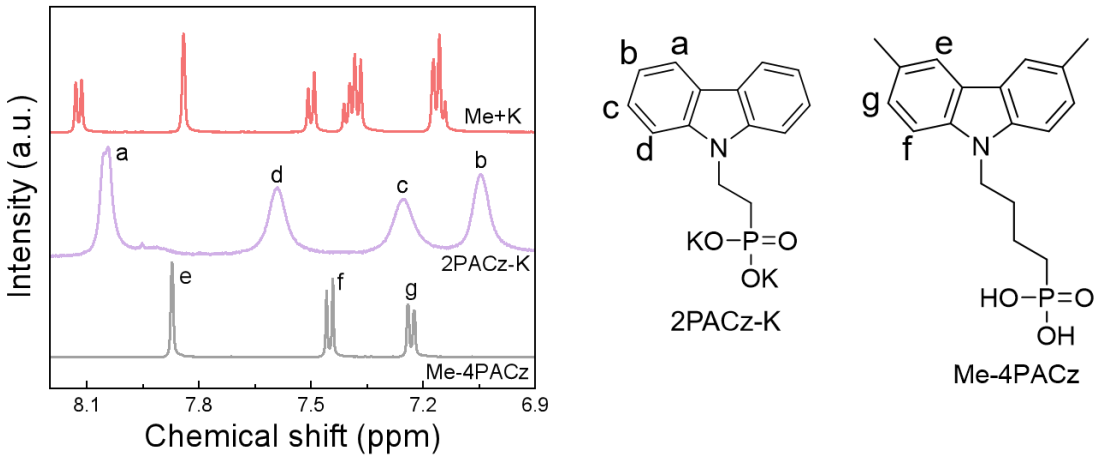

Supplementary Figure 41. Enlarged ^{1}H-NMR liquid-state spectra in d_6-DMSO for Me-4PACz, 2PACz-K and Me-4PACz+2PACz-K (denoted as Me+K). The hydrogen atoms on carbazole rings are labeled by letters in the chemical structure.

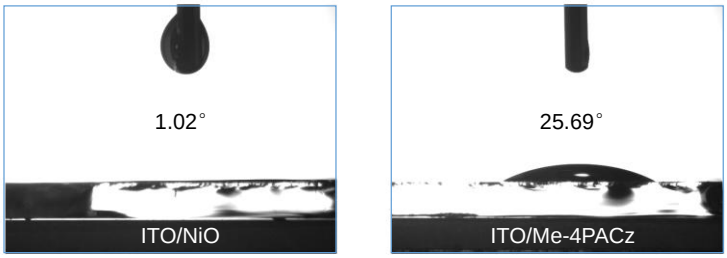

Supplementary Figure 42. Contact angle measurements of NiO_x and Me-4PACz on ITO. The dropped solution is DMF and DMSO (volume 4:1).

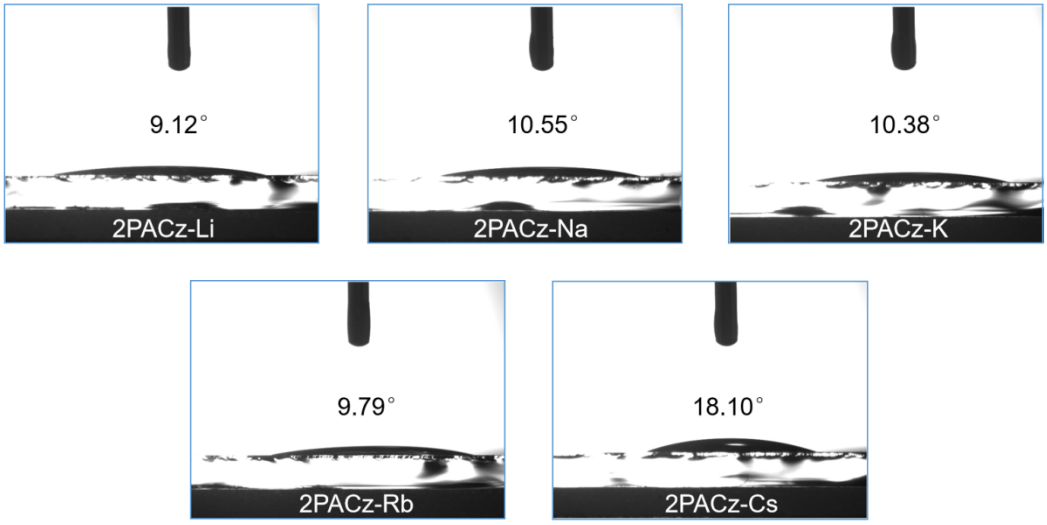

Supplementary Figure 43. Contact angle measurements of 2PACz-Li, 2PACz-Na, 2PACz-K, 2PACz-Rb and 2PACz-Cs on ITO. The dropped solution is DMF and DMSO (volume 4:1).

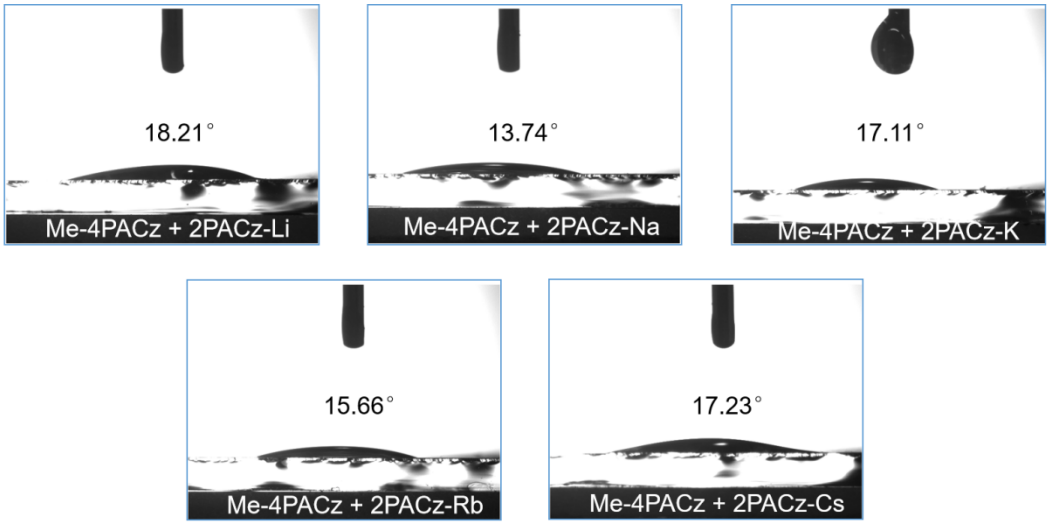

Supplementary Figure 44. Contact angle measurements of mixed SAMs on ITO. The dropped solution is DMF and DMSO (volume 4:1). The mole ratio of Me-4PACz and 2PACz-M is 1:1 with the total concentration of 1 mmol/L.

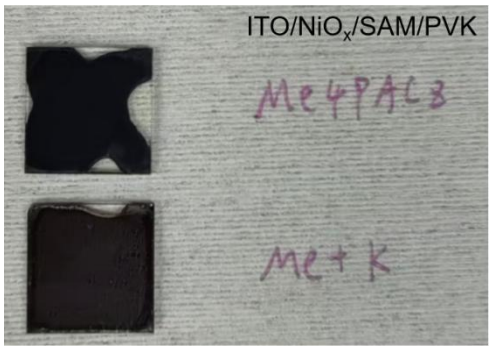

Supplementary Figure 45. Photos of perovskite films on different SAMs. The perovskite film on Me-4PACz shows incomplete coverage, while that on Me-4PACz+2PACz-K shows significantly improved coverage.

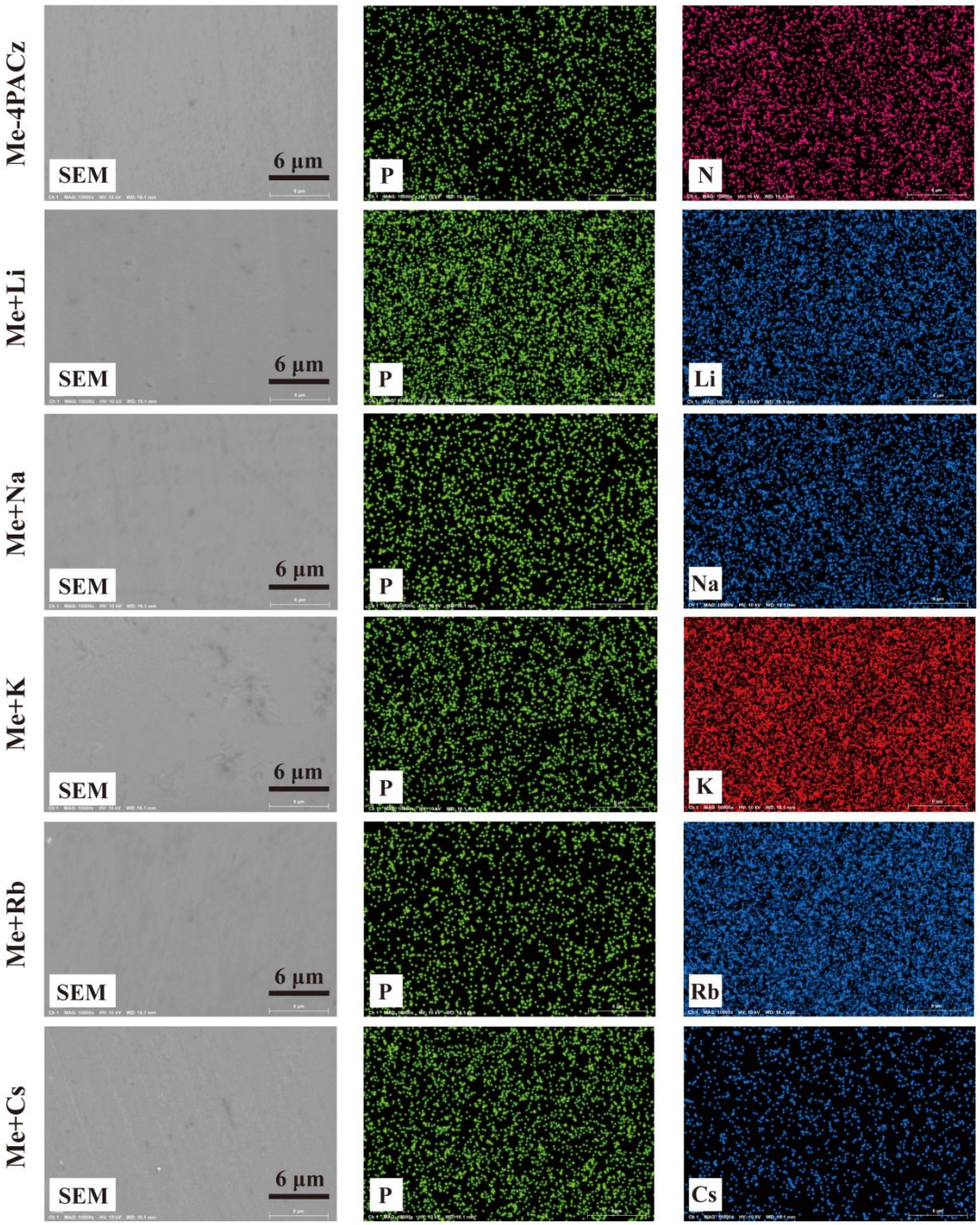

Supplementary Figure 46. SEM-EDX analyses of ITO/NiO_x/SAM.

Notes: The P and N signals of Me-4PACz are not uniform, indicating its agglomeration and corresponding uncovered area. While enhanced P signals and uniform distribution of K signals of Me-4PACz+2PACz-K imply suppressed SAM agglomeration and better coverage.

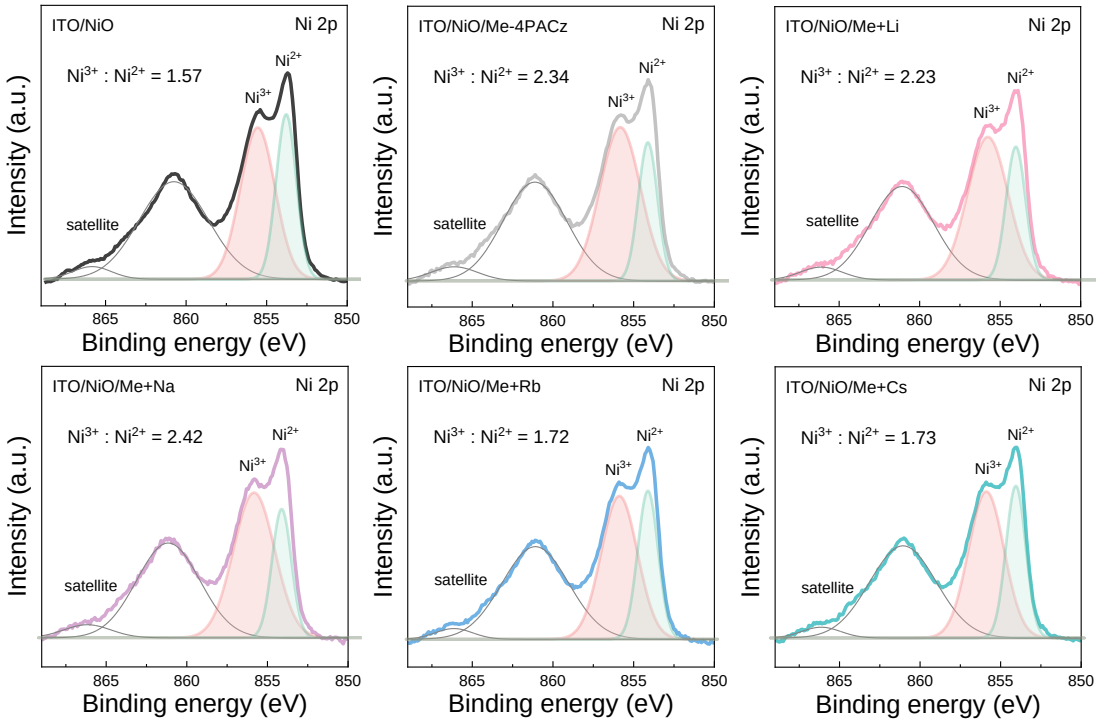

Supplementary Figure 47. High-resolution XPS spectra of Ni 2p core level.

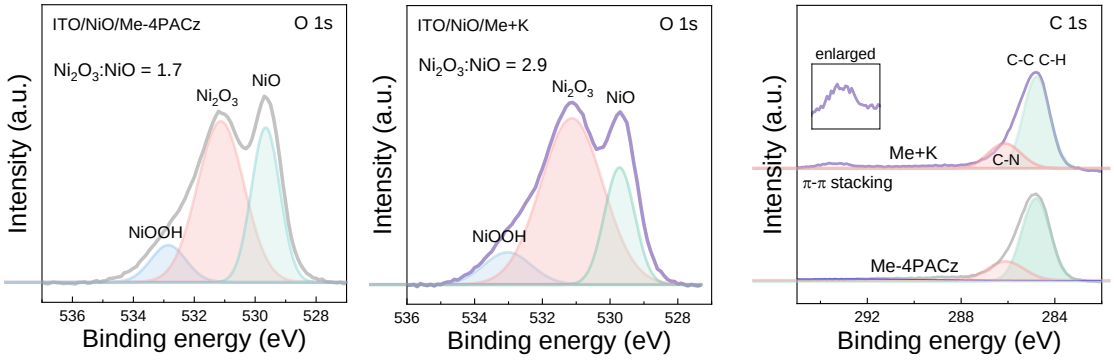

Supplementary Figure 48. High-resolution XPS spectra of O 1s and C 1s core level. Notes: The Ni^{3+}/Ni^{2+} ratio (Ni_2O_3/NiO_x) of O 1s peak of Me+K is higher than that of Me-4PACz. In the XPS spectra of C 1s, 2PACz-K and Me-4PACz show π-π interaction.

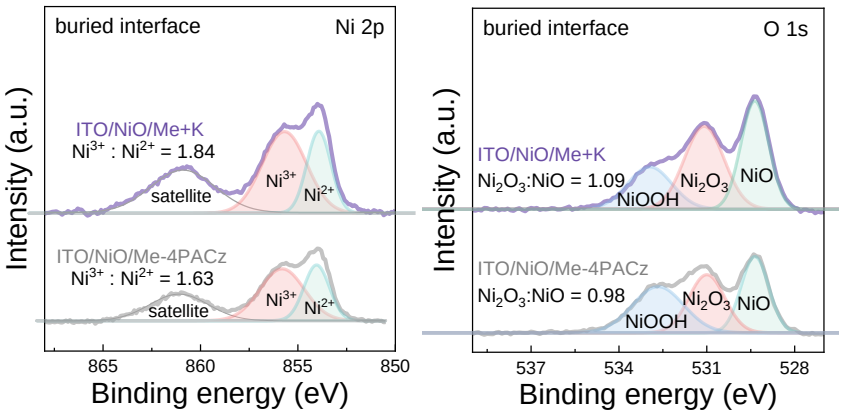

Supplementary Figure 49. High-resolution XPS spectra of Ni 2p and O 1s core level of buried interface of perovskite.
Notes: (i) For Me+K, the Ni 2p peak area increases, implying more inseparable interface contact and enhanced adhesion force, confirming strengthened interfacial coupling for extreme mechanical durability. (ii) The NiOOH peak area decreases for Me+K, which indicates fewer trap states. (iii) The Ni^{3+}/Ni^{2+} ratio increases for Me+K, leading to improved conductivity of NiO_x.

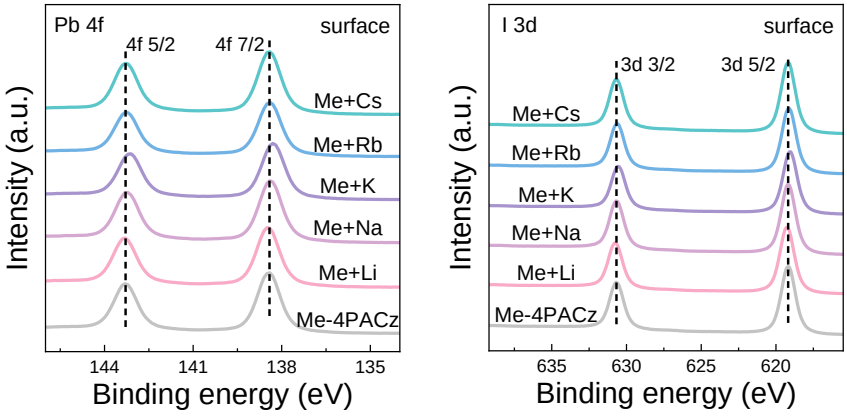

Supplementary Figure 50. High-resolution XPS spectra of Pb 4f and I 3d core level of top surface of the perovskite on ITO/NiO_x/SAM. The peaks of Pb 4f and I 3d spectra slightly shift to lower binding energies due to the interaction between Pb^{2+} and the carbazole moieties of 2PACz-K.

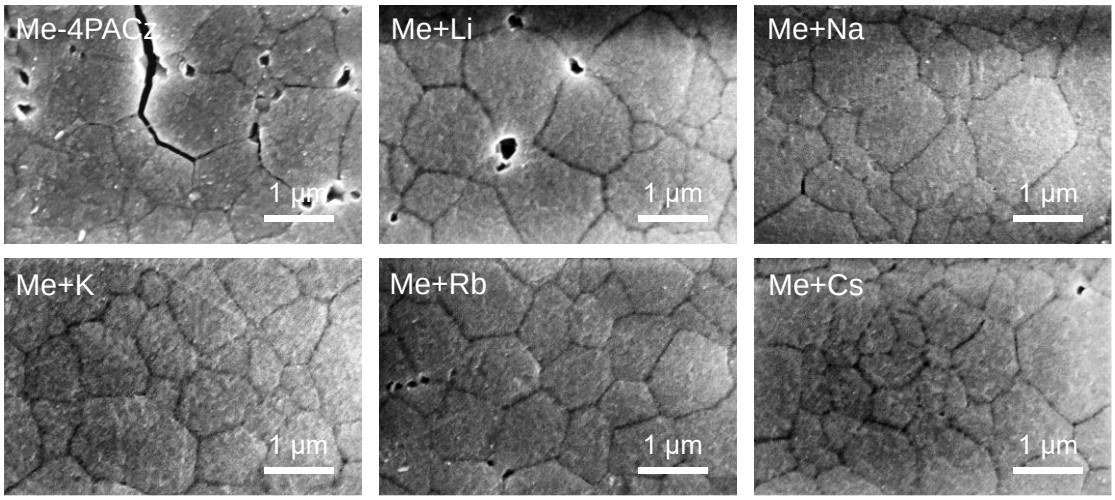

Supplementary Figure 51. SEM images of the buried interface of perovskite on ITO/NiO_x/SAM.

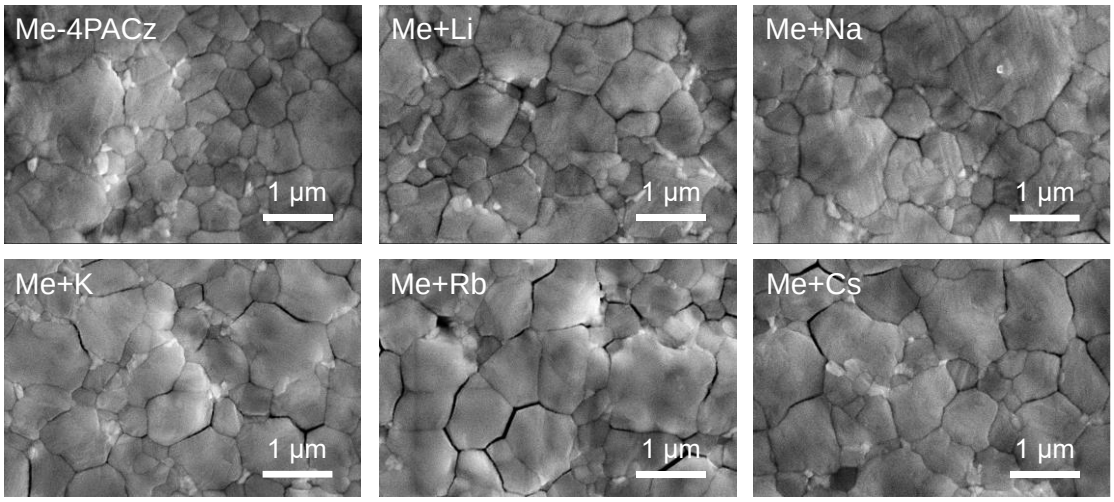

Supplementary Figure 52. SEM images of the top surface of perovskite on ITO/NiO_x/SAM. The perovskite films based on Me+M show larger grains than that of Me-4PACz.

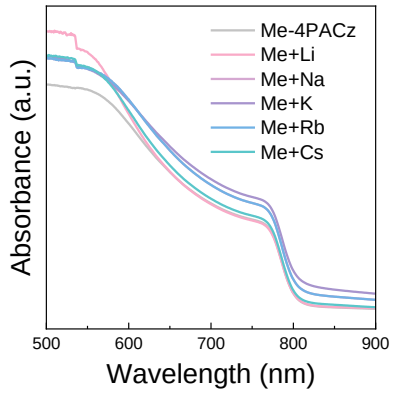

Supplementary Figure 53. UV-vis absorbance of the perovskite films on ITO/NiO_x/SAM. The perovskite film based on Me+K exhibits increased absorbance than that of Me-4PACz, indicating enhanced crystal quality.

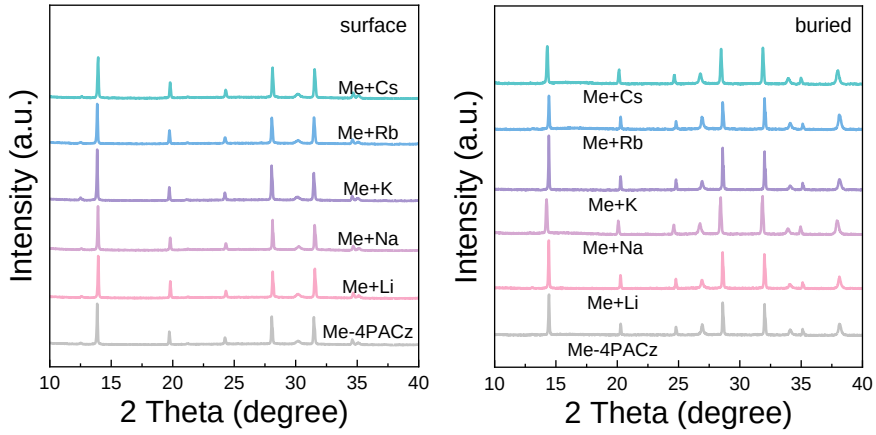

Supplementary Figure 54. XRD patterns of perovskite on ITO/NiO_x/SAM.

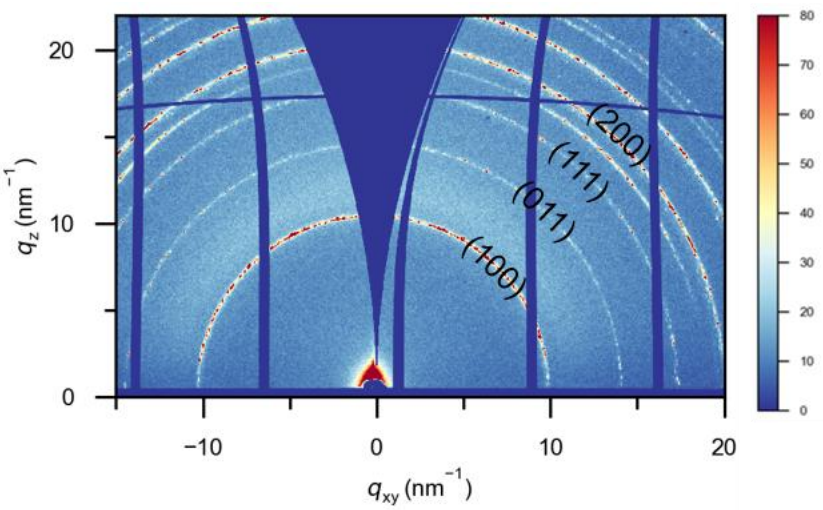

Supplementary Figure 55. GIWAXS two-dimensional maps of the buried interface for peeled off perovskite film based on ITO/NiO_x/Me-4PACz+2PACz-K.

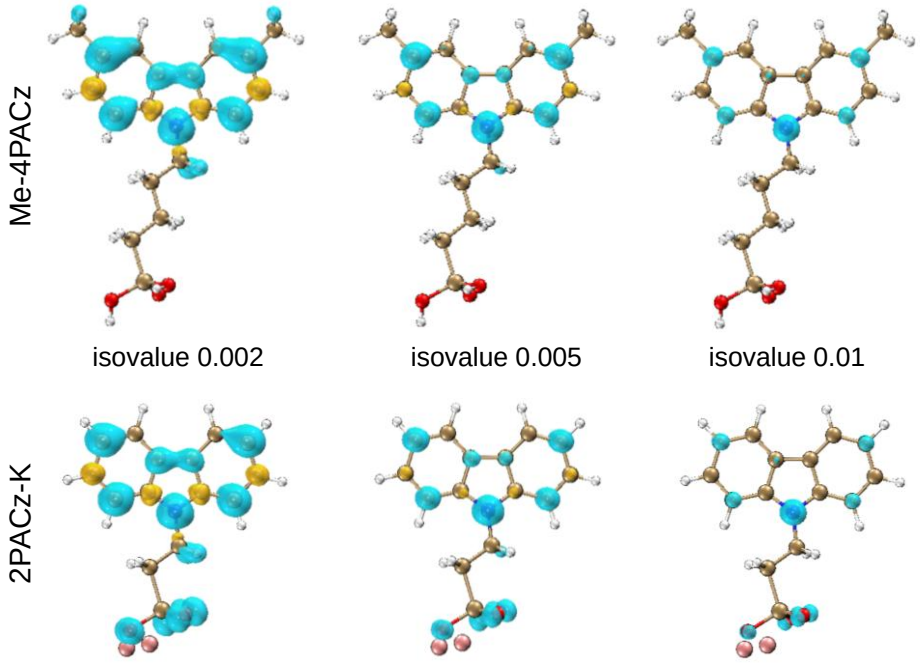

Supplementary Figure 56. Spin density isosurface maps of Me-4PACz and 2PACz-K with different isovalues. The blue and yellow isosurfaces correspond to alpha and beta electrons.

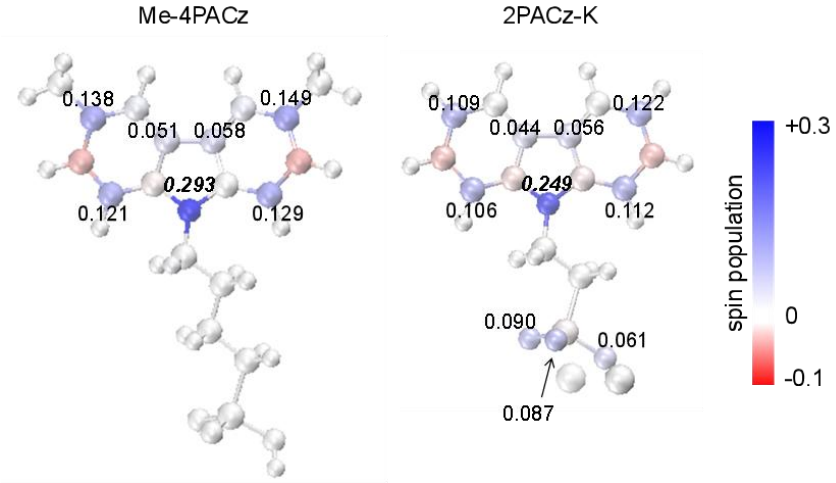

Supplementary Figure 57. The spin population of Me-4PACz and 2PACz-K. Only the values with main contribution (exceed 5% of the total spin population) are labeled. The spin population is quantitatively characterized by Hirshfeld spatial segmentation method.

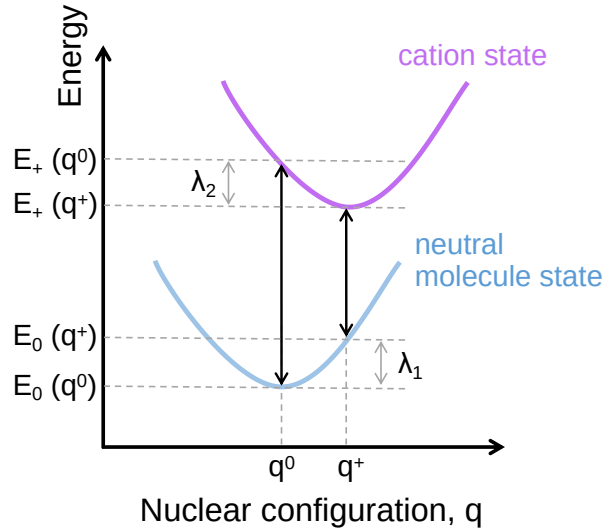

Supplementary Figure 58. Schematic diagram for calculating the dimer reorganization energy (ROE) based on Marcus theory.

Notes: Marcus theory elucidates charge transfer (CT) process and its kinetics[12-13]. Based on density functional theory (DFT) calculations, "Koopmans' theorem-energy splitting in dimer" (KT-ESD) method and the 4-point method are used to calculate the electronic coupling and reorganization energy in order to compare charge transfer rates of different molecules.

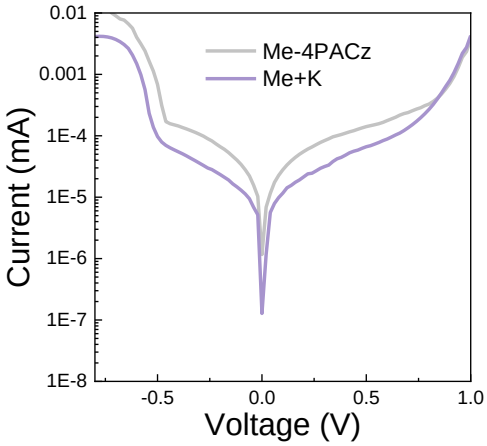

Supplementary Figure 59. Current leakage curves of PSCs devices under dark.

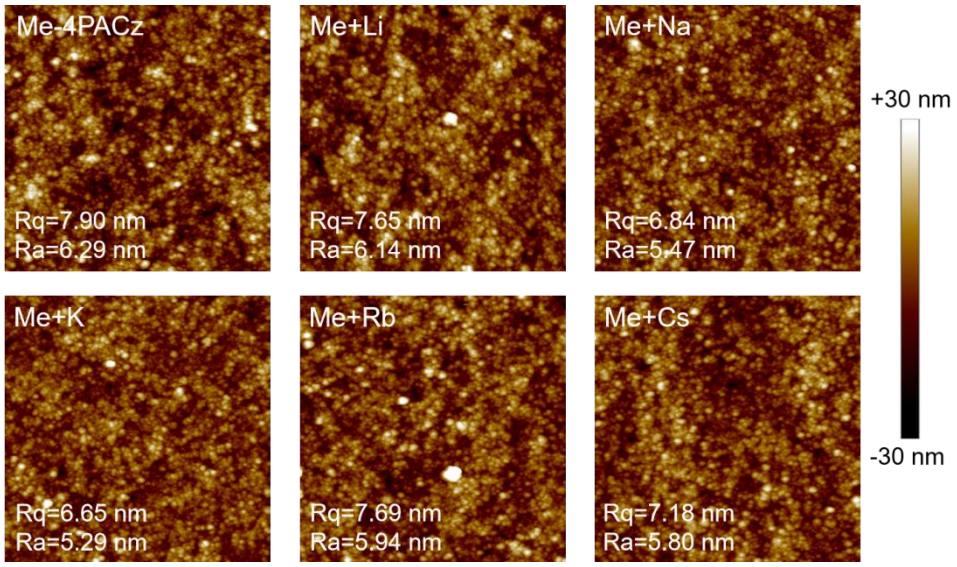

Supplementary Figure 60. AFM images of ITO/NiO_x/SAMs with an area of 3 μm × 3 μm. R_a and R_q refer to arithmetic mean roughness and root mean square roughness, respectively.

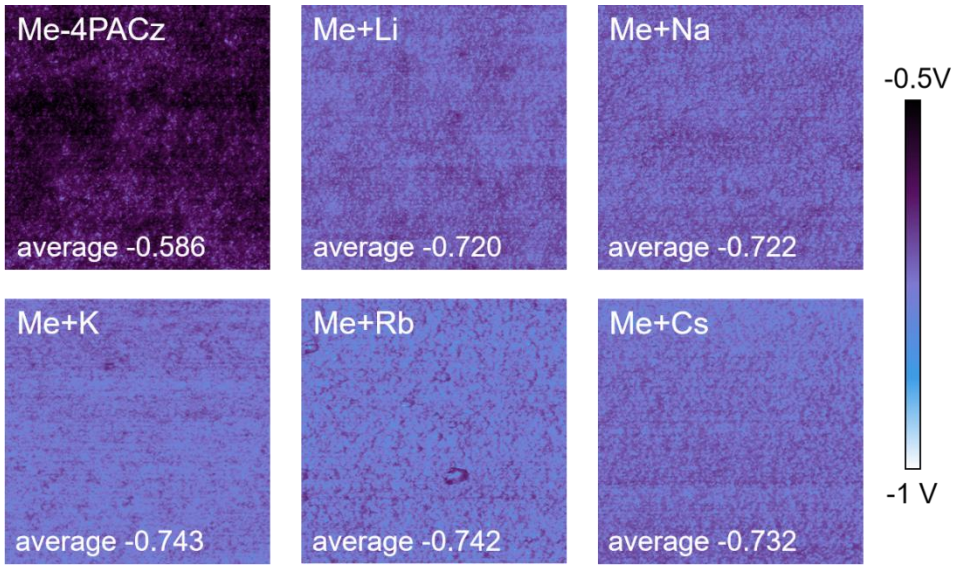

Supplementary Figure 61. KPFM images of ITO/NiO_x/SAMs with an area of 3 μm × 3 μm.

Notes: Topographic and electrical surface potential profiles were measured concurrently using KPFM operating in the Tapping mode. The contact potential difference (CPD) between the sample and a Pt-Ir coated conductive probe (Nanosensors PPP-EFM-20) was quantified via applying an AC bias and employing a nullifying feedback loop.

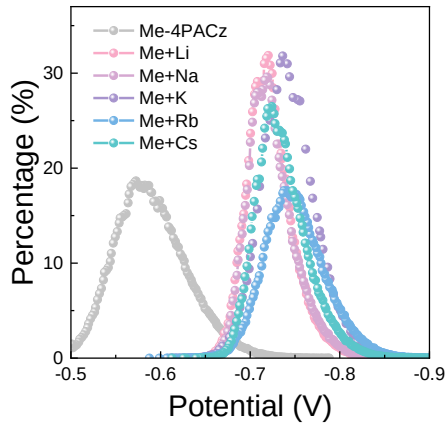

Supplementary Figure 62. Potential distributions of ITO/NiO_x/SAMs.

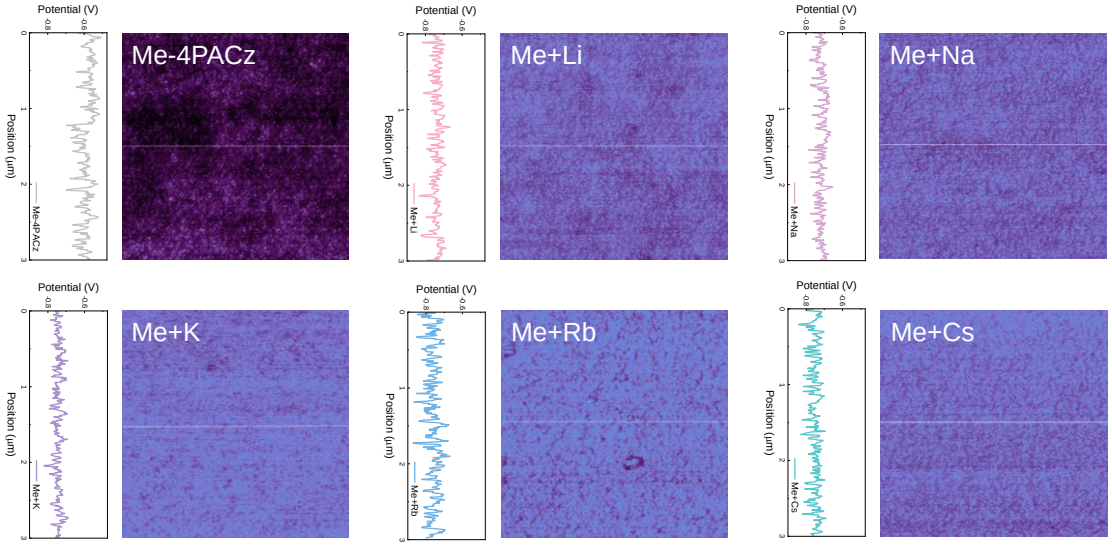

Supplementary Figure 63. KPFM images and corresponding lines of ITO/NiO_x/SAMs.

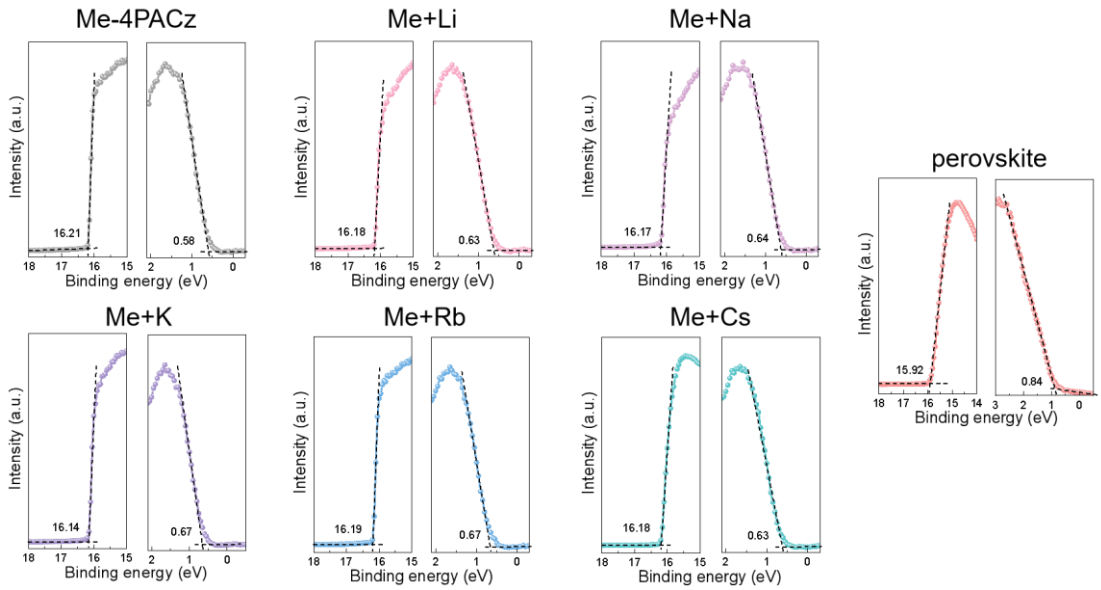

Supplementary Figure 64. UPS spectra in the cutoff and the onset region of SAMs and perovskite.

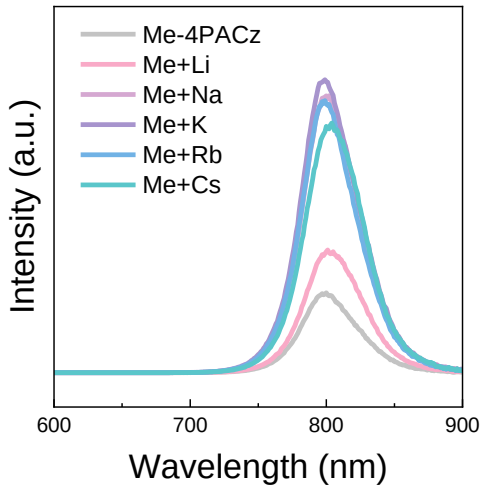

Supplementary Figure 65. Steady-state PL spectra of perovskite on ITO/NiO_x/SAMs.

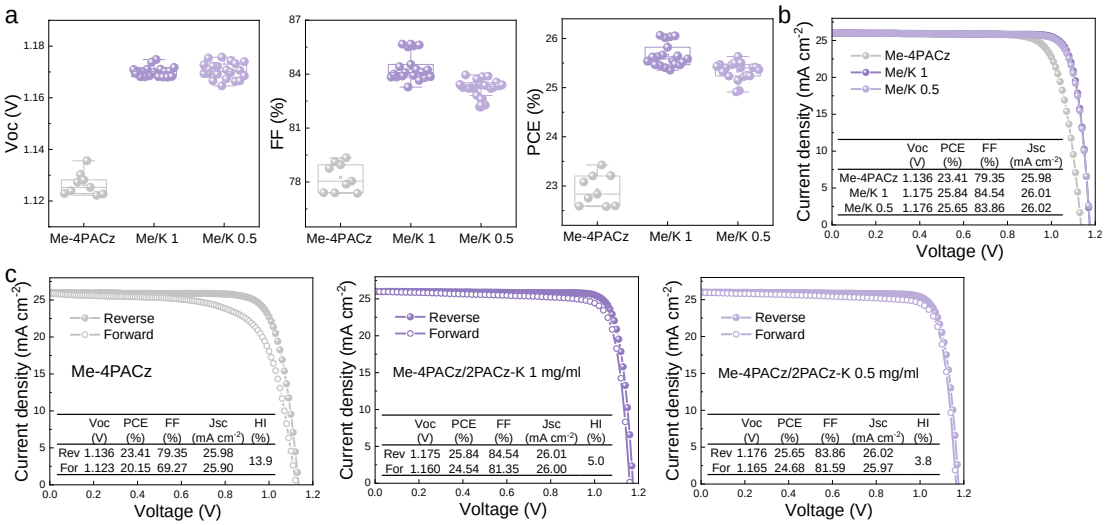

Supplementary Figure 66. Device performance with sequential deposited SAMs. (a) The statistical distribution of V_{OC}, FF and PCE of devices. (b) *J-V* characteristics of the champion devices under reverse scan. (c) *J-V* characteristics under reverse and forward scan. HI refers to hysteresis index. Herein, "Me/K 1" refers to depositing Me-4PACz (with annealing and cooling down) followed by depositing 1 mg/ml 2PACz-K and annealing. "Me/K 0.5" refers to depositing Me-4PACz (with annealing and cooling down) followed by depositing 0.5 mg/ml 2PACz-K and annealing.

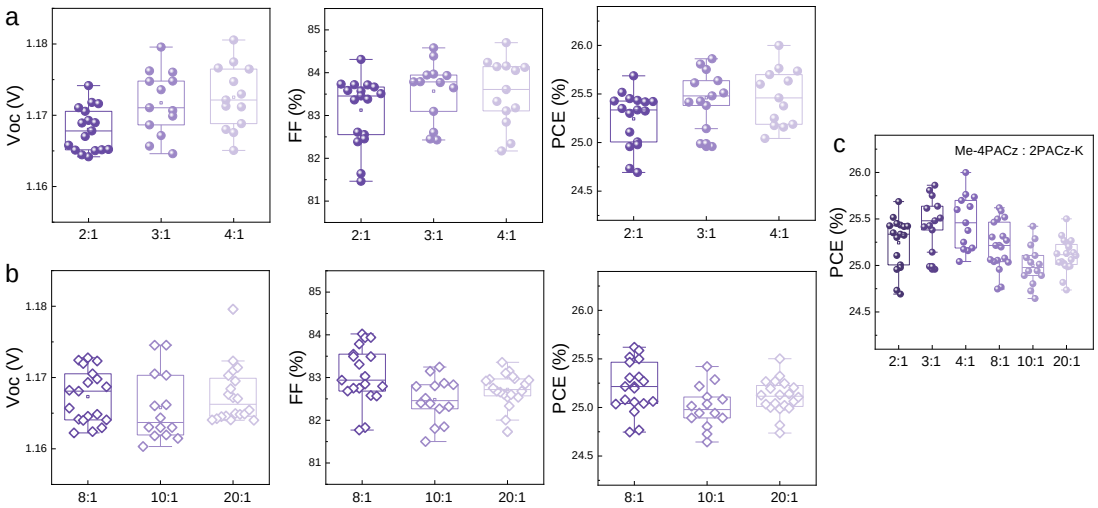

Supplementary Figure 67. (a,b) The statistical distribution of V_{OC}, FF and PCE of devices based on mixing Me-4PACz and 2PACz-K with different ratios. (c) The statistical distribution of PCE for easy comparison.

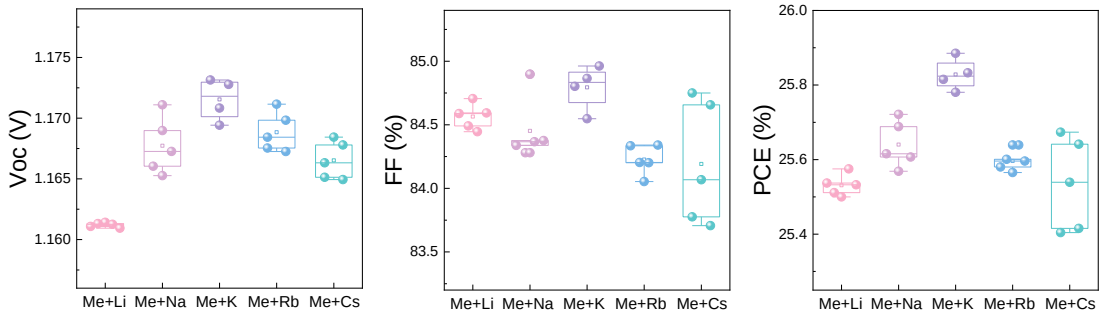

Supplementary Figure 68. The statistical distribution of V_{OC}, FF and PCE of devices based on mixed SAMs. The ratio of Me-4PACz and 2PACz-M (Me+M) is 4:1.

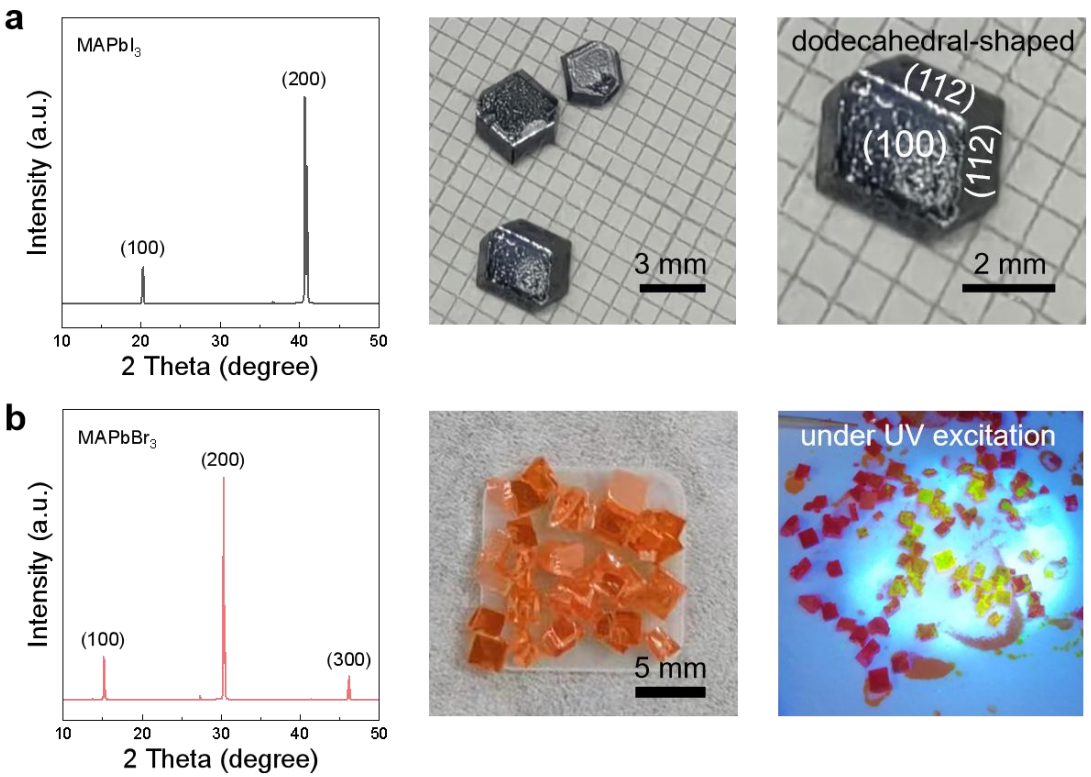

Supplementary Figure 69. (a) XRD pattern and photos of $MAPbI_3$ single crystals. (b) XRD pattern and photos of $MAPbBr_3$ single crystals. Bright yellow green fluorescence is observed under UV excitation at room temperature, indicating relatively few defects in these single crystals in comparison with polycrystalline perovskite.

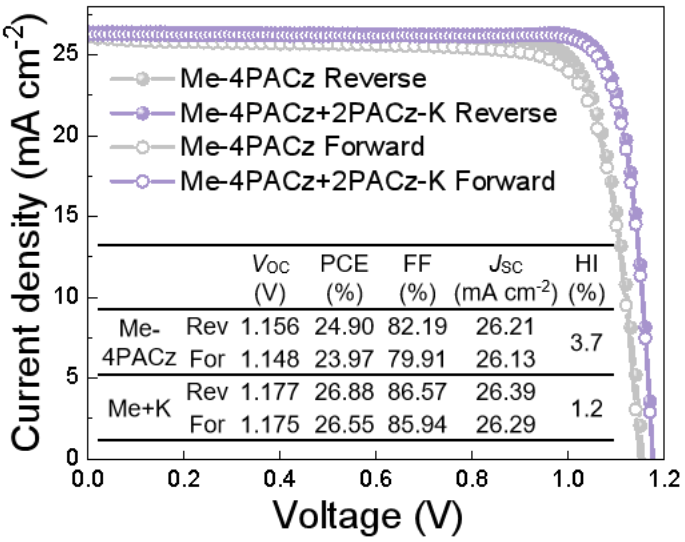

		V_{OC} (V)	PCE (%)	FF (%)	J_{SC} (mA cm^{-2})	HI (%)
Me-4PACz	Rev	1.156	24.90	82.19	26.21	3.7
	For	1.148	23.97	79.91	26.13	
Me+K	Rev	1.177	26.88	86.57	26.39	1.2
	For	1.175	26.55	85.94	26.29	

Supplementary Figure 70. *J-V* characteristics of the champion devices under reverse and forward scan. The devices are fabricated with presynthesized $MAPbI_3$ single crystals and commercial $FAPbI_3$, $CsPbI_3$ nanocrystals.

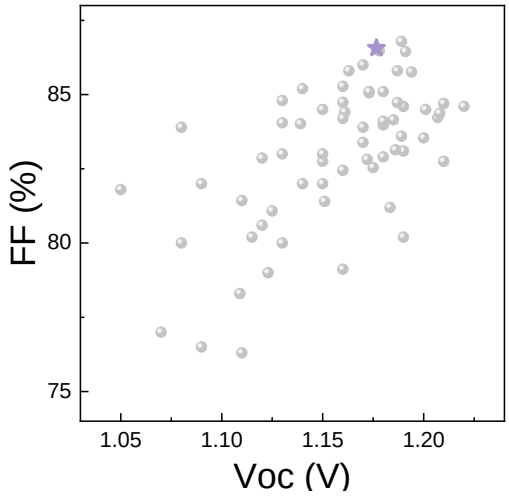

Supplementary Figure 71. PCE and V_{OC} records of single-junction inverted PSCs based on SAMs. This work is marked by the purple star.

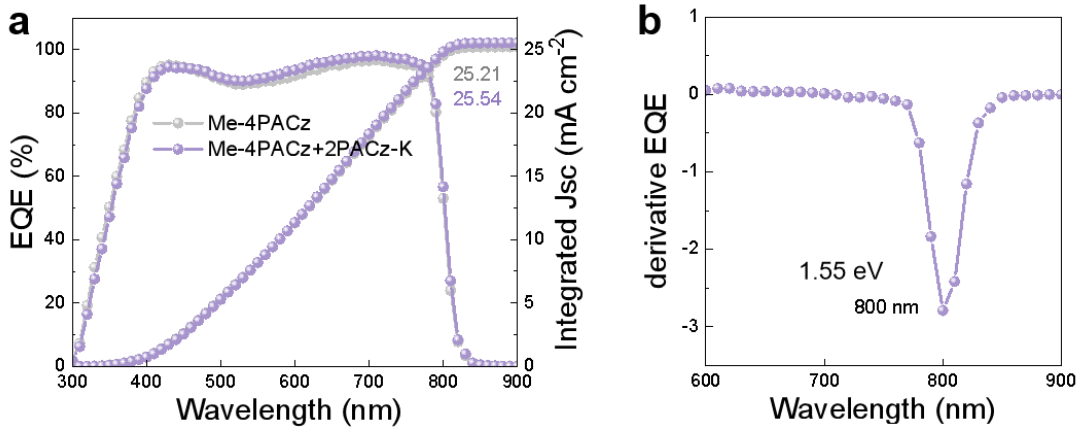

Supplementary Figure 72. (a) EQE spectra of champion devices based on Me-4PACz and Me-4PACz+2PACz-K. (b) Derivative EQE spectrum.

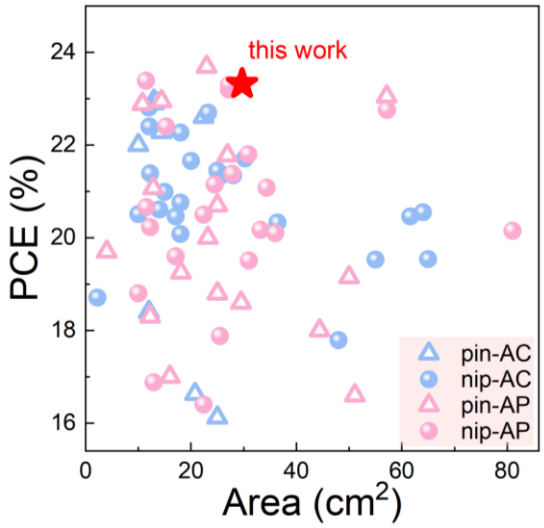

Supplementary Figure 73. PCE records of modules of different area. AC refers to active area and AP refers to aperture area.

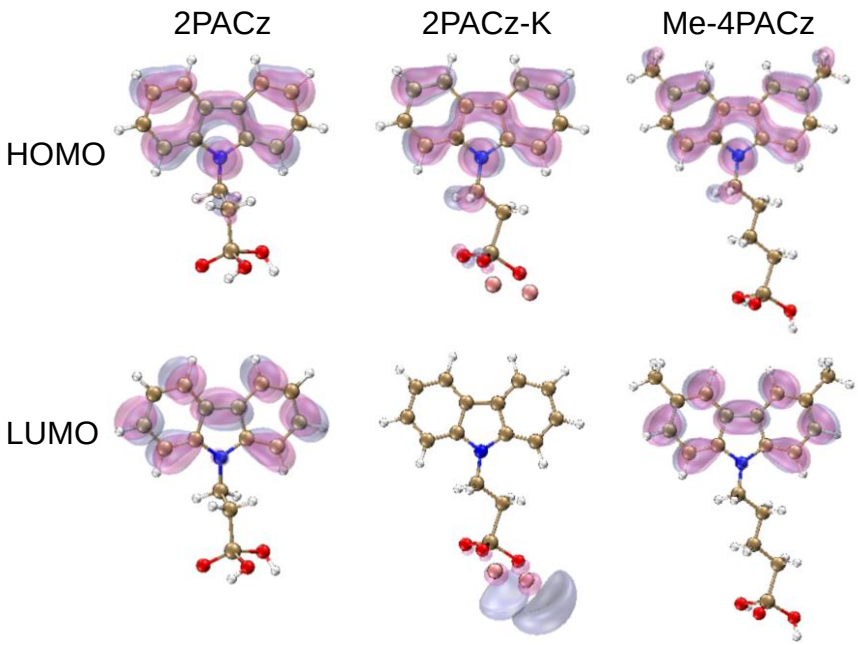

Supplementary Figure 74. Visualization wave functions of the highest occupied molecular orbitals (HOMO) and the lowest unoccupied molecular orbitals (LUMO) of 2PACz, 2PACz-K and Me-4PACz. The isovalue is 0.03 a.u. Herein, 2PACz is introduced for comparison to signify the effect of phosphonate group.

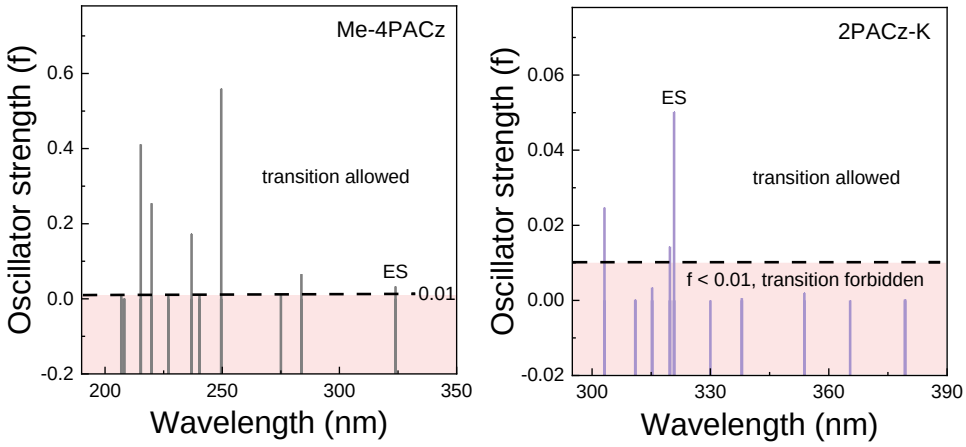

Supplementary Figure 75. The oscillator strength (*f*) of the first 10 excited states of Me-4PACz and 2PACz-K based on time-dependent DFT (TD-DFT) calculation. S_1 to S_{10} states are arranged with increased energy. ES is short for the crucial excited state.
Notes: When oscillator strength is larger than 0.01, the transition from ground state (S_0) to excited state is allowed (i.e., bright state), otherwise the transition is forbidden (i.e., dark state). The white and pink area corresponds to bright and dark state respectively. The crucial excited state (i.e., the bright state with the lowest energy) is S_1 for Me-4PACz and S_6 for 2PACz-K, respectively.

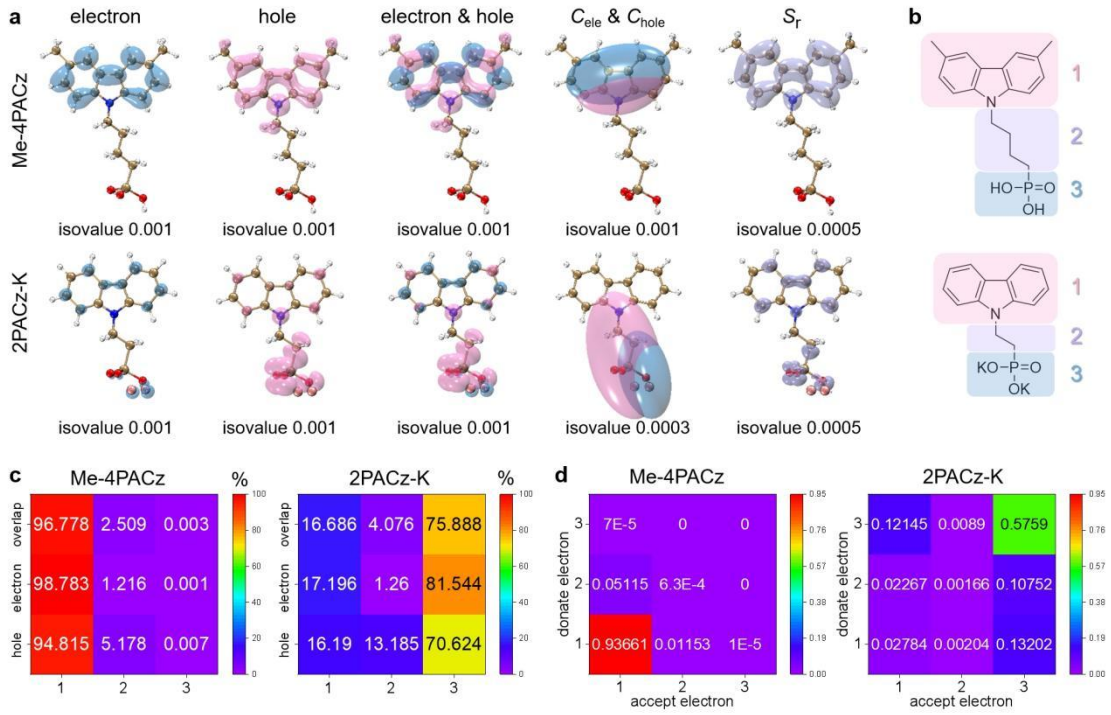

Supplementary Figure 76. Excited-state characteristics and electronic transition behavior for the crucial excited state of Me-4PACz and 2PACz-K. (a) The distributions of electron, hole, electron & hole, C_{ele} & C_{hole} and S_r. (b) The fragments divided for hole-electron analyses. Fragments 1, 2 and 3 represent the carbazole, alkyl and phosphonate groups, respectively. (c) Heat maps of hole and electron distributions for the three fragments. (d) Heat maps of interfragment charge transfer (IFCT) for the three fragments.

Notes:

(i) In Supplementary Figure 76a, the C_{hole} and C_{ele} functions are defined to make visual study of hole and electron easier[14]. S_r is a function to characterize the overlapping extent of hole and electron and S_r index is integral of S_r function[14]. D index is defined as the total magnitude of charge transfer length. Specifically, Me-4PACz exhibits the S_r index of 0.73682 a.u. and D index of 0.454 Angstrom, while 2PACz-K exhibits the S_r index of 0.26178 a.u. and D index of 2.108 Angstrom. 2PACz-K has smaller S_r index and larger D index than Me-4PACz, indicating less overlapped electron and hole.

(ii) In Supplementary Figure 76b-c, the hole and electron are mainly located on fragment 1 in Me-4PACz and no significant separation of the hole and electron is observed. Oppositely, the hole and electron disperse on fragment 1 and 3 in 2PACz-K.

(iii) In Supplementary Figure 76d, IFCT analyses indicate the charge transfer direction. The electron redistribution phenomenon is prominent in the fragment 1 of Me-4PACz and fragment 3 of 2PACz-K. For Me-4PACz, charge transfer (CT) excitation and local excitation (LE) is 6.276 % and 93.724 %. For 2PACz-K, charge transfer excitation and local excitation is 39.460 % and 60.540 %. In all, Me-4PACz shows more overlapped electron and hole than 2PACz-K.

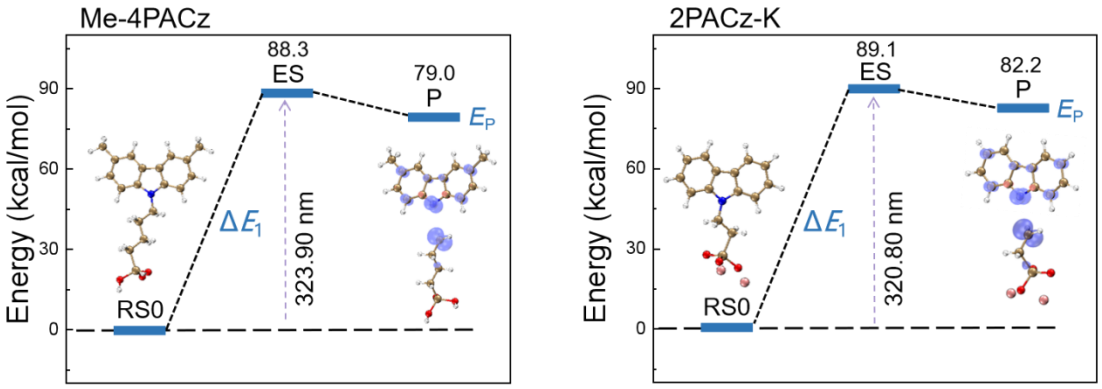

Supplementary Figure 77. Energy change of photo-decomposition reaction of Me-4PACz and 2PACz-K. RS0 refers to the reactant in the ground state. ES is short for the crucial excited state. P refers to decomposition products (i.e., two neutral radicals). The distribution of single electron in radicals is shown by purple isosurfaces.

Notes: The mechanism of photo-decomposition reaction[15]: (i) The ground-state SAM molecule (RS0) absorbs ultraviolet light and undergoes the vertical excitation to excited state (ES). (ii) The molecule undergoes the vibrational relaxation to reach the vibrational ground state of the transition state and cleaves the C-N bond to yield decomposition products (P).

Compared with Me-4PACz, 2PACz-K exhibits larger ΔE_1 and higher E_P. Combining with the low oscillator strength, these indicate 2PACz-K is more difficult to be excited under UV light, and the radical products are harder to form, synergistically enhancing the resistance to UV degradation.

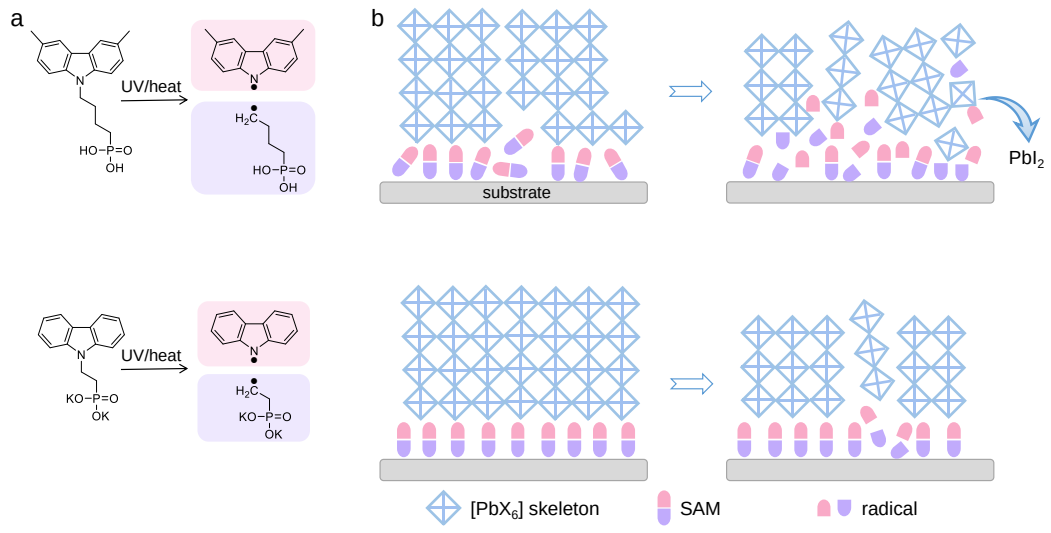

Supplementary Figure 78. Proposed mechanism of (a) SAM decomposition and (b) perovskite degradation under UV or heat.

Notes: The schematic diagram shows the serious buried degradation at the Me-4PACz/perovskite interface. While the 2PACz-K/perovskite interface remains relatively stable with less diffusion of radicals.

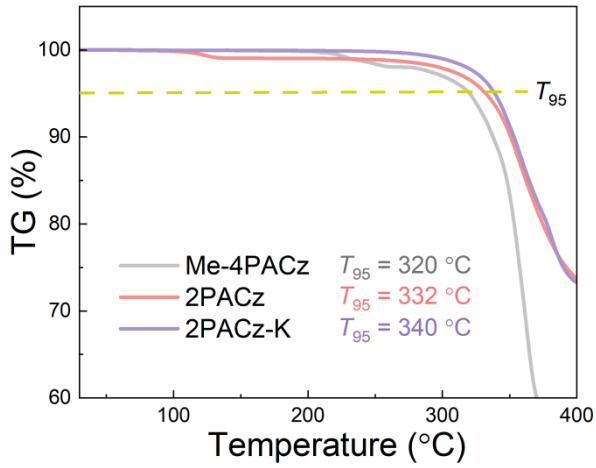

Supplementary Figure 79. Thermogravimetry (TG) curves of Me-4PACz, 2PACz and 2PACz-K. 2PACz-K exhibits better thermal stability than 2PACz, indicating the effect of salt.

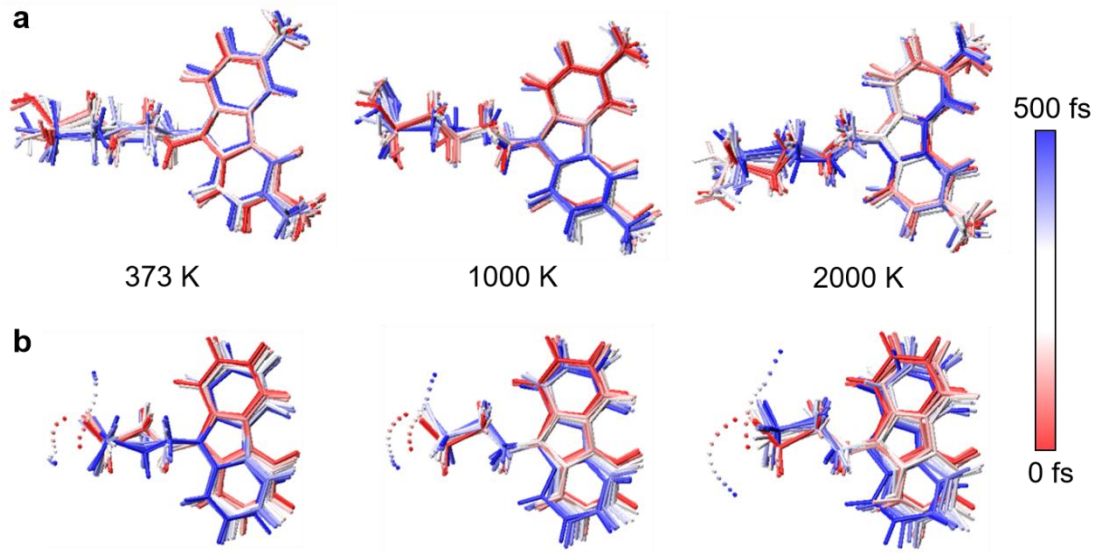

Supplementary Figure 80. Structure variation of (a) Me-4PACz and (b) 2PACz-K during the 500 fs trajectories at 373, 1000 and 2000 K based on *ab-initio* molecular dynamics, extracted every 50 fs from the trajectories. The full trajectories at 373 K are attached in Supplementary Movie 3-4.

Notes: Isomerization and dissociation are not observed during the 500 fs simulation for Me-4PACz and 2PACz-K. The higher the simulation temperature, the larger the geometry fluctuation.

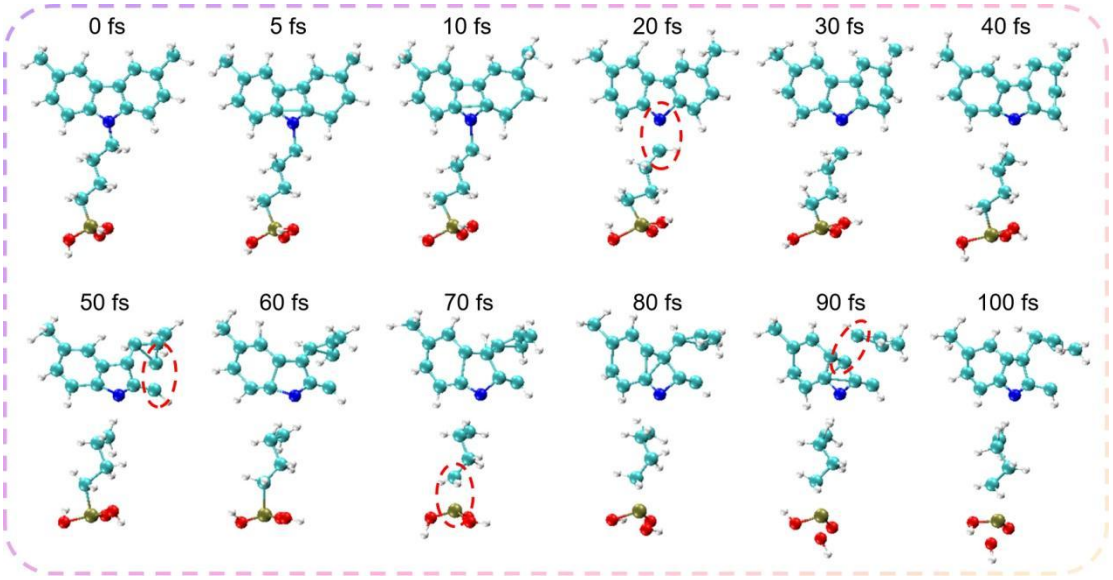

Supplementary Figure 81. The *ab-initio* molecular dynamics trajectories simulated at 5000 K for Me-4PACz. The full trajectory is attached in Supplementary Movie 5.

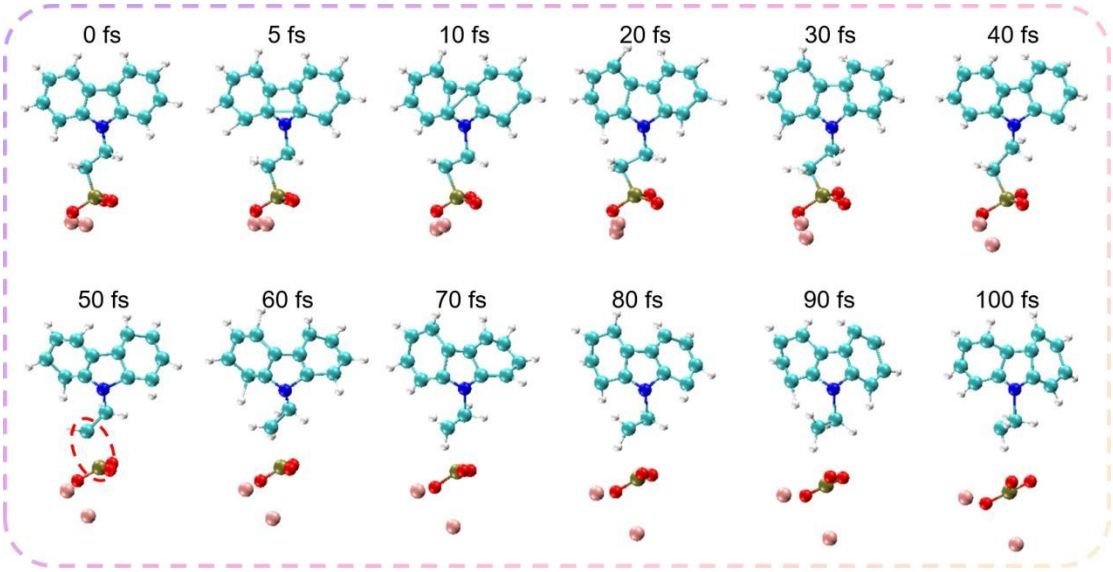

Supplementary Figure 82. The *ab-initio* molecular dynamics trajectories simulated at 5000 K for 2PACz-K. The full trajectory is attached in Supplementary Movie 6.
Notes: During the 100 fs simulation, the C-N and C-P bonds in Me-4PACz dissociate at around 20 fs and 70 fs, respectively. The carbazole ring in Me-4PACz shows cleavage at 50 fs. For 2PACz-K, the C-P bond dissociates at 50 fs while C-N bond and the carbazole ring display no obvious cleavage after 100 fs. The results indicate better thermal stability of 2PACz-K than Me-4PACz.

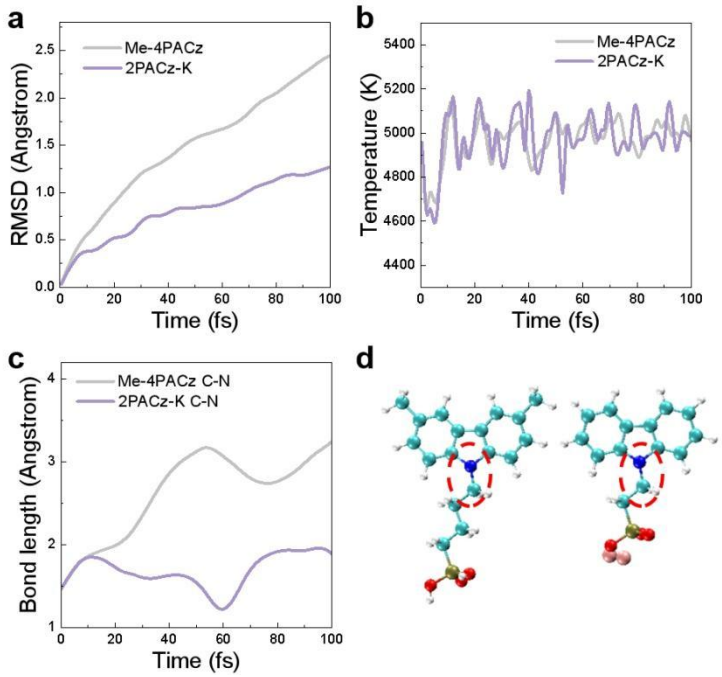

Supplementary Figure 83. (a) Root mean square deviation (RMSD), (b) temperature variation and (c) C-N bond length of *ab-initio* molecular dynamics trajectories simulated at 5000 K of Me-4PACz and 2PACz-K. (d) The structures of Me-4PACz and 2PACz-K. The C-N bonds are marked by red circles.

Notes: The temperature fluctuates around 5000 K under Berendsen thermostat. Me-4PACz displays larger RMSD and longer C-N bond length than 2PACz-K, suggesting serious cleavage under thermal stress.

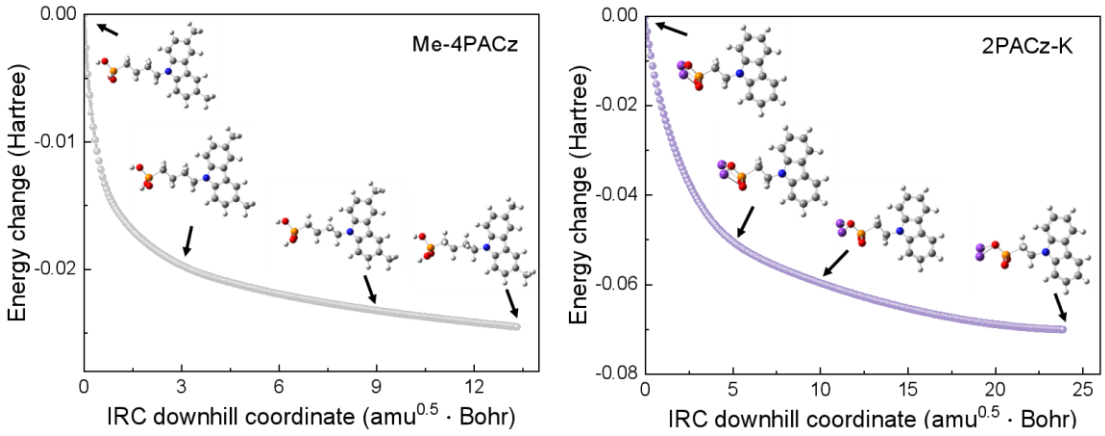

Supplementary Figure 84. Intrinsic reaction coordinate (IRC) curve and geometry change of Me-4PACz and 2PACz-K in the relaxation process under the electric field of -0.01 a.u. Here, amu refers to atomic mass unit.

Notes: The downhill trajectory was generated via downhill option in IRC keyword of Gaussian software[16]. The trajectory continues to generate until the current geometry is very close to the minimum on the potential energy surface. The full trajectories are attached in Supplementary Movie 7-8.

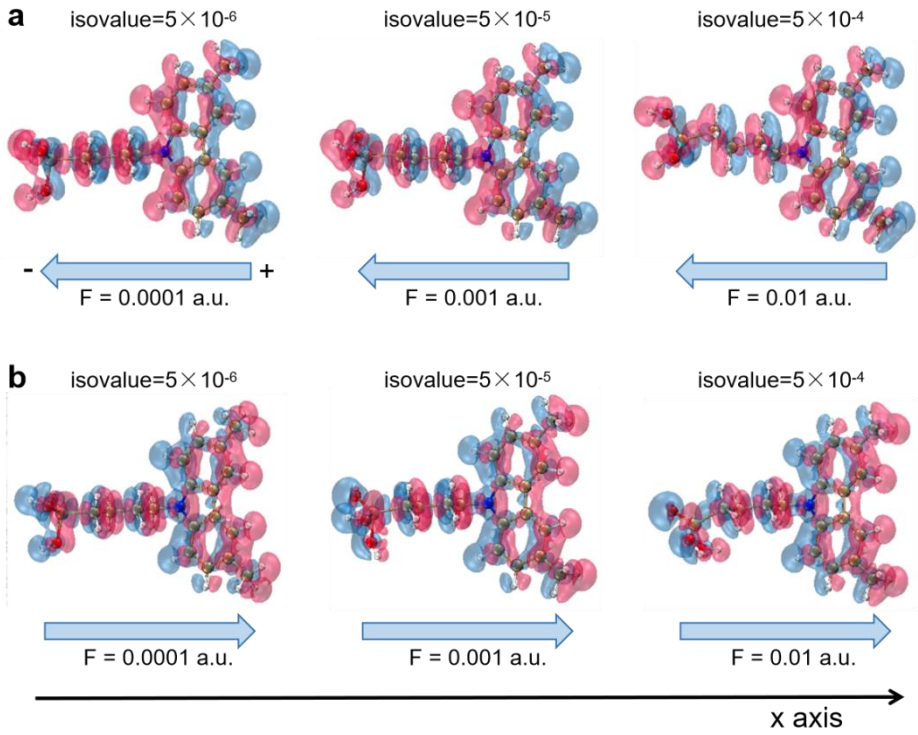

Supplementary Figure 85. Isosurface maps of electron density difference ($\Delta\rho$) before and after applying different external electric field (EEF) for Me-4PACz, under electric field in the (a) opposite or (b) same direction of x-axis. Blue and red correspond to positive and negative parts, respectively. For EEF, 0.01 a.u. = 5.1 $\times 10^9$ V/m.

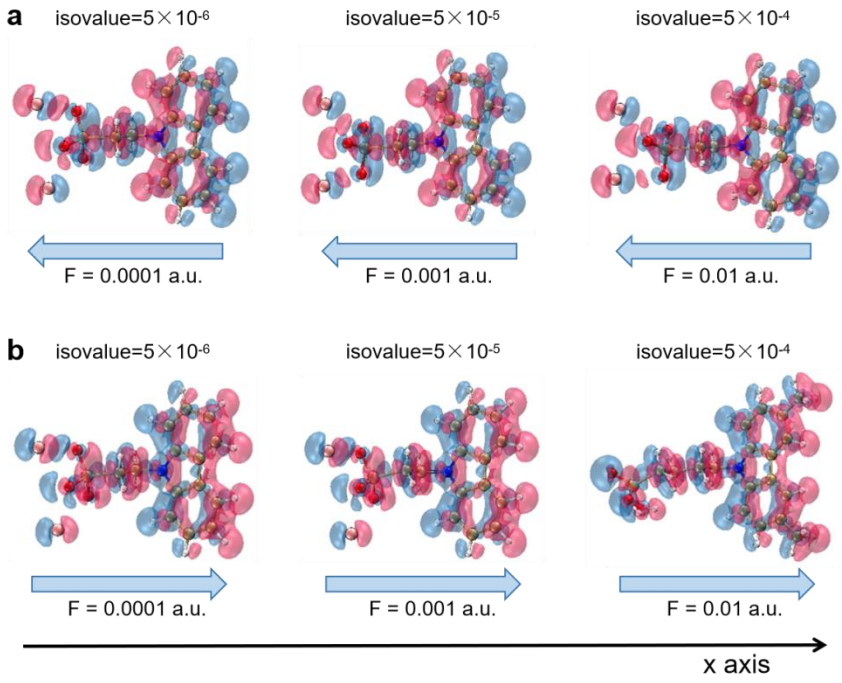

Supplementary Figure 86. Isosurface maps of electron density difference before and

after applying different external electric field for 2PACz-K, under electric field in the (a) opposite or (b) same direction of x-axis. Blue and red correspond to positive and negative parts, respectively.

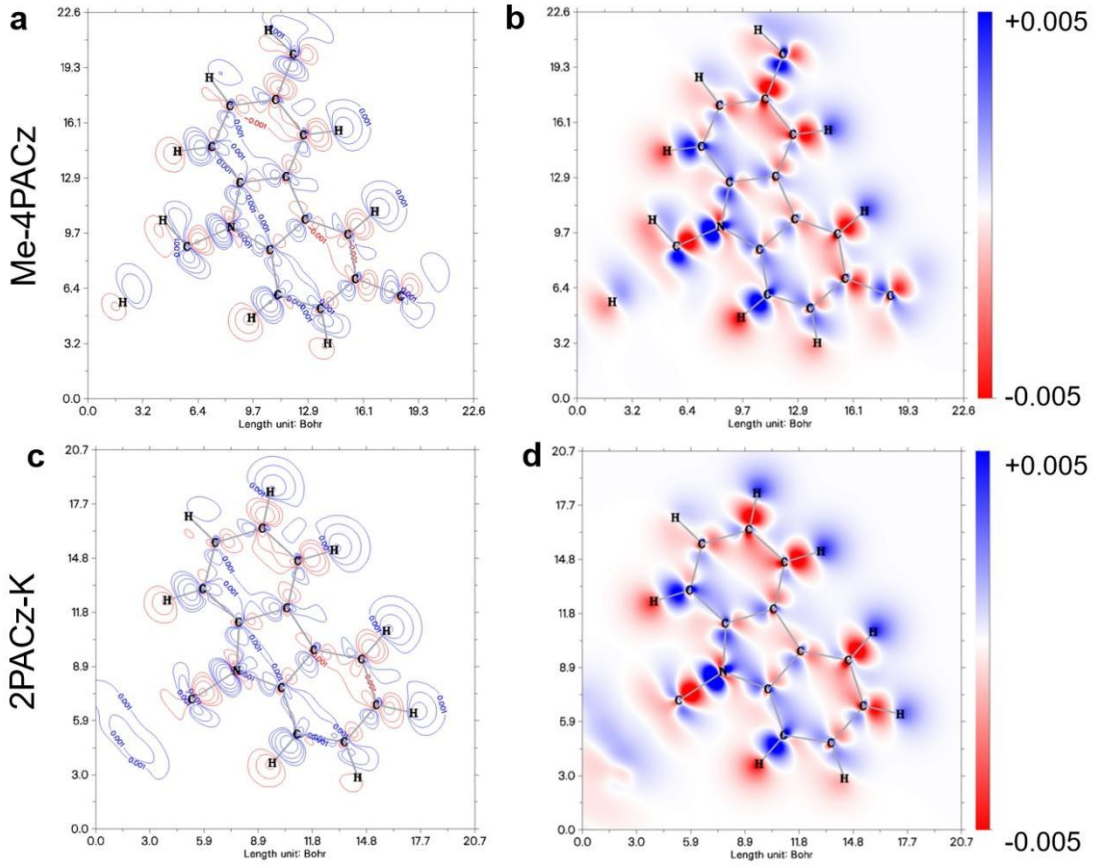

Supplementary Figure 87. (a,c) Color-filled maps and (b,d) contour line maps of electron density difference of the carbazole ring before and after applying -0.01 a.u. external electric field for Me-4PACz and 2PACz-K. Blue and red correspond to positive and negative parts, respectively.

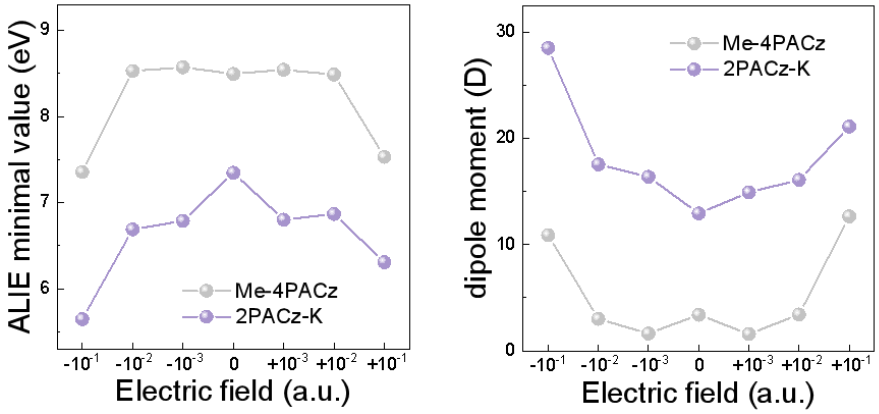

Supplementary Figure 88. ALIE minima and dipole moment values of Me-4PACz and 2PACz-K under different external electric field. The electric field in the same (or

opposite) direction as the x-axis is defined as positive (or negative).

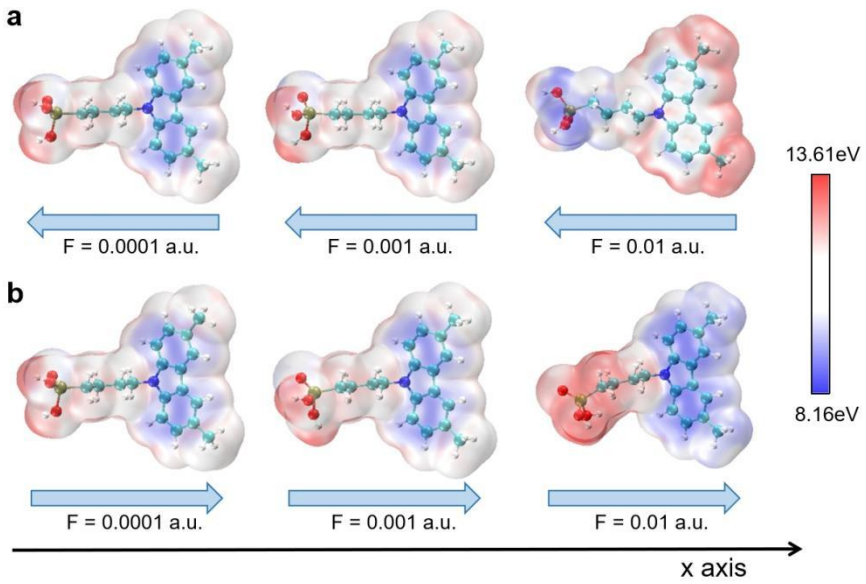

Supplementary Figure 89. ALIE maps of Me-4PACz after applying different external electric field, under electric field in the (a) opposite or (b) same direction of x-axis.

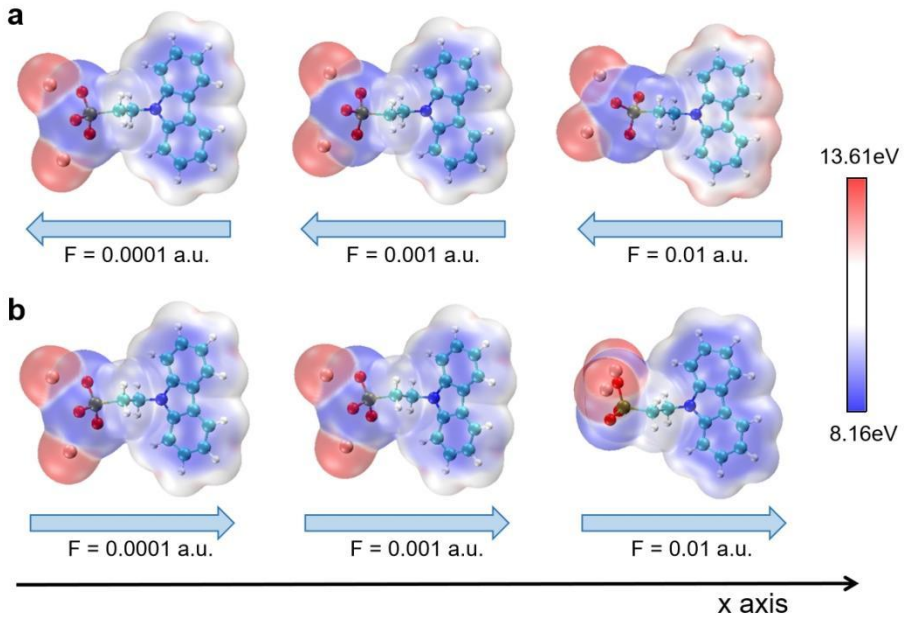

Supplementary Figure 90. ALIE maps of 2PACz-K after applying different external electric field, under electric field in the (a) opposite or (b) same direction of x-axis.

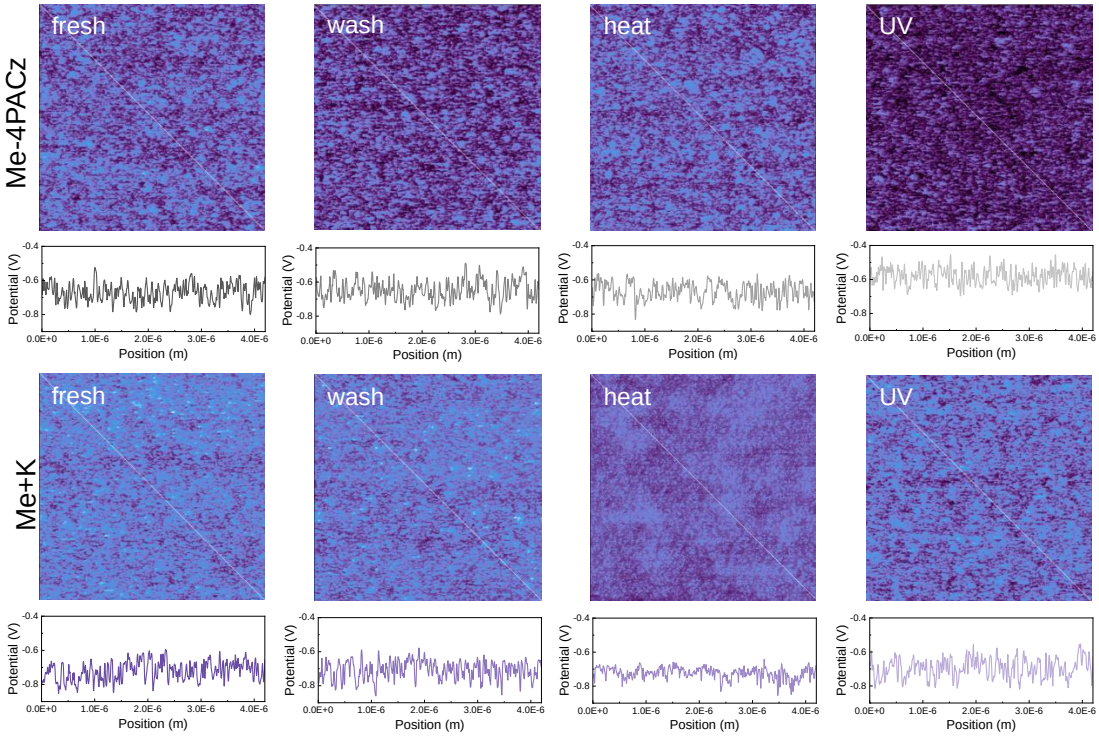

Supplementary Figure 91. KPFM images and corresponding lines of fresh ITO/NiO_x/SAM films, and those after DMF washing (50 μL DMF, spin-coating at 3000 rpm for 30 s), heating (85 ℃ for 24 h in nitrogen) and UV aging (365 nm, ~1 W cm^{-2} for 24 h in air), based on Me-4PACz and Me-4PACz+2PACz-K. The area is 3 μm × 3 μm.

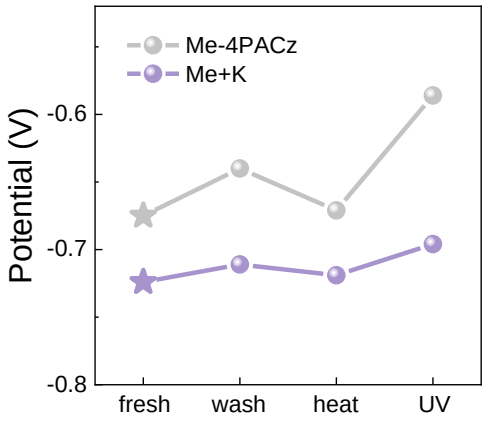

Supplementary Figure 92. The potential change of fresh and aged ITO/NiO_x/SAM films, corresponding to Figure 5e.

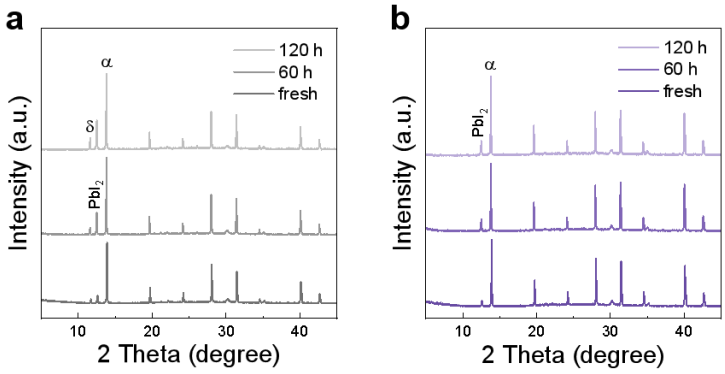

Supplementary Figure 93. XRD patterns of perovskite on (a) Me-4PACz and (b) Me-4PACz+2PACz-K under an ambient environment with 40 ± 5% RH at 20-25 ℃.

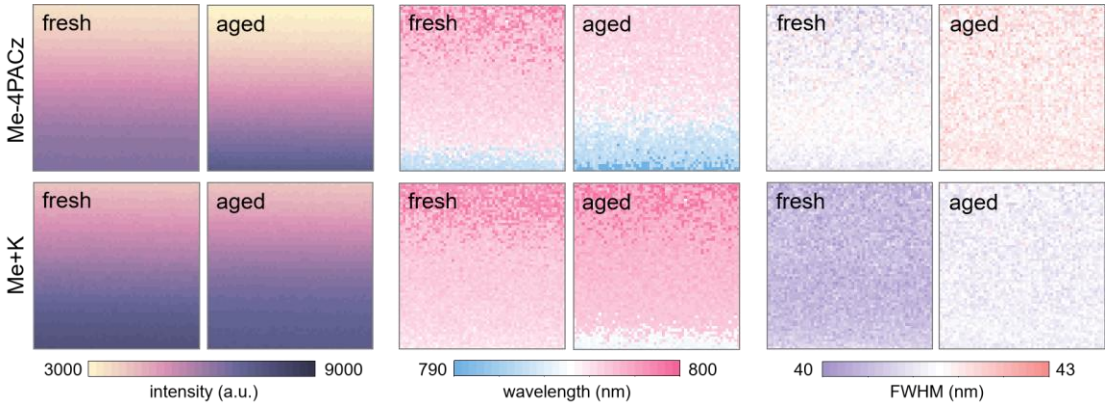

Supplementary Figure 94. PL mapping of fresh (left) and aged (right) perovskite films based on Me-4PACz and Me-4PACz+2PACz-K, including PL intensity, wavelength and FWHM, respectively. Data were obtained over an area of 43 μm × 43 μm. The samples are aged under a 20 mW laser for 10 min in air (at 25 ℃, relative humidity 20%).

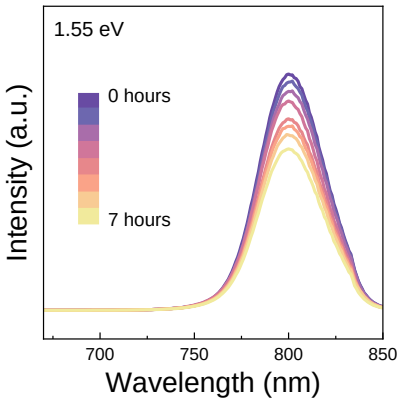

Supplementary Figure 95. PL evolution of 1.55 eV perovskite film on ITO/NiO_x/Me-4PACz+2PACz-K, aged under 100 mW cm^{-2} LED light in ambient air. No new PL peaks are observed, indicating no phase separation. Concretely, the separation of Cs-rich and FA-rich phases is not observed.

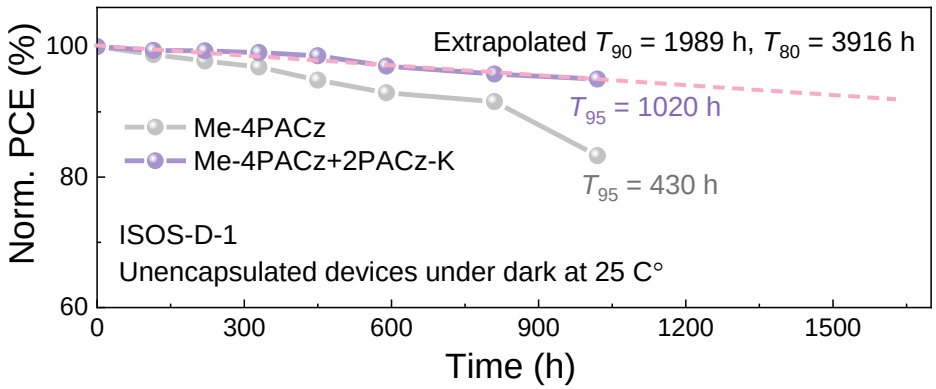

Supplementary Figure 96. ISOS-D-1 stability protocol of the unencapsulated 1.55 eV devices under dark storage at room temperature in nitrogen.

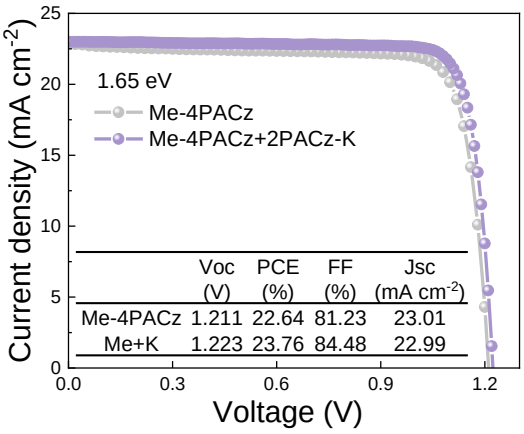

Supplementary Figure 97. *J-V* characteristics of the champion 1.65 eV devices under reverse scan.

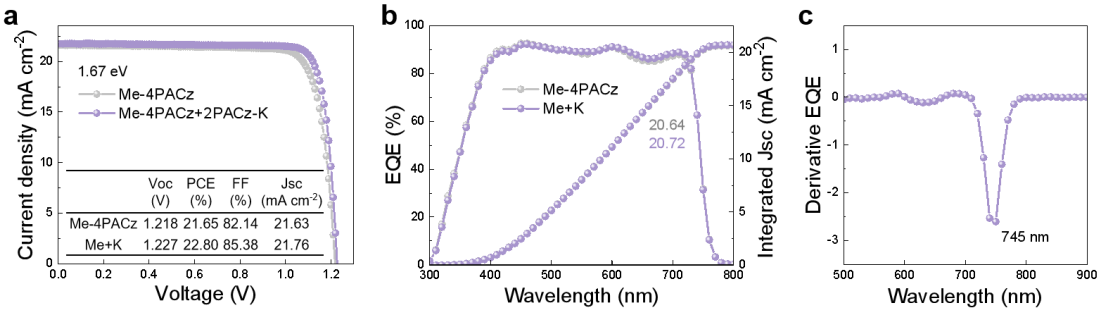

Supplementary Figure 98. Performance of 1.67 eV devices based on Me-4PACz and Me-4PACz+2PACz-K. (a) *J-V* characteristics of the champion 1.67 eV devices under reverse scan. (b) EQE spectra of champion devices. (c) Derivative EQE spectrum.

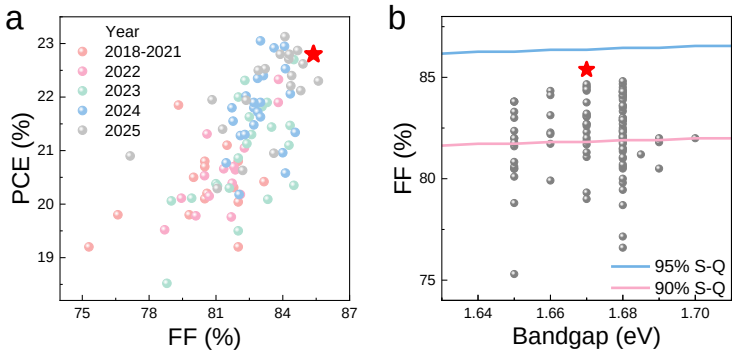

Supplementary Figure 99. Records of wide bandgap PSCs of 1.65-1.70 eV. (a) PCE and FF. (b) FF and the comparison of Shockley-Queisser (S-Q) limit[17]. In this work, the 1.67 eV device achieved a FF of 85.38%, up to 98.9% of S-Q limit.

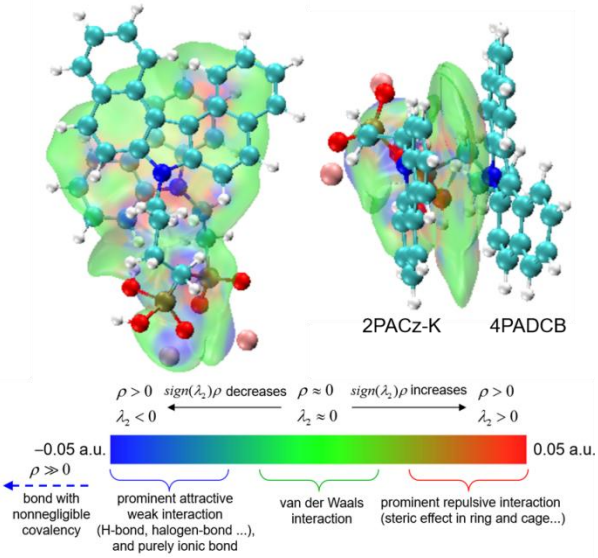

Supplementary Figure 100. Front and top view of IGM maps of δg^{inter} with isosurface of 0.001 a.u. for 4PADCB and 2PACz-K.

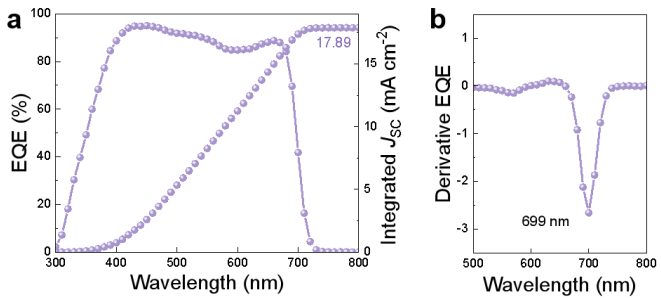

Supplementary Figure 101. (a) EQE and (b) derivative EQE spectra of 1.78 eV target devices.

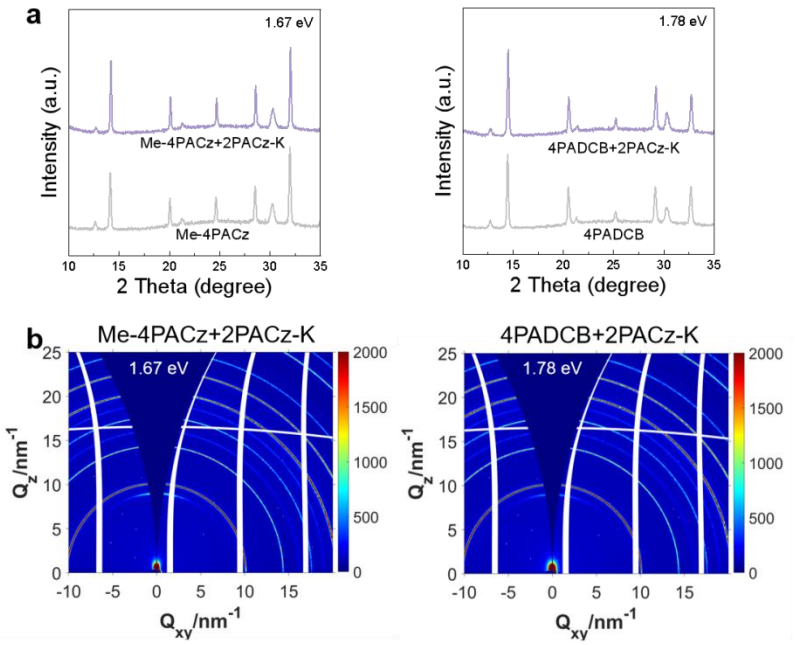

Supplementary Figure 102. (a) XRD patterns and (b) GIWAXS two-dimensional maps of 1.67 and 1.78 eV perovskite films.

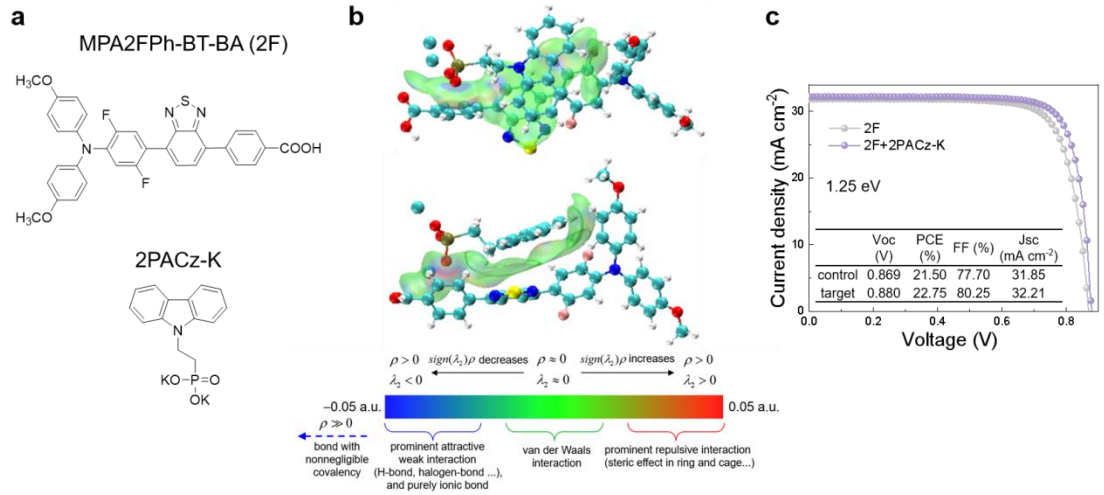

Supplementary Figure 103. (a) Chemical structure of 2F and 2PACz-K. (b) Front and side view of IGM maps of δg^{inter} with isosurface of 0.002 a.u. for 2F and 2PACz-K. (c) *J-V* characteristics of the champion 1.25 eV devices under reverse scan, based on 2F (control) and 2F+2PACz-K (target).

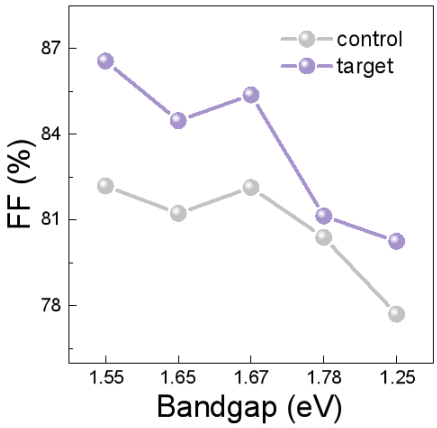

Supplementary Figure 104. Comparison of FF for devices of different bandgap.

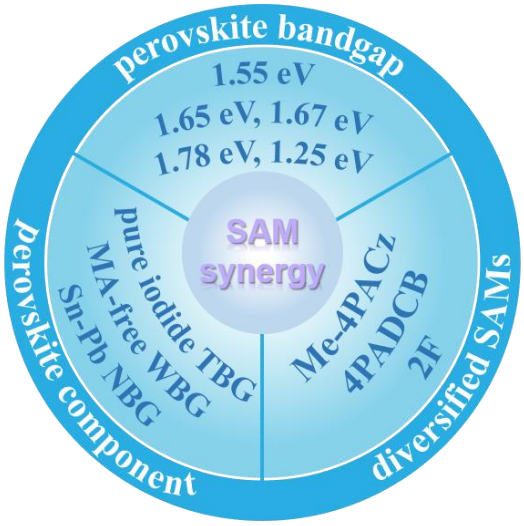

Supplementary Figure 105. The universality of SAM synergy strategy.

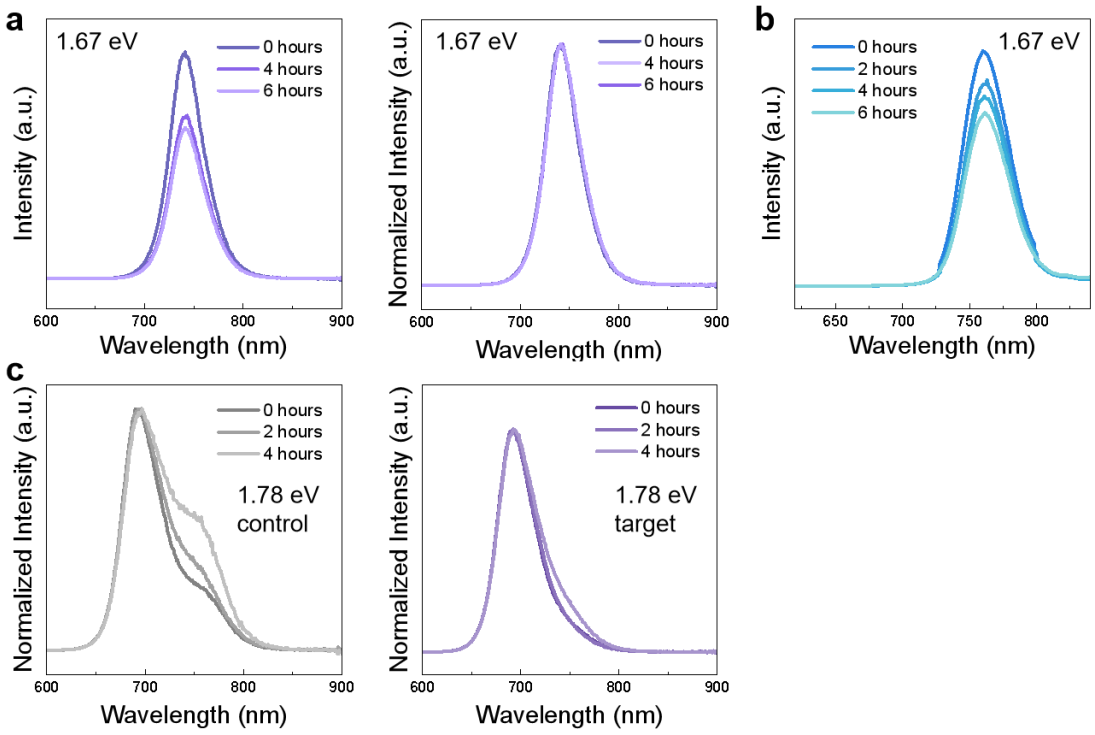

Supplementary Figure 106. PL evolution of aged wide bandgap perovskite films. (a) 1.67 eV perovskite films based on ITO/NiO_x/Me-4PACz+2PACz-K, aged under 100 mW cm^{-2} LED light in ambient air. (b) 1.67 eV perovskite films based on ITO/NiO_x/Me-4PACz+2PACz-K, aged at 85 °C in ambient air. (c) 1.78 eV perovskite films based on ITO/NiO_x/4PADCB (control) and ITO/NiO_x/4PADCB+2PACz-K (target), aged under 100 mW cm^{-2} LED light in ambient air. The PL intensity is normalized corresponding to Fig. 6d,e.

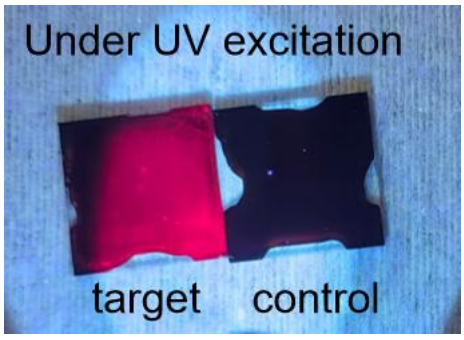

Supplementary Figure 107. The photos of 1.78 eV perovskite films under UV excitation. The structure is ITO/NiO_x/SAM/perovskite. The perovskite on 4PADCB+2PACz-K (target) exhibits bright red fluorescence at room temperature, indicating relatively few defects and optimized bottom interface.

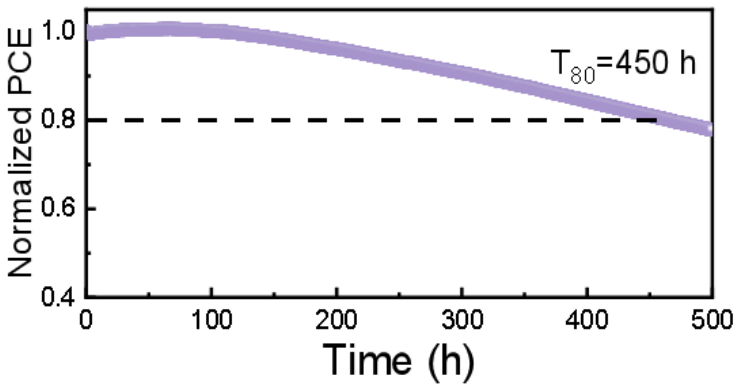

Supplementary Figure 108. The stability of the target tandem device, following ISOS-L-1 stability protocol under MPP tracking conditions under 1-sun equivalent illumination at 25 ℃ in nitrogen.

Supplementary Table

Supplementary Table 1. Summary of typical bandgap (1.5-1.6 eV) inverted perovskite solar cells based on SAMs[4]. HTL refers to hole transporting layer.

HTL	PCE (%)	V_{OC} (V)	FF (%)	V_{OC} × FF	Year
NiO_x/Br-BA	18.4	1.11	76.3	0.847	2017
V1036+C4	17.8	1.09	76.5	0.834	2018
MC-43	17.3	1.08	80	0.864	2019
2PACz	21.1	1.12	80.6	0.903	2019
TPA-PT-C6+CA-Br	17.49	/	/	/	2020
NiO_x/MeO-2PACz	19.9	1.115	80.2	0.894	2021
TPT-P6	21.43	1.125	81.08	0.912	2021
RC24	19.8	1.123	79	0.887	2022
PTAA/2PACz	22.17	1.15	82.75	0.952	2022
DC-PA+IAHA	23.59	1.16	82.45	0.956	2022
MPA-BT-CA	21.24	1.13	84.8	0.958	2020
MPA-BT-CA	21.81	1.15	82	0.943	2022
MPA-Ph-CA	22.53	1.139	84.02	0.957	2022
NiO_x/CBSA	21.8	1.11	81.43	0.904	2022
Br-2EPT	22.44	1.09	82	0.894	2022
Br-2EPSe	22.73	1.12	82.86	0.928	2022
PPA	23.24	1.14	82	0.935	2023
CbzNaph	24.1	1.17	83.39	0.976	2022
CbzNaph	24.98	1.173	85.06	0.998	2023
Me-4PACz	24.5	1.19	83.1	0.989	2023
MTPA-BA	22.62	1.14	85.2	0.971	2023
SAM1	18.86	1.109	78.3	0.868	2023
NiO_x/LS2+PTAA-0.2P	24.5	1.18	82.9	0.978	2023
BCB-C4PA	22.2	1.13	80	0.904	2023
MeO-2PACz	23.1	1.07	77	0.824	2023
NiO_x/2PACz+ethanolamine	21.99	1.19	80.2	0.954	2023
Me-4PACz+PFN-Br	20.67	1.16	79.12	0.918	2023
AC-5	23.19	1.13	84.05	0.950	2023
NiO_x/Me-4PACz+PC	25.09	1.175	82.54	0.970	2024
MPA-CPA	25.4	1.21	84.7	1.025	2023
PTZ-CPA	25.35	1.18	83.98	0.991	2024
Al_2O_3-NPs/Ph-4PACz	25.6	1.207	84.23	1.017	2024
TDPA-Cl	22.4	1.151	81.4	0.937	2024
MeO-BTBT	24.53	1.16	85.28	0.989	2024
NiO_x/MeO-2PACz	21.7	1.08	83.9	0.906	2024
NiO_x/HC-A4	20	1.05	81.8	0.859	2024
Cbz2SMe	24.42	1.172	82.82	0.971	2024

CbzBT	24.04	1.161	84.41	0.980	2024
NiO_x/MeO-4PADBC	25.6	1.19	84.6	1.007	2023
Me-4PACz/Al_2O_3	25.56	1.208	84.37	1.019	2023
NiO_x/Me-4PACz	25.2	1.1834	81.2	0.961	2023
Poly-4PACz	24.4	1.17	83.9	0.982	2023
2PACz+3-MPA	24.78	1.15	84.5	0.972	2023
DC-TMPS	24.8	1.18	84.1	0.992	2024
3PATAT-C3	23	1.13	83	0.938	2023
EtCz3EPA/PTAA:BCP	23.77	1.15	83	0.955	2024
A-4PADCB	25.05	1.186	83.14	0.986	2024
2PACz/PyCA-3F	25.12	1.17	86	1.006	2024
IDCz-3	25.15	1.16	84.74	0.983	2024
Me-4PACz/Br-EPA	25.16	1.2	83.54	1.002	2024
KF	25.17	1.189	83.6	0.994	2024
4PA-Spiro	25.28	1.16	84.2	0.977	2024
I-2PACz	25.39	1.163	85.8	0.998	2024
GM-4PACz	25.52	1.21	82.75	1.001	2024
NiO_x/Me-4PACz+DCZ-4P	25.57	1.173	85.1	0.998	2024
NiO_x/Me-4PACz/p-XPA	25.87	1.185	84.15	0.997	2024
DMAcPA	25.86	1.187	84.73	1.006	2023
CbzNaphPPA	26.07	1.191	86.45	1.030	2024
Py3	26.1	1.18	85.1	1.004	2024
Me-4PACz	26.15	1.178	86.47	1.019	2024
Me-PhpPACz	26.17	1.189	86.79	1.032	2024
NiO_x/Br-4PACz+Me-4PACz	26.28	1.187	85.8	1.018	2024
NiO_x/Me-4PACz+NA	26.69	1.201	84.5	1.015	2024
NiO_x/LS2	26.7	1.22	84.6	1.032	2024
NiO_x/Me-4PACz	26.81	1.194	85.76	1.024	2024
this work	26.88	1.177	86.57	1.019	2025

Supplementary Table 2. Average values of V_{OC}, J_{SC}, FF and PCE in Figure 4e for 1.55 eV devices.

	V_{OC} (V)	PCE (%)	FF (%)	J_{SC} (mA cm^{-2})
Me-4PACz	1.156	24.74	81.81	26.15
Me+K	1.176	26.67	86.07	26.33

Supplementary Table 3. Performance summary of perovskite modules corresponding to Figure 4h. AP refers to aperture area, and AC refers to active area.

structure	AP (cm^2)	AC (cm^2)	PCE (%)	V_{OC} (V)	J_{SC} (mA cm^{-2})	FF (%)	Year	DOI
nip	22.4	18.2	16.4	7.51	2.95	74	2020	10.1038/s41560-020-0653-2
nip	25.49		17.88	7.52	3.03	78.59	2020	10.1016/j.joule.2020.04.013
pin		20.77	16.63	1.0845	20.63	74.3	2021	10.1126/sciadv.abg3749
nip	12.92		16.88	4.11	5.53	74.27	2021	10.1002/pssr.202000613.
pin		25	16.12	6.36	3.62	70	2021	10.1002/aenm.202101291
pin	29.5		18.6	8.715	2.83	75.41	2021	10.1038/s41560-021-00831-8
pin	44.4		18	12.91	1.83	76.2	2021	10.1038/s41560-021-00831-8
nip		65	19.54	15.35	1.67	76.1	2021	10.1126/science.abh1035
pin	4		18	5.5	4	81	2021	10.1002/pip.3489
pin	51.1		16.6	19	1.1	82	2021	10.1002/pip.3489
pin	18.1		19.25	5.809	4.25	78	2021	10.1126/science.abi6323
pin	50		19.15	16.07	1.53	78	2021	10.1126/science.abi6323
nip		17.1	20.46	6.851	3.89	76.8	2021	10.1126/science.abh1035
nip		10	20.51	6.703	3.87	79.1	2021	10.1126/science.abh1035
nip		15	20.99	5.79	4.54	79.91	2021	10.1016/j.joule.2021.08.005
nip	31	29.25	19.51	11.68	2.26	73.85	2021	10.1016/j.joule.2021.08.005
nip		26	21.36	10.3	2.71	76.4	2021	10.1038/s41467-021-26754-2
nip	205		15.3	20.9	1.01	72	2022	10.1038/s41560-022-01039-0
nip		48	17.79	16.62	1.47	74.65	2022	10.1002/aenm.202103420
nip		2.25	18.71	3.32	7.43	75.83	2022	10.1002/aenm.202103420
nip	33.2	30.24	20.17	8.92	2.82	80.2	2022	10.1016/j.joule.2022.05.012
nip	22.4		20.5	8.13	3.16	80	2022	10.1038/s41560-022-01039-0
nip		14	20.61	11.08	2.36	78.82	2022	10.1038/s41467-022-32047-z
nip		20	21.66	12.15	2.29	77.9	2022	10.1126/science.abh1885
nip		64	20.55	18.43	1.46	76.59	2022	10.1126/science.abh1885
pin	12.84		21.07	7.2	3.65	80.22	2022	10.1002/aenm.202202287
nip	34.36	30.24	21.08	8.92	2.96	79.9	2022	10.1016/j.cej.2021.133713
nip		28	21.35	8.761	3.08	79.1	2022	10.1002/ange.202212891
nip		25	21.45	11.6	2.36	78.51	2022	10.1038/s41566-021-00931-7
nip	30.24		22.59	9.368	3.24	74.5	2022	10.1021/acsami.1c24757
pin	25.03		18.8	8.13	3.04	76	2023	10.1038/s41560-023-01254-3
pin	12.25		18.3	7.36	3.4	74	2023	10.1016/j.joule.2023.05.017
nip		18	22.27	8.96	3.12	79.65	2023	10.1016/j.joule.2023.05.020
nip		55	19.53	15.26	1.79	71.49	2023	10.1016/j.joule.2023.05.020
nip	17.1		19.6	6.99	3.81	73.8	2023	10.1126/science.add8786
pin	25		20.7	8.11	3.3	77.3	2023	10.1016/j.joule.2023.10.014
nip	10		18.8	6.87	3.55	76.9	2023	10.1039/d2ee01634f

nip	36		20.1	10.48	2.54	75.4	2023	10.1002/aenm.202300595
nip	27.83		21.38	7.483	3.06	74.22	2023	10.1038/s41586-023-06208-z
pin	26.9		21.78	9.41	2.88	80.32	2023	10.1126/science.ade9463
nip	12.25	11.52	20.23	6.726	3.74	80.5	2023	10.1038/s41893-023-01196-4
nip		61.6	20.46	15.82	1.666	77.6	2023	10.1038/s41893-023-01196-4
nip	81		20.15	15.46	1.71	76.3	2023	10.1002/aenm.202300595
nip		36.4	20.33	13.02	2.038	76.64	2023	10.1016/j.joule.2023.03.003
nip		30.24	21.71	8.887	3.02	80.9	2023	10.1002/adma.202300720
pin		10	22	4.68	6.11	76.9	2023	10.1126/science.adg3755
pin		12	18.4	5.43	4.42	77	2024	10.1016/j.joule.2024.02.007
pin	23.2		20	9.96	2.51	80	2024	10.1126/science.adn9453
pin	174		18.8	10.8	2.29	76	2024	10.1126/science.adn9453
pin	228		18.1	21.9	1.02	76	2024	10.1126/science.adn9453
pin	4	3.86	19.7	4.45	21.6	78.6	2024	10.1002/solr.202300862
pin	16	15.1	17	8.75	21.9	71.8	2024	10.1002/solr.202300862
pin	100		15.5	21.7	19.6	73	2024	10.1002/solr.202300862
nip	11.56	10.28	20.66	5.88	4.76	75.96	2024	10.1016/j.joule.2024.01.016
pin		61.48	19.22	12.04	2.01	79.35	2024	10.1021/acsami.4c05893
nip	24.5		21.15	11.82	2.24	80	2024	10.1002/aenm.202400791
nip		214.7	19.91	33.81	0.753	78.2	2024	10.1002/aenm.202400791
nip		18	20.76	8.91	3.05	76.4	2024	10.1038/s41467-024-52199-4
nip		18	20.08	8.83	2.96	76.82	2024	10.1039/D4TA01511H
nip		12.25	21.39	6.81	3.99	78.74	2024	10.1016/j.jechem.2024.01.063
nip		18	22.91	9.25	3.12	79.29	2024	10.1021/jacs.4c00110
nip	15.28		22.4	6.77	4.1	81.6	2024	10.1038/s41560-023-01444-z
nip	30.86		21.8	10.05	2.7	80	2024	10.1038/s41560-023-01444-z
nip	27.2		23.2	9.46	3.05	80.3	2024	10.1126/science.ado6619
nip	27.22		23.3	9.402	3.08	80.33	2024	10.1038/s41586-024-07228-z
pin		14.4	22.28	9.474	3.09	76.12	2024	10.1021/jacs.3c13576
nip	/	14	22.35				2024	10.1039/d4ee00229f
nip		14	22.96	11.5	2.429	82.19	2024	10.1021/jacs.4c03783
pin	22.96		23.69	10.566	2.656	84.4	2024	10.1002/smtd.202400428
pin	57.13		23.05	16.346	1.683	83.8	2024	10.1002/smtd.202400428
nip		12.1	22.4	6.935	4.11	78.71	2025	10.1021/acsenergylett.4c03233
nip		12	22.81	3.553	8.2	77.57	2025	10.1002/adma.202502916
nip		23.26	22.7	9.5	3.27	73.04	2025	10.1002/anie.202508169
nip	57.2		22.76	20.4	1.37	81.2	2025	10.1016/j.joule.2025.101919
nip	11.46		23.39	6.06	4.7	82.06	2025	10.1002/adma.202407225
pin		22.4	22.61	8.377	3.457	78.08	2025	10.1002/anie.202421174
pin		12.96	22.96	6.935	4.226	78.36	2025	10.1002/adma.202505087
pin		12.96	22.9	6.84	4.25	78.78	2025	10.1002/anie.202503008
pin	14.4		22.95	7.24	9.8	77.62	2025	10.1002/anie.202512660

pin	10.8		22.89	6.91	4.25	78.17	2025	10.1039/d5ee00156k
pin	26.78		22.3	9.05	3.1	79.5	2025	10.1002/adfm.202516987
pin		51	19.64	11.49	2.97	72.14	2025	10.1002/adma.202506291

Supplementary Table 4. Excitation energy, corresponding wavelength and oscillator strength (*f*) of the first 10 excited states of Me-4PACz and 2PACz-K based on time-dependent DFT (TD-DFT) calculation.

Excited State	Me-4PACz			2PACz-K		
	Excitation energy (eV)	Wavelength (nm)	*f*	Excitation energy (eV)	Wavelength (nm)	*f*
1	**3.8278**	**323.90**	**0.0328**	3.2683	379.36	0.0003
2	4.3692	283.77	0.0659	3.3930	365.41	0.0000
3	4.9682	249.56	0.5596	3.5042	353.81	0.0020
4	5.1602	240.27	0.0092	3.6685	337.97	0.0006
5	5.2337	236.89	0.1729	3.7570	330.01	0.0000
6	5.4618	227.00	0.0072	**3.8648**	**320.80**	**0.0502**
7	5.6395	219.85	0.2546	3.8776	319.75	0.0143
8	5.7609	215.22	0.4115	3.9331	315.23	0.0034
9	5.9574	208.12	0.0007	3.9871	310.96	0.0002
10	5.9922	206.91	0.0125	4.0900	303.14	0.0247

Supplementary Table 5. Summary of 1.65-1.70 eV inverted perovskite solar cells. E_g refers to bandgap.

Perovskite component	structure	E_g (eV)	V_{OC} (V)	J_{SC} (mA cm^{-2})	FF (%)	PCE (%)	Year	DOI
$Cs_{0.05}MA_{0.15}FA_{0.8}Pb(I_{0.75}Br_{0.25})_3$	nip	1.65	1.22	21.2	80.5	20.8	2018	10.1038/s41467-018-05531-8
$FA_{0.65}MA_{0.20}Cs_{0.15}Pb(I_{0.8}Br_{0.2})_3$	pin	1.68	1.17	21.2	79.8	19.8	2019	10.1016/j.joule.2019.04.012
$FA_{0.6}Cs_{0.3}DMA_{0.1}PbI_{2.4}Br_{0.6}$	pin	1.7	1.2	19.6	82	19.2	2019	10.1016/j.joule.2019.05.009
$FA_{0.78}Cs_{0.22}Pb(I_{0.85}Br_{0.15})_3$	pin	1.67	1.217	20.18	83.16	20.42	2020	10.1126/science.aaz5074
$FA_{0.65}MA_{0.20}Cs_{0.15}Pb(I_{0.8}Br_{0.2})_3$	nip	1.68	1.196	21.65	81.5	21.1	2020	10.1002/solr.202000082
$FA_{0.65}MA_{0.20}Cs_{0.15}Pb(I_{0.8}Br_{0.2})_3$	pin	1.68	1.213	21.2	80.5	20.7	2020	10.1126/science.aba3433
$Cs_{0.17}FA_{0.83}PbI_{2.3}Br_{0.7}$	nip	1.65	1.18	21.6	75.3	19.2	2020	10.1002/adfm.201909919
$Cs_{0.17}FA_{0.83}Pb(I_{0.83}Br_{0.17})_3$	pin	1.69	1.21	20.7	80.5	20.1	2020	10.1021/acsenergylett.0c01104
$Cs_{0.05}(FA_{0.77}MA_{0.23})_{0.95}Pb(I_{0.77}Br_{0.23})_3$	pin	1.68	1.22	20.7	82	20.8	2020	10.1126/science.abd4016
$Cs_{0.15}MA_{0.15}FA_{0.7}Pb(I_{0.8}Br_{0.2})_3$	pin	1.68	1.22	21	80	20.5	2021	10.1016/j.joule.2021.05.013
$Cs_{0.05}MA_{0.15}FA_{0.8}Pb(I_{0.85}Br_{0.15})_3$	pin	1.68	1.2	21.6	76.6	19.8	2021	10.1039/d1ee01206a
$CsFADMAPbI_3$	nip	1.65	1.127	21.69	82	20.04	2021	10.1021/acsenergylett.1c01013
$FA_{0.8}Cs_{0.2}Pb(I_{0.8}Br_{0.2})_3$	pin	1.68	1.19	20.94	81.8	20.31	2021	10.1016/j.nanoen.2021.106608
$FAMACsPb(I_{0.8}Br_{0.2})_3$	nip	1.67	1.195	23.06	79.32	21.85	2021	10.1126/sciadv.abj1799
$Cs_{0.05}FA_{0.8}MA_{0.15}Pb(I_{0.75}Br_{0.25})_3$	pin	1.68	1.218	20.6	80.6	20.2	2021	10.1016/j.joule.2021.11.003
$Cs_{0.2}FA_{0.8}Pb(I_{0.82}Br_{0.15}Cl_{0.03})_3$	pin	1.66	1.23	20.79	82.28	21.05	2022	10.1002/adfm.202107359
$Cs_{0.22}FA_{0.78}PbI_{2.55}Br_{0.45}$	pin	1.68	1.204	20.72	81.73	20.39	2022	10.1002/inf2.12307
$Rb_{0.05}Cs_{0.05}FA_{0.675}MA_{0.225}Pb(I_{0.75}Br_{0.25})_3$	pin	1.68	1.207	20.98	79.45	20.11	2022	10.1002/adfm.202200431
$Cs_{0.22}FA_{0.78}PbI_{2.55}Br_{0.45}$	pin	1.67	1.19	20.33	81.69	19.76	2022	10.1002/adma.202201451
$Cs_{0.22}FA_{0.78}Pb(I_{0.85}Br_{0.15})_3$	nip	1.65	1.21	21.08	80.49	20.53	2022	10.1002/adma.202201315
$Cs_{0.05}FA_{0.8}MA_{0.15}Pb(I_{0.755}Br_{0.255})_3$	pin	1.68	1.209	20.68	80.7	20.15	2022	10.1126/science.abn8910
$FA_{0.65}MA_{0.20}Cs_{0.15}Pb(I_{0.8}Br_{0.2})_3$	pin	1.67	1.195	21.11	81.87	20.64	2022	10.1021/acsnano.2c02876
$Cs_{0.1}FA_{0.2}MA_{0.7}Pb(I_{0.85}Br_{0.15})_3$	pin	1.65	1.23	21.2	83.8	21.9	2022	10.1038/s41566-022-01033-8
$Cs_{0.1}FA_{0.2}MA_{0.7}Pb(I_{0.80}Br_{0.20})_3$	pin	1.69	1.25	20.2	81.8	20.7	2022	10.1038/s41566-022-01033-8
$Cs_{0.05}MA_{0.15}FA_{0.8}Pb(I_{0.75}Br_{0.25})_3$	pin	1.68	1.25	20.32	81.35	20.66	2022	10.1021/acsami.2c10928
$Cs_{0.22}FA_{0.78}PbI_{2.55}Br_{0.45}$	pin	1.68	1.2	20.7	78.7	19.52	2022	10.1021/acsenergylett.2c01506
$Cs_{0.15}FA_{0.7}MA_{0.15}PbI_{2.4}Br_{0.6}$	pin	1.65	1.14	23.19	80.6	21.31	2022	10.1002/adma.202206193
$Cs_{0.1}FA_{0.9}PbI_{2.74}Br_{0.16}Cl_{0.1}$	pin	1.65	1.147	21.58	80.1	19.78	2022	10.1002/aenm.202202404
$Cs_{0.3}DMA_{0.2}MA_{0.5}PbI_3$	pin	1.68	1.21	20.3	82.1	20.18	2022	10.1016/j.joule.2022.08.006
$Cs_{0.25}FA_{0.75}Pb(I_{0.85}Br_{0.15})_3$	pin	1.65	1.2	22.15	83.81	22.33	2022	10.1016/j.joule.2022.10.007
$Cs_{0.15}FA_{0.8}MA_{0.05}PbI_{2.5}Br_{0.5}$	pin	1.65	1.22	21.5	83.3	21.9	2023	10.1002/aenm.202203230
$CsFAMAPbIBr$	pin	1.67	1.21	22.4	82.3	22.31	2023	10.1002/adfm.202214381
$Cs_{0.05}(FA_{0.77}MA_{0.23})_{0.95}Pb(I_{0.77}Br_{0.23})_3$	pin	1.68	1.239	21.16	82.5	21.63	2023	10.1002/ange.202216668
$FA_{0.8}Cs_{0.2}Pb(I_{0.8}Br_{0.2})_3$	pin	1.68	1.18	20.43	83.33	20.09	2023	10.1039/d2ta08966a
$FA_{0.5}Cs_{0.5}PbI_3$	nip	1.65	1.03	22.82	78.8	18.52	2023	10.1002/adfm.202300552

CsFAMAPbIBr	pin	1.65	1.19	20.9	81.6	20.3	2023	10.1002/adma.202207883
$FA_{0.75}Cs_{0.25}Pb(I_{0.8}Br_{0.2})_3$	pin	1.67	1.153	20.9	84.5	20.35	2023	10.1007/s40820-023-01078-6
$Cs_{0.17}FA_{0.83}PbI_{2.4}Br_{0.6}$	nip	1.67	1.255	20.31	79	20.06	2023	10.1002/smll.202208289
$FA_{0.75}Cs_{0.25}Pb(I_{0.8}Br_{0.2})_3$	pin	1.66	1.23	20.74	84.33	21.47	2023	10.1002/adfm.202300860
$Cs_{0.22}FA_{0.78}PbI_{2.55}Br_{0.45}$	pin	1.68	1.202	21.33	82.39	21.13	2023	10.1016/j.cej.2023.143341
$Cs_{0.05}MA_{0.15}FA_{0.8}Pb(I_{0.75}Br_{0.25})_3$	pin	1.68	1.2	20.94	81	20.38	2023	10.1002/smll.202302021
$Cs_{0.18}FA0._{82}Pb(I,Br)_3$	pin	1.69	1.22	19.5	82	19.5	2023	10.1126/science.adg0091
CsFAMAPbIBr	pin	1.67	1.14	21.64	81.07	20.34	2023	10.1002/adfm.202301695
$Cs_{0.2}FA_{0.8}Pb_{I2.4}Br_{0.6}$	pin	1.66	1.2	21.02	79.91	20.11	2023	10.1016/j.cej.2023.143860
$Cs_{0.05}(FA_{0.77}MA_{0.23})_{0.95}Pb(I_{0.77}Br_{0.23})_3$	pin	1.67	1.24	21.18	83.07	21.82	2023	10.1039/d3ta02209a
$Cs_{0.22}FA_{0.78}Pb(I_{0.85}Br_{0.15)3}$	nip	1.65	1.199	21.22	82	20.86	2023	10.1021/acsami.3c05333
$Cs_{0.05}FA_{0.8}MA_{0.15}Pb(I_{0.76}Br_{0.24})_3$	pin	1.68	1.25	21.5	84.5	22.7	2023	10.1126/science.ade9637
$Cs_{0.21}FA_{0.74}MA_{0.05}Pb(I_{0.83}Br_{0.12}Cl_{0.05})_3$	pin	1.68	1.185	21.66	83.5	21.44	2023	10.1002/adma.202305822
$Cs_{0.15}FA_{0.65}MA_{0.2}Pb(I_{0.8}Br_{0.2})_3$	pin	1.67	1.26	20.5	82.6	21.3	2023	10.1016/j.joule.2023.09.007
$Cs_{0.05}(FA_{0.84}MA_{0.16})_{0.95}Pb(I_{0.75}Br_{0.25})_3$	pin	1.67	1.272	21.09	82.01	22	2023	10.1002/aenm.202302983
$Cs_{0.05}FA_{0.8}MA_{0.15}PbI_{2.25}Br_{0.75}$	pin	1.68	1.215	20.59	84.28	21.1	2023	10.1002/anie.202315281
$Cs_{0.22}FA_{0.78}Pb(I_{0.85}Br_{0.15})_3$	pin	1.65	1.24	21.29	81.77	21.55	2024	10.1002/aenm.202303344
$FA_{0.75}Cs_{0.25}Pb(I_{0.8}Br_{0.2})_3$	pin	1.66	1.27	21.14	83.13	22.4	2024	10.1002/adma.202307987
$FA_{0.8}Cs_{0.2}Pb(I_{0.8}Br_{0.2})_3$	pin	1.68	1.248	20.77	82.1	21.28	2024	10.1002/solr.202301016
$Cs_{0.15}FA_{0.65}MA_{0.2}Pb(I_{0.8}Br_{0.2})_3$	nip	1.68	1.2	20.79	84	20.96	2024	10.1002/adfm.202311679
$Cs_{0.05}FA_{0.8}MA_{0.15}Pb(I_{0.75}Br_{0.25})_3$	pin	1.67	1.262	20.9	82.7	21.8	2024	10.1002/adma.202308370
$FA_{0.8}MA_{0.15}Cs_{0.05}Pb(I_{0.75}Br_{0.25})_3$	pin	1.68	1.22	21.84	82.35	22.02	2024	10.1002/solr.202300519
$Cs_{0.05}FA_{0.8}MA_{0.15}PbI_{2.25}Br_{0.75}$	pin	1.68	1.216	22.18	82.87	22.35	2024	10.1002/adma.202311923
$FA_{0.7}Cs_{0.25}MA_{0.05}Pb(I_{0.8}Br_{0.2})_3$	pin	1.67	1.25	21.05	84.34	22.06	2024	10.1002/adma.202400105
$FA_{0.8}Cs_{0.2}Pb(I_{0.8}Br_{0.2})_3$	pin	1.68	1.22	21.48	82.88	21.72	2024	10.1002/adma.202401103
$FA_{0.8}Cs_{0.15}MA_{0.05}PbI_{2.4}Br_{0.6}$	pin	1.65	1.256	21	83	21.9	2024	10.1039/d4ee00330f
$Cs_{0.3}DMA_{0.2}MA_{0.5}PbI_3$	pin	1.68	1.193	21.7	82.3	21.3	2024	10.1002/anie.202400205
$FA_{0.7}MA_{0.05}Cs_{0.25}Pb(I_{0.8}Br_{0.2})_3$	pin	1.68	1.243	20.9	82.7	21.48	2024	10.1016/j.cej.2024.151379
$FA_{0.8}Cs_{0.2}Pb(I_{0.8}Br_{0.2})_3$	pin	1.68	1.2	20.51	82.04	20.18	2024	10.1016/j.cej.2024.151459
CsFAMAPbIBr	pin	1.68	1.22	20.98	81.46	20.77	2024	10.1038/s41467-024-49351-5
$Cs_{0.15}FA_{0.65}MA_{0.2}Pb(I_{0.8}Br_{0.2})_3$	pin	1.67	1.24	21.3	82.7	21.9	2024	10.1002/aenm.202401029
$Cs_{0.05}FA_{0.8}MA_{0.15}Pb(I_{0.8}Br_{0.2)3}$	pin	1.66	1.181	22.59	81.72	21.8	2024	10.1002/anie.202407766
$Cs_{0.05}MA_{0.15}FA_{0.8}PbBr_{0.75}I_{2.25}$	pin	1.68	1.25	22.31	83	23.05	2024	10.1039/d4ee01547a
$Cs_{0.15}FA_{0.85}Pb(I_{0.77}Br_{0.23})_3$	pin	1.66	1.3	22.38	84.12	22.53	2024	10.1002/adma.202407681
$Cs_{0.235}FA_{0.765}Pb(I_{0.867}Br_{0.133})_3$	pin	1.68	1.23	20.8	84.12	20.58	2024	10.1038/s41467-024-51345-2
$Cs_{0.05}FA_{0.8}MA_{0.15}Pb(I_{0.755}Br_{0.255})_3$	pin	1.68	1.29	21.28	83.61	22.92	2024	10.1002/adma.202408686
$DMA_{0.1}Cs_{0.2}MA_{0.05}FA_{0.65}Pb(I_{0.9}Br_{0.1})_3$	pin	1.67	1.253	20.14	84.56	21.34	2024	10.1002/adfm.202410737
$Cs_{0.22}FA_{0.78}Pb(Br_{0.15}I_{0.85})_3$	nip	1.68	1.218	21.34	83	21.63	2024	10.1016/j.cej.2024.156798
/	pin	1.68	1.277	21.37	84.08	22.95	2024	10.1002/adma.202416150

$Cs_{0.05}FA_{0.8}MA_{0.15}Pb(I_{0.75}Br_{0.25})_3$	nip	1.68	1.195	20.94	81.06	20.29	2025	10.1002/aenm.202402856
$Rb_{0.05}(Cs_{0.3}FA_{0.7})_{0.95}Pb(I_{0.85}Br_{0.15})_3$	pin	1.65	1.18	23.01	80.83	21.95	2025	10.1016/j.cej.2024.158272
$Cs_{0.05}(FA_{0.77}MA_{0.23})_{0.95}Pb(I_{0.77}Br_{0.23})_3$	pin	1.68	1.254	20.8	85.6	22.3	2025	10.1007/s40820-024-01631-x
$Cs_{0.05}FA_{0.8}MA_{0.15}Pb(I_{0.75}Br_{0.25})_3$	pin	1.68	1.25	21.62	84.27	22.71	2025	10.1016/j.jechem.2024.12.067
$Cs_{0.05}FA_{0.8}MA_{0.15}Pb(I_{0.77}Br_{0.23})_3$	pin	1.67	1.25	21.2	84.4	22.4	2025	10.1016/j.cej.2025.159453
$Cs_{0.17}FA_{0.83}Pb(I_{0.83}Br_{0.17})_3$	pin	1.68	1.286	21.12	83.89	22.8	2025	10.1002/adfm.202419391
/	pin	1.68	1.24	21.76	84.67	22.87	2025	10.1038/s41467-024-55377-6
$FA_{0.74}Cs_{0.22}Rb_{0.04}Pb(I_{0.8}2Br_{0.15}Cl_{0.03})_3$	nip	1.67	1.29	20.4	81.3	21.4	2025	10.1126/science.adt3417
$FA_{0.5}Cs_{0.5}Pb(I_{0.93}Br_{0.07})_3$	nip	1.65	1.27	20.99	82.36	21.94	2025	10.1021/acsenergylett.4c03219
$Cs_{0.05}(FA_{0.77}MA_{0.23})_{0.95}Pb(I_{0.77}Br_{0.23})_3$	pin	1.68	1.2	20.9	83.6	20.95	2025	10.1002/aenm.202405675
$Cs_{0.15}FA_{0.85}PbI_{1.8}Br_{1.2}$	pin	1.68	1.217	21.88	84.91	22.62	2025	10.1021/acsnano.5c00458
CsFAMAPbIBr	pin	1.68	1.247	21.11	84.36	22.21	2025	10.1039/d5ee00563a
$Cs_{0.17}FA_{0.83}Pb(I_{0.80}Br_{0.20})_3$	pin	1.67	1.273	21.27	83.21	22.53	2025	10.1002/adma.202504520
$Cs_{0.22}FA_{0.78}Pb(I_{0.82}Br_{0.18})_3$	pin	1.68	1.26	21.6	82.9	22.5	2025	10.1002/anie.202424809
$Cs_{0.22}FA_{0.78}PbI_{2.55}Br_{0.45}$	pin	1.68	1.265	21.74	84.1	23.13	2025	10.1021/acsenergylett.5c00147
$Cs_{0.05}MA_{0.15}FA_{0.8}PbI_{2.25}Br_{0.75}$	pin	1.68	1.24	21.8	84.3	22.8	2025	10.1038/s41467-025-59896-8
$Cs_{0.05}FA_{0.8}MA_{0.15}PbI_{2.25}Br_{0.75}$	pin	1.68	1.226	22.09	77.15	20.9	2025	10.1039/D5EE02269J
$Cs_{0.22}FA_{0.78}Pb(I_{0.85}Br_{0.15})_3$	pin	1.68	1.23	21.29	84.81	22.12	2025	10.1002/adfm.202510444
$Cs_{0.05}(FA_{0.84}MA_{0.16})_{0.95}Pb(I_{0.75}Br_{0.25})_3$	pin	1.66	1.231	20.38	82.2	20.63	2025	10.1016/j.cej.2025.164850
$Cs_{0.2}FA_{0.8}Pb(I_{0.75}Br_{0.25})_3$	pin	1.68	1.253	20.63	82.95	21.45	2025	10.1002/smll.202504346

Supplementary Table 6. Performance summary of 2T all-perovskite tandem devices corresponding to Figure 6j. WBG refers to wide bandgap and NBG refers to narrow bandgap.

WBG PCE (%)	NBG PCE (%)	**Tandem PCE (%)**	Tandem V_{OC} (V)	Tandem J_{SC} (mA cm^{-2})	Tandem FF (%)	Year	DOI
/	20.4	**23.3**	1.943	15.11	79.3	2020	10.1038/s41560-020-00692-7
16.1	19.4	**23.7**	1.967	15	80.4	2020	10.1002/adma.201907058
16	20.2	**24.6**	2.03	15.2	79.7	2020	10.1038/s41560-020-0657-y
16.4	21.7	**25.6**	2.013	16	79.8	2020	10.1038/s41560-020-00705-5
15.8	16.7	**23.5**	1.9	15.4	80.4	2021	10.1002/solr.202100814
12.6	17.3	**20.1**	1.94	13.6	76.2	2022	10.1021/acsmaterialslett.2c01001
16	17.1	**23.1**	1.95	15.8	75	2022	10.1002/adma.202110053
/	19.4	**23.1**	2.01	14.8	77.5	2022	10.1038/s41560-022-01102-w
/	/	**23.5**	2.04	15.8	73	2022	10.1038/s41560-022-01059-w
15.1	18.2	**23.8**	2.1	15.1	75.1	2022	10.1002/aenm.202202438
/	19.6	**24.4**	2.03	15.4	78.1	2022	10.1126/sciadv.add0377
16.2	/	**24.7**	2	15.8	78.3	2022	10.1038/s41560-022-01045-2
18.58	21.51	**25.05**	1.956	15.41	83.1	2022	10.1038/s41560-022-01076-9
17.2	19	**25.1**	2.025	15.4	79.4	2022	10.1126/science.abn7696
17.1	22.2	**25.5**	2.121	15.03	80.1	2022	10.1038/s41560-022-01046-1
17.3	21.2	**25.6**	2.03	15.8	79.4	2022	10.1002/adma.202110351
17.7	20.7	**26.2**	2.046	16	80.1	2022	10.1002/adma.202110356
17.6	21	**26.3**	2.026	16.2	80.3	2022	10.1002/aenm.202202948
20.3	/	**27.1**	2.2	15.3	80.8	2022	10.1126/science.adf0194
17.7	23.2	**26.3**	2.05	16.2	79.3	2022	10.1002/adma.202205769
17.3	22.2	**26.7**	2.03	16.5	79.9	2022	10.1038/s41586-021-04372-8
20.2	21.5	**27.4**	2.19	15.05	83.1	2023	10.1038/s41586-022-05541-z
20.5	20.1	**21.5**	1.943	12.9	85.8	2023	10.1021/acsenergylett.2c02164
20.84	17.57	**23.65**	2.05	14.66	78.7	2023	10.1021/acsenergylett.2c02156
17.8	19.4	**24.1**	2.06	15.2	76.9	2023	10.1021/acsenergylett.3c00564
/	/	**24.2**				2023	10.1016/j.joule.2023.10.009
19.1	19.6	**25.3**	2.049	15.6	78.7	2023	10.1038/s41467-023-37492-y
16	22	**25.3**	2.04	15.1	82.1	2023	10.1002/aenm.202300968
18.5	21.7	**25.6**	2	16.1	79.6	2023	10.1038/s41560-023-01250-7
	22.16	**26.01**	2.08	15.77	79.35	2023	10.1002/adma.202301125
16.67	22.67	**26.08**	2.09	15.5	80.5	2023	10.1002/aenm.202301218
17.72	22.15	**26.16**	2.081	15.42	81.53	2023	10.1002/adma.202300352
20.22	21.97	**26.68**	2.115	15.29	82.5	2023	10.1039/d2ee04087e
18.28	21.26	**27.01**	2.11	15.37	83.13	2023	10.1038/s41586-023-05992-y
19.33	23.24	**27.22**	2.13	15.52	82.36	2023	10.1038/s41560-023-01274-z
19.83	21.83	**27.34**	2.15	15.81	80.49	2023	10.1039/d3ee02818f
19.38	22.46	**27.84**	2.11	16.02	82.2	2023	10.1038/s41586-023-06707-z
18.2	23.2	**28.1**	2.11	16.7	79.5	2023	10.1002/anie.202313374

19.6	21.3	**28.1**	2.135	16.2	81.5	2023	10.1038/s41467-023-43016-5
18.6	23.8	**28.5**	2.112	16.5	81.9	2023	10.1038/s41586-023-06278-z
/	21.28	**23.52**	1.98	14.54	81.8	2024	10.1016/j.cej.2023.147587
16.4	15.8	**23.8**	2.05	15.6	74.8	2024	10.1021/acsenergylett.3c02018
17.62	18	**24.66**	2.008	15.08	81.45	2024	10.1016/j.jechem.2023.09.023
/	23.2	**25.8**	2.11	15.15	80.8	2024	10.1002/adma.202411968
18.02	22.5	**26.03**	2.11	15.06	81.9	2024	10.1002/adma.202308240
20.06	21.73	**26.08**	2.12	15.43	79.72	2024	10.1002/adfm.202308908
19.7	22.1	**26.1**	2.02	15.8	81.8	2024	10.1002/adma.202307701
17.6	20.9	**26.1**	2.045	15.98	79.99	2024	10.1016/j.cej.2024.148638
19.6	21.2	**26.3**	2.1	15.8	79.5	2024	10.1038/s41560-024-01672-x
17.83	22.58	**26.33**	2.12	15.78	78.7	2024	10.1039/d3ee03898j
20.42	21.86	**26.54**	2.11	15.91	79.05	2024	10.1002/solr.202400184
20.24	21.16	**26.76**	2.109	15.38	82.5	2024	10.1002/solr.202301016
/	23.32	**26.76**	2.18	15.01	81.8	2024	10.1002/anie.202409072
17.9	21.4	**26.8**	2.15	15.5	80.2	2024	10.1126/science.adj6088
19.4	21.5	**27**	2.11	15.8	81	2024	10.1021/acsenergylett.4c00285
19.14	23.28	**27.03**	2.1	15.68	82	2024	10.1002/adma.202405860
19.22	21.01	**27.04**	2.021	16.46	81.30	2024	10.1002/aenm.202404366
19.9	/	**27.1**	2.14	15.98	79.3	2024	10.1016/j.jechem.2024.01.064
19.97	20.41	**27.11**	2.12	15.49	82.43	2024	10.1002/adma.202414790
/	22.04	**27.17**	2.13	15.59	81.23	2024	10.1002/adfm.202412458
18.8	23.4	**27.2**	2.16	15.6	81	2024	10.1038/s41467-024-48552-2
17.68	20.95	**27.2**	2.12	15.84	81.01	2024	10.1002/adfm.202410605
19	20.6	**27.2**	2.11	15.91	81.1	2024	10.1016/j.joule.2024.07.003
20.37	21.39	**27.23**	2.12	16.01	80.36	2024	10.1093/nsr/nwae055
19.59	21.65	**27.27**	2.113	15.85	81.4	2024	10.1038/s41560-023-01441-2
20	23	**27.3**	2.21	15.1	81.7	2024	10.1021/acsenergylett.3c02470
19.0	20.6	**27.4**	2.094	15.9	82.4	2024	10.1002/adma.202308706
19.96	22.14	**27.41**	2.133	15.58	82.6	2024	10.1002/aenm.202402171
20.20	21.66	**27.41**	2.14	15.53	82.28	2024	10.1039/d4ee02483d
18.69	23.09	**27.42**	2.11	15.64	83.08	2024	10.1039/d4ee01539h
19.3	/	**27.47**	2.13	15.59	82.73	2024	10.1002/aenm.202304429
20.47	24.23	**27.48**	2.082	16.02	82.4	2024	10.1002/adfm.202411746
20.3	20.6	**27.5**	2.111	16.1	80.9	2024	10.1002/adma.202307743
/	23.36	**27.56**	2.169	15.5	82	2024	10.1002/adma.202312170
18.54	23.09	**27.6**	2.12	15.69	82.97	2024	10.1002/adfm.202412216
19.26	22.31	**27.62**	2.143	15.98	80.65	2024	10.1039/d4ee03419h
21.02	23.58	**27.66**	2.11	15.63	83.64	2024	10.1002/adfm.202419393
19.78	/	**27.76**	2.1	16.58	79.91	2024	10.1002/adma.202410779
18.72	22.7	**27.8**	2.147	15.7	82.6	2024	10.1016/j.joule.2024.05.007
18.83	22.56	**27.81**	2.14	15.69	82.83	2024	10.1126/sciadv.adl2063
19.3	23.24	**27.85**	2.13	15.56	83.89	2024	10.1002/adma.202401698
18.68	23	**27.9**	2.08	16.48	81.4	2024	10.1039/d4ee02427c

18.81	22.29	**28.13**	2.038	16.81	82.1	2024	10.1002/advs.202411403
19.64	22.88	**28.17**	2.13	15.88	83.03	2025	10.1002/aenm.202403186
19.26	23.15	**28.24**	2.11	16.65	80.23	2024	10.1038/s41467-024-46679-w
19.17	22.62	**28.26**	2.15	15.81	83.12	2024	10.1002/adfm.202415797
20.5	21.9	**28.5**	2.16	16.5	80.3	2024	10.1038/s41586-024-08158-6
18.82	22.7	**28.68**	2.1	16.75	81.57	2024	10.1002/adma.202415627
18.46	23.7	**28.71**	2.153	15.77	84.58	2024	10.1039/d4ee02754j
19.48	23.07	**28.73**	2.14	16.2	82.87	2024	10.1002/adma.202411677
19.64	23.32	**28.8**	2.13	16.06	84.19	2024	10.1038/s41467-024-51703-0
19.21	23.48	**28.83**	2.18	15.57	84.8	2024	10.1038/s41560-024-01613-8
18.95	23.97	**27.01**	2.11	15.78	81.1	2025	10.1002/smll.202500383
19.5	21.3	**27.1**	2.11	15.6	82.3	2025	10.1016/j.nanoen.2025.110954
19.52	22.44	**27.25**	2.08	15.57	84.15	2025	10.1016/j.nanoen.2025.110882
17.95	21.02	**27.5**	2.07	16.65	79.69	2025	10.1002/adma.202418766
/	24.33	**27.57**	2.113	15.65	83.39	2025	10.1002/adfm.202421416
/	23.87	**27.61**	2.156	15.63	81.93	2025	10.1021/acsenergylett.4c03370
20.76	20.89	**27.7**	2.11	16.49	79.81	2025	10.1039/d4ee04029e
19.57	22.42	**27.82**	2.11	16.05	82.16	2025	10.1002/aenm.202501871
18.18	22.29	**27.92**	2.06	16.54	81.91	2025	10.1002/aenm.202502835
18.68	23.26	**28.07**	2.171	15.96	80.97	2025	10.1002/adma.202505581
20.03	22.38	**28.1**	2.11	15.88	83.89	2025	10.1016/j.cej.2025.163287
18.45	24.02	**28.12**	2.129	15.68	84.25	2025	10.1021/acs.nanolett.4c04652
19.68	/	**28.16**	2.131	16.14	81.85	2025	10.1038/s41566-024-01570-4
19.27	22.67	**28.16**	2.13	16.29	81	2025	10.1016/j.nanoen.2025.110927
20.13	23.32	**28.2**	2.14	15.89	83.07	2025	10.1038/s41467-025-57195-w
19.92	21.45	**28.25**	2.13	16.11	82.11	2025	10.1002/aenm.202500309
20.47	22.47	**28.3**	2.14	16.05	82.4	2025	10.1002/adma.202502450
19.5	21.3	**28.3**	2.17	16.1	81.2	2025	10.1039/d4ee02898h
19.37	22.87	**28.34**	2.154	16.31	80.7	2025	10.1016/j.jechem.2024.09.007
18.57	23.37	**28.33**	2.16	16.16	81.01	2025	10.1002/adma.202502770
20.1	22.2	**28.5**	2.15	16	83	2025	10.1038/s41467-025-59515-6
19.84	/	**28.51**	2.14	16.13	82.58	2025	10.1002/anie.202424825
19.34	21.64	**28.53**	2.131	16.21	82.6	2025	10.1002/adma.202412943
19.03	23.21	**28.55**	2.131	16.05	83.5	2025	10.1038/s41467-025-58810-6
19.12	23.54	**28.61**	2.155	16.05	82.73	2025	10.1038/s41467-024-55492-4
19.5	/	**28.65**	2.16	16.25	81.45	2025	10.1002/anie.202511743
21.1	23.2	**28.7**	2.207	16	81.1	2025	10.1038/s41563-024-02073-x
20.35	22.02	**28.71**	2.18	16.19	81.35	2025	10.1038/s41565-025-01899-z
19.94	/	**28.83**	2.15	16.19	82.81	2025	10.1021/acsnano.5c03542
20.26	23.3	**28.87**	2.12	16.3	83.56	2025	10.1016/j.joule.2025.101825
20.23	22.01	**28.9**	2.183	15.74	84.1	2025	10.1039/d5ee01369k
20.67	22.55	**28.94**	2.146	16.19	83.29	2025	10.1038/s41467-025-58111-y
20.27	22.88	**28.95**	2.134	16.05	84.52	2025	10.1038/s41566-025-01616-1
20.71	23.02	**28.99**	2.16	16.52	81.24	2025	10.1002/adma.202504321

20.70	22.3	**29**	2.19	16.4	81	2025	10.1039/d5ee02462e
/	23.02	**29.33**	2.22	16.45	80.33	2025	10.1038/s41467-025-56549-8

Reference

[1] Lu, T. & Chen, F. Atomic dipole moment corrected Hirshfeld population method. *J. Theor. Comput. Chem.* **11**, 163-183 (2012).

[2] Zhang, J. & Lu, T. Efficient evaluation of electrostatic potential with computerized optimized code. *Phys. Chem. Chem. Phys.* **23**, 20323-20328 (2021).

[3] Liu, Z., Lu, T. & Chen, Q. Intermolecular interaction characteristics of the all-carboatomic ring, cyclo[18]carbon: Focusing on molecular adsorption and stacking. *Carbon* **171**, 514-523 (2021).

[4] Yang, Y. et al. Design and applications of hole-selective self-assembled monolayers for perovskite photovoltaics. *Chem. Eng. J.* **504**, 158870 (2025).

[5] Pino-Rios, R., Inostroza, D., Cardenas-Jiron, G. & Tiznado, W. Orbital-weighted dual descriptor for the study of local reactivity of systems with (quasi-) degenerate states. *J. Phys. Chem. A* **123**, 10556-10562 (2019).

[6] Wu, Y. et al. Exploring thearomaticity differences of isoelectronic species of cyclo[18]carbon (C_{18}), $B_6C_6N_6$, and B_9N_9-the role of carbon atoms as connecting bridges. *Inorg. Chem.* **62**, 19986-19996 (2023).

[7] Fuster, F. & Grabowski, S. J. Intramolecular hydrogenbonds: the QTAIM and ELF characteristics. *J. Phys. Chem. A* **115**, 10078-10086 (2011).

[8] Lu, T. Visualization analysis of covalent and noncovalent interactions in real space. *Angew. Chem., Int. Ed.* **64**, e202504895 (2025).

[9] Lu, T. & Chen, Q. Revealing molecular electronic structure via analysis of valence electron density. *Acta Phys.-Chim. Sin.* **34**, 503-513 (2018).

[10] Wang, J. et al. Less-acidic boric acid-functionalized self-assembled monolayer for mitigating NiOx corrosion for efficient all-perovskite tandem solar cells. *Nat. Commun.* **16**, 4148 (2025).

[11] Lu, T. & Chen, Q. van der Waals potential: an important complement to molecular electrostatic potential in studying intermolecular interactions. *J. Mol. Model.* **26**, 315 (2020).

[12] Yin, S. et al. A green-solvent-processable polymer hole transport material for achieving 26.31% efficiency in inverted perovskite solar cells. *Energy Environ. Sci.* **18**, 4153-4161 (2025).

[13] Fan, Y., Du, J., Zhao, W., Ma, X. & Yu, X. Molecular insights into Marcuss theory: an Ab initio quantum chemistry computational lab practice for charge transfer kinetics pedagogy. *J. Chem. Educ.* **101**, 3418-3427 (2024).

[14] Liu, Z., Lu, T. & Chen, Q. An sp-hybridized all-carboatomic ring, cyclo[18]carbon: Electronic structure, electronic spectrum, and optical nonlinearity. *Carbon* **165**, 461-467 (2020).

[15] Zhang, S. et al. Self-assembled π-conjugated hole-selective molecules for UV-resistant high-efficiency perovskite solar cells. *Angew. Chem., Int. Ed.* e202508782 (2025).

[16] Lu, T. & Chen, Q. Ultrastrong regulation effect of the electric field on the all-carboatomic ring cyclo[18]carbon. *Chemphyschem* **22**, 386-395 (2021).

[17] Ruhle, S. Tabulated values of the Shockley-Queisser limit for single junction solar cells. *Sol. Energy* **130**, 139-147 (2016).